Numerical Modelling of Wastewater Dispersion from Offshore Hydrogen Electrolysis in the Dutch North Sea - implications for the marine environment

Utrecht University

Bas van der Hagen

6467032

First supervisor: Dr. Martin Ziegler — **Utrecht University (Geosciences)**

Second supervisor: Dr. Johan van der Molen — **Royal Netherlands Institute for Sea Research**

Third supervisor: Dr. Mohammad Daliri — **Royal Netherlands Institute for Sea Research**

Contents

Acknowledgements

I would like to express my deepest gratitude to Mohammad Daliri from the Royal Netherlands Institute for Sea Research (NIOZ), without who the completion of this project would not be possible. Even while entering fatherhood during this project, Mohammad always found time to help me learning the process of numerical modelling or providing excellent scientific discussion. I would also like to extend special thanks to Johan van der Molen (NIOZ), Udeke Huiskamp (Utrecht University) and Martin Ziegler (Utrecht University) for guiding me on this project, providing useful feedback and valuable insights.

Abstract

The Dutch government has recently unveiled plans to establish the North Sea's first offshore green hydrogen electrolyser in the 'Ten Noorden van de Waddeneilanden' region, situated 84 kilometres off the northern Dutch coast, by 2031. However, hydrogen electrolysis generates a hypersaline brine waste product as a result of desalination, as well as a large amount of thermal effluent after cooling the electrolyser stack, both potentially harmful for the marine environment. This study evaluates the hydrodynamic and ecological impacts of these wastewater discharges using a numerical modelling approach. A high-resolution Delft3D-Flow model is nested within a large-scale, pre-validated outer model named the General Estuarine Transport Model (GETM). The investigation includes 14 scenarios, altering the electrolyser capacity and discharge characteristics during summer and winter conditions. The thermal plume is largely confined to the top 5 meters of the water column but extends into the far-field of the domain. The brine plume shows sinking towards the seabed during minimum current velocity at the change of the tide, as well as limited dispersal in the surface domain. The brine was found to be dispersing at the seabed, though diluted within one tidal cycle. The brine plume shows very marginal salinity increases for all simulated scenarios, whereas the thermal plume shows temperature increases of several degrees Celsius. The winter scenarios show a respective 17.7% and 11.3% reduction in affected seawater volume for coolant and brine simulations compared to summer simulations. Simultaneous release of both coolant and brine showed no effect on the dispersion of heat in both the surface and the vertical of the domain, while the distribution of salinity was profoundly altered compared to the discharge of brine alone. Combined discharge induced positive buoyancy of the brine plume resulting in significantly increased surface dispersion, while the sinking patterns were largely negated. The model is not able to accurately represent extremely slight salinity changes when invoking combined discharge due to the substantially higher flowrate compared to discharging brine alone. The ecological effects of the thermal effluent possibly include the induction of heat stress near the discharge point, while the direct effects of increased salinity due to the brine discharge are far lower than the natural variation within the domain. The results of this study offer a valuable pilot and baseline for this topic of research, underscoring the need for further investigation and suggesting potential areas for future research.

1. Introduction

For the past few decades, the need to decarbonize the global energy supply has been increasingly emphasized by environmental studies (IEA, 2021). Electrification of the energy budget has been regarded as the prime pathway to decarbonisation. This process is particularly challenging for some industries; mainly in heavy transport, chemistry and steel production (Lehner et al., 2022). Using hydrogen gas as a high-density versatile energy carrier can play a pivotal role in the transition to sustainable energy for such applications.

Presently, hydrogen gas is predominantly produced from various non-renewable resources such as the steam reforming of methane, oxidation of oil, and coal gasification. As of now, less than 1% of total hydrogen produced is classified as ‘green’, signifying carbon neutrality (Taibi et al., 2018). In order to produce green hydrogen, its production necessitates water electrolysis using renewable electricity. Nevertheless, this manufacturing approach imposes difficulties attributed to the substantial demands for feedwater and energy inherent in the large-scale production process. In order to account for these prerequisites, the primary process being currently explored is the implementation of an offshore wind-to-hydrogen system where the electricity feed originates from offshore wind farms (Groenemans et al., 2022; Morales et al., 2023; Niblett et al., 2024). Positioning hydrogen electrolysers in an offshore environment has the additional advantage of using seawater as feedwater, as it is readily available and does not pose risks to freshwater budgets (Caparros Mancera et al., 2020).

In this context, the North Sea emerges as a significant player. In the fall of 2020, the European Commission introduced the EU Strategy on Offshore Renewable Energy, a crucial initiative aimed at achieving the EU’s climate neutrality goal by 2050. This strategy was endorsed by the nine North Sea Energy Cooperation (NSEC) countries, who pledged to ambitious offshore wind energy targets. To realize this capacity, political leaders from four of the NSEC countries (the Netherlands, Belgium, Denmark and Germany) signed the Esbjerg Declaration in the spring of 2022 (Esbjerg Declaration, 2022). This declaration outlines their joint efforts to develop the North Sea as an offshore renewable energy system. The potential capacity of offshore renewable energy from wind is much larger than can be directly absorbed as electricity in existing energy infrastructure. Therefore, excess renewable energy capacity can be utilized for water electrolysis, turning the North Sea into a significant source of hydrogen gas production. In late 2023, the Dutch government unveiled plans to establish the first large-scale hydrogen electrolysis hub in the area known as ‘Ten Noorden van de Waddeneilanden’ (TNW), located north of the Wadden Sea Islands, within the Dutch Exclusive Economic Zone (see Figure 1). This initiative is designed to complement the existing offshore wind farm with the same name (Rijksoverheid, 2023). The TNW area is uniquely positioned to leverage the existing gas infrastructure for hydrogen gas distribution. The offshore wind farm associated with the project contains potential electrolysis capacity of approximately 700 MW. The project is aimed to reach full operational status by 2031.

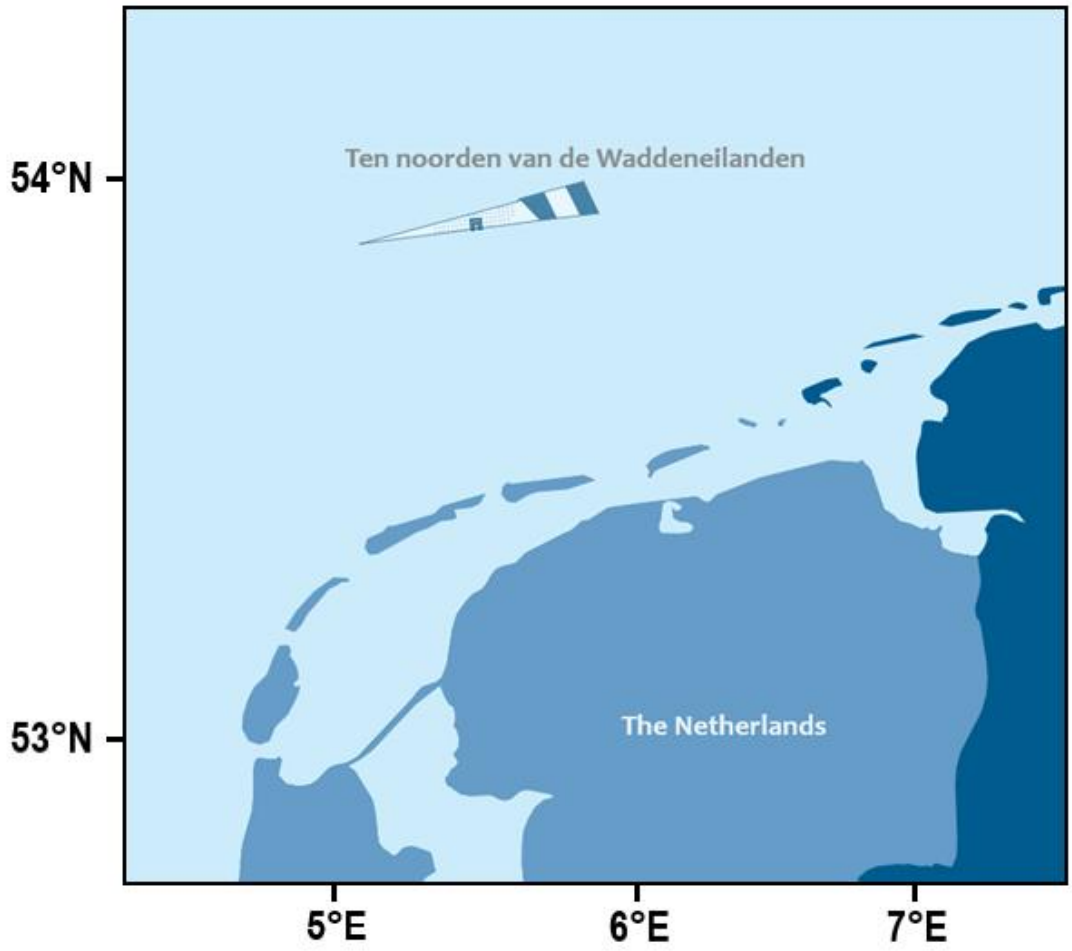

Figure 1. *Location of the TNW (Ten Noorden van de Waddeneilanden) area.*

Note. Retrieved and modified from www.windopzee.nl. Blue fill: existing windfarms at 1 GW capacity. White fill: planned windfarms at 10 GW capacity.

One important aspect associated with offshore electrolysis is the emission of a hypersaline wastewater stream, commonly referred to as brine. Electrolysers require the use of ultrapure water at the anode of the system. In order to provide ultrapure feedwater, readily available seawater undergoes a desalination process, where a high-salinity brine is produced (Eichner et al., 2022; Kumar et al., 2019). The salinity of such brine depends on the water recovery ratio of the process and the desalination technique utilized. Additionally, the electrolysis process generates a substantial amount of heat due to inherent inefficiencies in the system (Wang et al., 2022). In larger scale offshore electrolysis plants, such as the one projected to take place in the TNW area, air cooling may not be sufficient to maintain operating temperatures (Srinath et al., 2022). For such plants, liquid cooling would be the solution of choice. This necessitates the incorporation of a cooling water stream characterized by significantly elevated temperatures compared to the surrounding ambient seawater (Danish Energy Agency, 2023). Recent research highlighted that brine streams originating from desalination plants may negatively impact the local marine environment (Belkin et al., 2015; Frank et al., 2017; Omerspahic et al., 2022). The studies, performed in the Eastern Mediterranean Sea and the Arabian Gulf, show elevated salinity levels near the brine stream, which impacts local flora and fauna, including seagrasses, fish, and meiofauna. Furthermore, a large input of (hyper)saline water can change the local distribution of water density, initiating stratification processes, observed in the coastal Pacific Ocean (Lykkebo Petersen et al., 2019). Long-term stratification has been identified as destructive to benthic communities and

reproductive processes involving the marine benthos in a case study in the Canary Islands (Riera et al., 2012). Similarly, the effects of thermal discharge have shown detrimental effects in the marine environment: studies performed on thermal discharge resulting from industrial cooling cycles, such as coastal power plants in Northern Taiwan and the Western Mediterranean Sea, showed that steep rises in local temperatures arise, disturbing local biota (Chuang et al., 2009; Lardicci et al., 1999; Li et al., 2014). Changes in water temperature also lead to significant decrease in dissolved oxygen levels, which in turn lead to changes in metabolism, reproduction and increased mortality in local aquatic communities as shown in a case study investigating the effects of thermal discharge by a coastal power plant in the South Chinese Sea (Li et al., 2014).

Most research on thermal and brine discharges concentrates on coastal settings, specifically where a steep bathymetric slope exists and the land boundary significantly affects the dispersal pattern of the discharge. These locations are typical for facilities that produce such waste. This leaves a research gap regarding the impact of wastewater discharge in non-coastal environments such as shelf seas. The dispersion of saline and thermal plumes in open seas could significantly differ from coastal settings due to variations in bed shear effects, water depth, and the presence of a land boundary (Stanev et al., 2009; Bosboom & Stive, 2021). Without a land boundary and bed shear effects, plumes could disperse more extensively due to reduced flow resistances. Additionally, greater water depths may enhance vertical plume expansion. The ecological implications of wastewater discharge may also differ between coastal and shelf sea environments, due to variations in biodiversity and density (Gray, 1997). Coastal habitats, known for their high biological productivity, may suffer greater detrimental effects from wastewater discharges compared to deeper offshore areas. However, coastal organisms are generally well-suited to rapid changes in salinity and temperature due to the significant variability in these parameters within coastal zones. Consequently, the impact on open sea habitats, where natural variability in these parameters is lower, could be more severe.

Jia et al. (2016) further concluded that the area affected by diffusion is likely considerably smaller in the open ocean than in estuaries or coastal areas, due to the ocean's high rate of water exchange and mixing. However, the dispersion pattern of such wastewater streams in an open ocean setting remains unknown. Therefore, this thesis aims to explore the impact of high salinity and thermal plumes resulting from offshore electrolysis on the ecosystem and hydrodynamics of the North Sea in the vicinity of the TNW area.

In addressing this challenge, a series of numerical simulations was designed with the primary goal of understanding the possible ecological- and hydrodynamical impacts associated with the discharge of wastewater with varying temperature and salinity characteristics. The simulations were performed under a set of scenarios, varying parameters such as wind stresses, water temperature, wastewater discharge rate and wastewater composition. The temporal/spatial evolution of temperature and salinity were modelled using the Delft3D package, developed and maintained by Deltares (Deltares, 2023). The model is recognized as one of the most robust and reliable tools for studying coastal circulation dynamics, sediment transport, and water quality, both from the standpoint of practical applications and research and development (Bai et al., 2022). The model formulated in this study could potentially act as an initial pilot, laying the groundwork for future research and development. Furthermore, considering that the discharge of wastewater from commercial hydrogen electrolysers into the Dutch North Sea must comply with the regulations stipulated by the OSPAR agreement (OSPAR, 2021) and the London Protocol (IMO, 2022), the findings of this study may offer a preliminary framework to guide investigations towards regulatory compliance.

In order to determine the inputs for the model, a comprehensive survey of the existing literature was carried out. This encompasses the current state of research regarding electrolyser techniques and associated emissions, as well as the current understanding of the dispersal of brine and thermal plumes in marine areas.

2. Background

Hydrogen electrolysis technology

There are several electrolysis technologies that have been widely studied, including Alkaline Liquid Electrolysis Cells (ALECs), Alkaline Membrane Electrolysis Cells (AMECs), Proton Exchange Membrane Electrolysis Cells (PEMECs), and Solid Oxide Electrolysis Cells (SOECs). Among these, AMECs and SOECs have shown unsatisfactory durability, limiting their immediate application (Wang et al., 2022). Both ALECs and PEMECs have been successfully commercialized due to their superior performance and durability. However, ALECs suffer from low operating current density and high maintenance costs (Salehmin et al., 2022). PEM electrolysers have gained increasing attention due to their high efficiency, low maintenance cost, fast dynamics, and high H_2 purity. Furthermore, PEMECs are significantly more compact than ALECs, which enables simplified system design, manufacture, and installation (Wang et al., 2022). Therefore, PEMECs have become the hydrogen electrolysis method of choice for offshore hydrogen electrolyser concepts and projects (PosHYdon; Fraunhofer, 2021; RWE, n.d.).

Desalination techniques

PEM electrolysers operate using a solid polymer electrolyte that conducts protons, separates product gases and electrically insulates the electrodes. At the anode of the system, deionized water reacts to form oxygen and protons. Protons are transferred to the cathode, where electrons from the external circuit form hydrogen gas (Görgün, 2006). A schematic overview of this process is displayed in Figure 2.

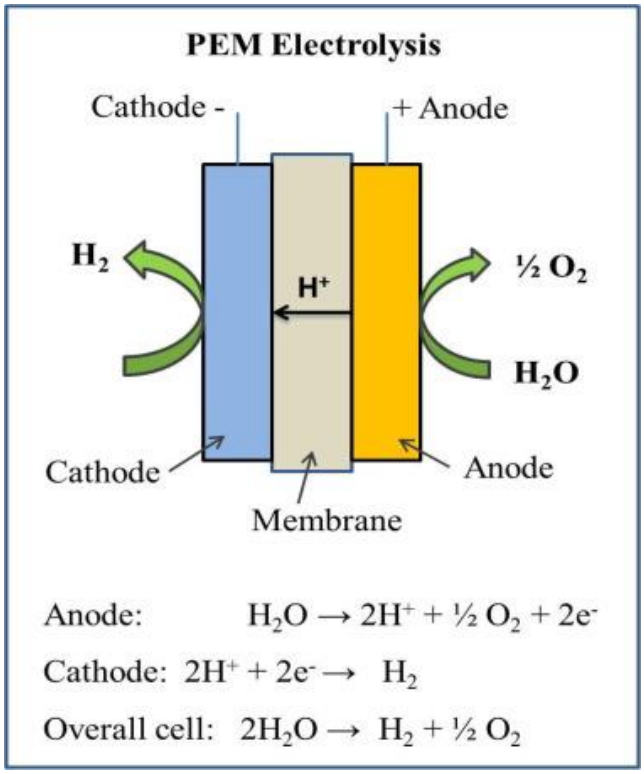

Figure 2. *Schematic illustration of PEM water electrolysis.*

Note. Adapted from Kumar & Himabindu (2019).

This process implies the necessity of high-purity feedwater, as dissolved ions would otherwise compete for ion exchange, and dissolved salts could lead to reduced efficiency and even damage to the system (Cassol et al., 2024). When considering hydrogen electrolysis on a large scale, meaning contributing to a large share of the global energy supply in the near future, shortages in water distribution may arise (Shahzad & Burhan, 2017). Given that seawater forms a virtually infinite source of feedwater, current research is looking into the direct use of seawater as a feedstock for electrolysis, specifically through the direct splitting of seawater (Dresp et al., 2019). However, this approach is still in its early stages due to the inherent complexity of natural seawater, which could potentially accelerate system degradation or contaminate the water splitting catalyst (Dionigi et al., 2016). In an offshore context, hydrogen electrolyser plants would likely be paired with conventional desalination technologies. These, in turn, may need to be coupled with an additional purification system to achieve the necessary purity level of feedstock water for commercial electrolysers (Darre & Toor, 2018).

Several desalination techniques are commercially ready. As of today, several main desalination strategies have been posed to be potentially effectively coupled to offshore PEM electrolysis, the most common listed here.

- Forward Osmosis (FO) desalination utilizes the natural osmotic pressure gradient to move water from a low solute concentration (pure water) to a high solute concentration (saltwater) across a semi-permeable membrane (Li et al., 2023). A last step involves the separation of freshwater from the diluted draw solution. A simple graphic representation of FO depicted in Figure 3-1.
- Reverse Osmosis (RO) desalination applies external pressure to force water from a high solute concentration (saltwater) to a low solute concentration (pure water) (Hilal et al., 2011). This process occurs against the natural osmotic pressure gradient. A simple graphic representation of RO depicted in Figure 3-2.
- Membrane Distillation (MD), a thermally driven separative process enabled by phase changes. The heated feed solution is in contact with a membrane, allowing evaporation to take place at the feed-membrane surface. The membrane is fully hydrophobic, thus the liquid phase is prevented from passing through the membrane, allowing only pure water vapour to pass which is subsequently condensed (Ghaffour et al., 2019). The process is schematically depicted in Figure 3-3.
- Multi-Stage Flash Distillation (MSF) utilizes multiple stages of decreasing pressure, where in each stage saltwater is heated and evaporated. Vapor is subsequently condensed to produce pure water (Feria-Díaz et al., 2021). A schematic representation of MSF is displayed in Figure 3-4.

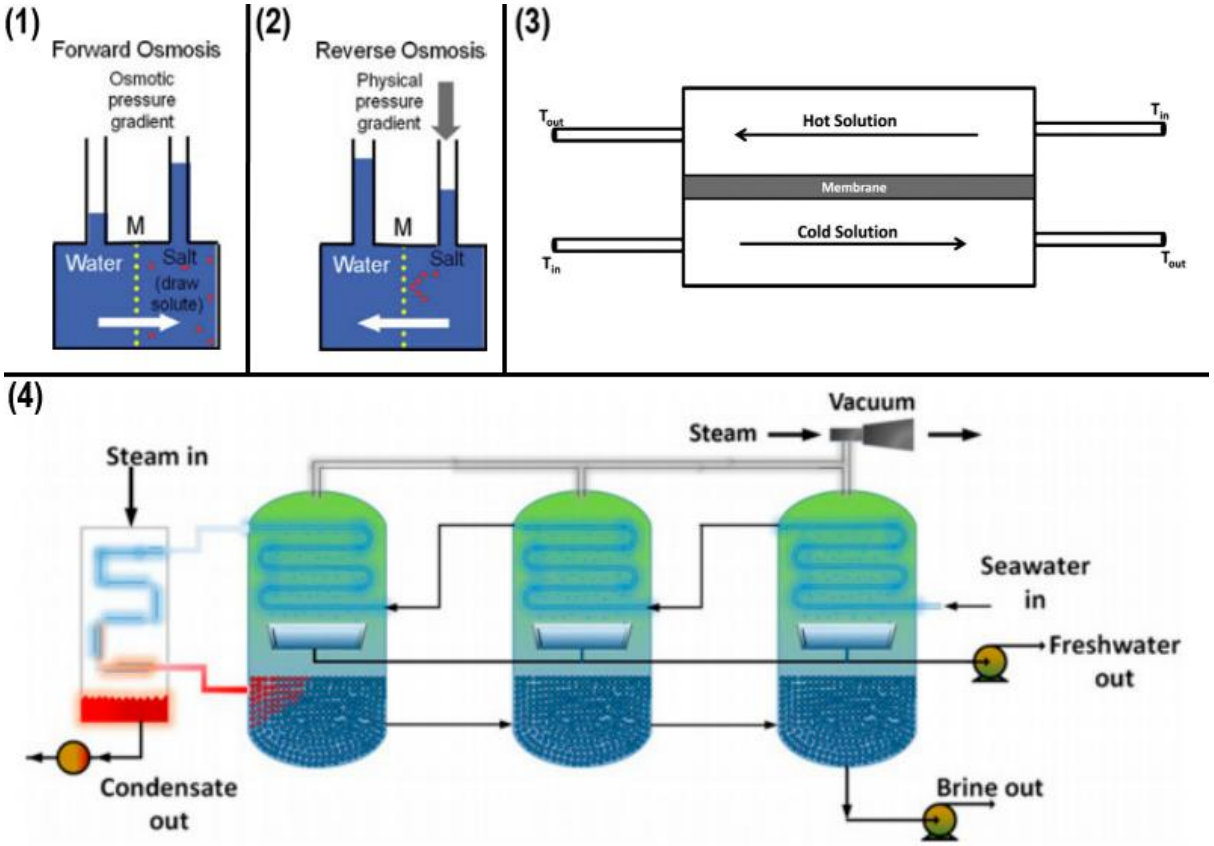

Figure 3. *Schematic representations of widely used desalination techniques.*

Note. Figures 3-1 and 3-2 are adapted from Qin et al. (2014). Figure 3-3 is adapted from Alkhudhiri et al. (2012). Figure 3-4 is adapted from Feria-Díaz et al. (2021).

With FO, MD and MSF being troubled by high module costs, high energy usage and upscaling difficulties (Ghaffour et al., 2019), the currently most widely used seawater desalination strategy is RO (Darre & Toor, 2018). Using established techniques such as RO in desalination for PEM electrolysis is favourable in terms of designing, maintaining and upscaling costs. Citing Sajna et al. (2023): 'RO desalination presents several advantages over thermal options, including adaptability to local conditions, lower capital expenditure and potentially significant CO2 emission reduction. Given its simple processing, cost-effective installation, and minimal chemical usage, RO technology represents the future of desalination and forms the foundation of the seawater hub concept' (p 3-4).

One major drawback in any desalination technique is the steady production of hypersaline wastewater. This poses the problem of potential environmental impact, as well as increased economic costs of wastewater treatment (Davenport et al., 2018). As highlighted in Zainal et al. (2024), it is critical to lower the cost of green hydrogen production in order to facilitate large scale manufacturing. Currently, surface water dumping of saline wastewater remains the most cost-effective method to discharge produced brine not accounting for environmental considerations (Panagopoulos et al., 2019). In order to assess the impact such brine discharge has on the local marine environment, it is important to quantify the characteristics of such brine in terms of composition and volume corresponding to a certain rate of hydrogen production.

Brine outflow characteristics

In order to produce hydrogen, PEM electrolysis plants typically need 9-11 kg pure water to produce 1 kg of hydrogen (Birol, 2019). In a more recent study by Morales et al. (2023) it was shown that in order to produce 50000 kg of hydrogen in one day, 1600 m^3 of seawater is used in the desalination process, resulting in 1100 m^3 of brine. 500 m^3 Ultra-Pure Water (UPW) is extracted, indicating an UPW recovery rate of 0.31. 500 m^3 corresponds to roughly $5*10^5$ kg of seawater needed to produce $5*10^4$ kg hydrogen, in accordance with the generally assumed ratio of 1:9 (Birol, 2019).

This result was acquired whilst assuming the following:

- Additional water demands for cooling or steam generation in the other processes were not considered.
- The electrolyser is running at a constant 100% load.

As described by Panagopoulos et al. (2019), with the volume of feedwater and wastewater known, the amount of Total Dissolved Solid (TDS) per kg brine can be calculated as follows:

$$TDS_{brine} = TDS_{feed} * (\frac{1}{1-R}) \quad (1)$$

with R, the recovery rate, being defined as:

$$R = \frac{Q_{prod}}{Q_{feed}} \quad (2)$$

Q_{prod} being the produced volume of desalinated water, and Q_{feed} the total volume of feedwater (seawater).

$$Q_{brine} = Q_{feed} - Q_{prod} \quad (3)$$

In the case of 1600 m^3 feedwater with a TDS of 35.00 g/L and 1100 m^3 brine per day (R = 0.313) for producing 50000 kg H_2 (Morales et al., 2023), the resulting wastewater stream would be 1100 m^3 brine per day with a TDS of 50.91 g/L, running at a capacity of 111.9 MW. This volumetric input flowrate is in general accordance with Simoes et al. (2021), who estimated a water usage of 700 m^3 per day for a 60 MW electrolyser. Considering the mass balance principle applied to the process of hydrogen generation, the production of brine is directly proportional to the hydrogen production, which in turn determines the capacity of the electrolyser (Calado & Castro, 2021). The brine outputs and its characteristics of two distinct offshore electrolyser concepts were compared: one for research purposes (Morales et al., 2023) and one for commercial applications (undisclosed). Employing a linear scale to correlate hydrogen production, electrolyser capacity and brine production, the results were normalized to 1 MW electrolyser capacity. The values were compared to an analytical approach, where:

- The amount of hydrogen produced per MW capacity were derived from a typical commercial hydrogen electrolyser (HTEC, n.d.) (450kg H_2 per MW at 100% load).
- The amount of feedwater needed per kilogramme H_2 produced were assumed to be 11 L per kg H_2 (Shi et al., 2020).
- The TDS were calculated via formulas 1, 2 and 3.

The results are displayed in Table 1.

Table 1. *The characteristics of electrolysis induced desalination brines from literary findings, an analytical approach and an undisclosed commercial plant.*

Study	Desalination technology	Recovery rate	Electrolyser capacity (MW)	Feedwater - normalized (1MW)	Brine output - normalized (1MW)	Brine composition - TDS
Moralez et al. (2023)	RO	0.31	111.9	0.596 m^3/h	0.410 m^3/h	50.91 g/L
Analytical approach	RO	0.33	1	0.619 m^3/h	0.413 m^3/h	52.50 g/L
Commercial plant	TD	0.33	480	0.462 m^3/h	0.303 m^3/h	52.50 g/L

Note. Desalination technology RO refers to Reverse Osmosis. Desalination technology TD refers to Thermal Desalination, a broad term referencing to the desalination strategies involving the heating of saltwater in order to extract pure water vapour.

Heat output of electrolysis

PEM cells generate heat as a result of ohmic losses in the system as well as inefficiencies in the electrolysis process (Ni et al., 2008; Mo et al., 2023; van der Roest et al., 2022). The study by van der Roest et al. (2023) provides rough estimates of excess heat for PEM operation, assuming a third party can utilize the heat, with a theoretical waste heat of 20% of the input energy. The analysis by Zauner et al. (2019) for the European Commission estimates a waste heat of approximately 30% of the electrolyser's power input for both alkaline and PEM electrolysers. D'Amore-Domenech & Leo (2019) assume alkaline and PEM electrolysers to have identical heat outputs, estimating a waste heat of around 20% of the energy input. However, it is important to note that the efficiency of PEM electrolysers diminishes over their lifespan, leading to a progressive increase in heat generation.

At present, electrolyser stacks are cooled using air cooling. The excess heat generated by the stack, which operates at temperatures ranging from 50-80°C (PEM), is effectively dissipated by dry coolers positioned atop the electrolyser containers (van der Roest et al., 2022; PosHYdon). However, the significant power consumption associated with dry cooling presents a challenge to scalability (Niekerk & Manita, 2022). For electrolyser plants on a larger scale, liquid-cooled systems are considered the most suitable cooling solution, offering advantages from both a financial and power consumption perspective. In an offshore setting, the abundant supply of seawater alleviates potential issues such as freshwater scarcity and logistical complications of accounting for large coolant feed that are more prevalent with land-based electrolysers, thereby enhancing the appeal of liquid-cooled solutions. While air-cooled systems dissipate heat directly into the atmosphere, liquid-cooled systems manage heat by discharging condenser cooling water that is at a higher temperature than the ambient waters. The temperature of the cooling water can be controlled by adjusting the quantity of coolant introduced into the system. A larger volume of water circulating through the system results in a higher volumetric flow rate and a smaller temperature differential relative to the surrounding seawater. Conversely, reducing the coolant intake leads to a lower volumetric flow rate and a larger temperature difference compared to ambient (RWE, n.d.).

In order to estimate the volumetric outflow of cooling water at different conditions, the cooling water usage of an undisclosed commercial plant was identified and compared to an analytical approach. In this case, the values as published by the commercial plant are as follows: The plant runs at a capacity of 480 MW at 100% load, where 76.8 MW of waste heat is disposed

by coolant. Assuming an initial water temperature of 18ºC and a target wastewater temperature of 30ºC, $5.6*10^6$ kg seawater per hour is used for cooling purposes, with a TDS of 35g/L. In order to convert these values to the standardized unit for volumetric flowrate (m^3/h), seawater density was calculated to be 1021.84 kg/m^3 using the methodology as published by Millero et al. (1980). The analytical approach utilized the base values of the commercial plant, and related the changes in coolant volumetric flowrate via the equation of specific heat:

$$Q = m * c * \Delta T \tag{5}$$

Where Q is heat [J], m is seawater mass [kg], c is the specific heat capacity [J/kg*ºC] and ΔT the change in temperature [ºC]. A constant c = 3990 J/kg*ºC was assumed (Cox & Smith, 1959). Given that the heat output of the electrolyser is directly proportional to its capacity, the required mass of seawater (and thus its volume) can be calculated for different temperature differentials between coolant and seawater feed. The relation between heat generated, temperature differential and the corresponding required feedwater flowrate is displayed in Figure 4.

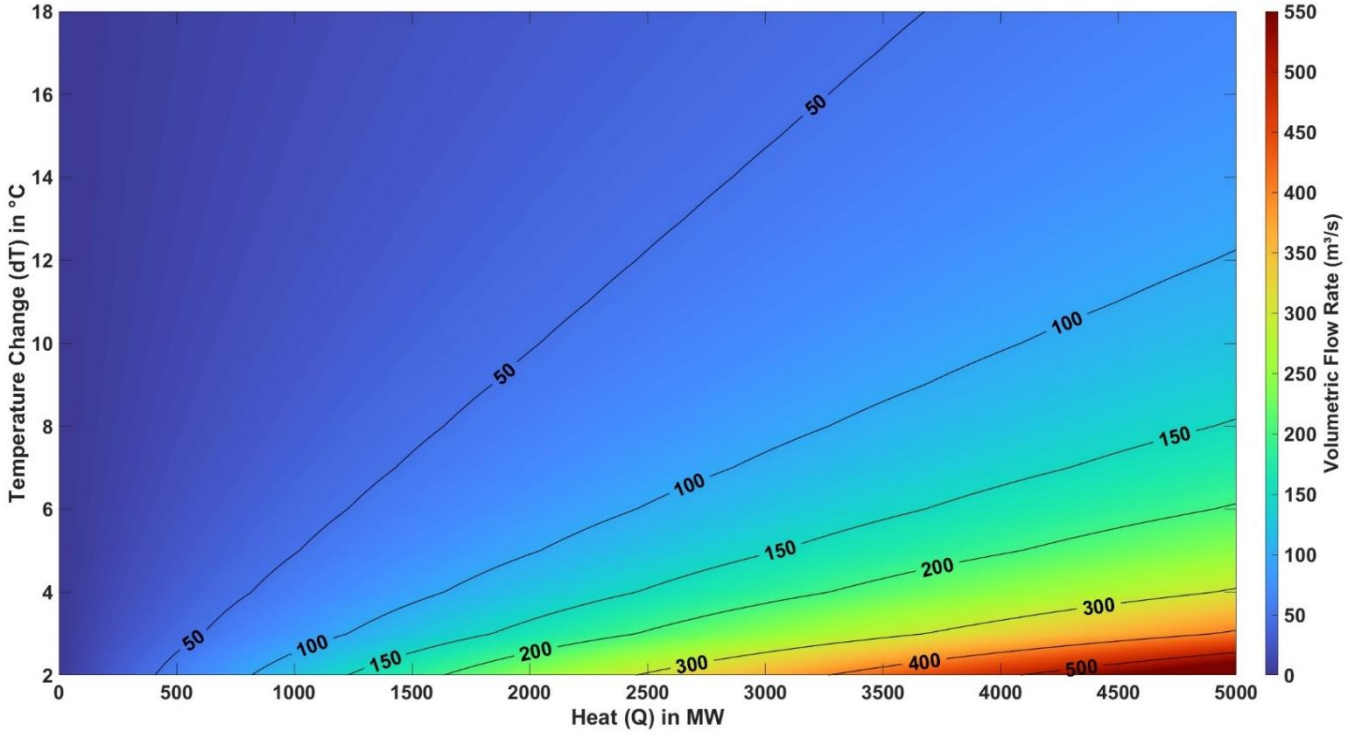

Figure 4. *Volumetric flowrate of feedwater required for a given temperature differential and generated heat*.

Study location

The Ten Noorden van de Waddeneilanden (TNW, latitude: 54.00 ºN to 54.05 ºN, longitude: 5.23 ºE to 5.86 ºE) area is a designated area for offshore wind parks. It is located 84 kilometres off the coast of the Netherlands and is positioned west of the maritime border with Germany (see Figure 1). In late 2023, the Dutch government announced plans to set up the first major hydrogen electrolysis centre in the region. This plan is intended to enhance the current offshore wind farms (Rijksoverheid, 2023). TNW is ideally located to take advantage of the existing offshore gas infrastructure for the distribution of hydrogen gas. The offshore wind farms linked with this initiative have an electrolysis capacity of roughly 700 MW. The objective is for the project to be fully operational by 2031.

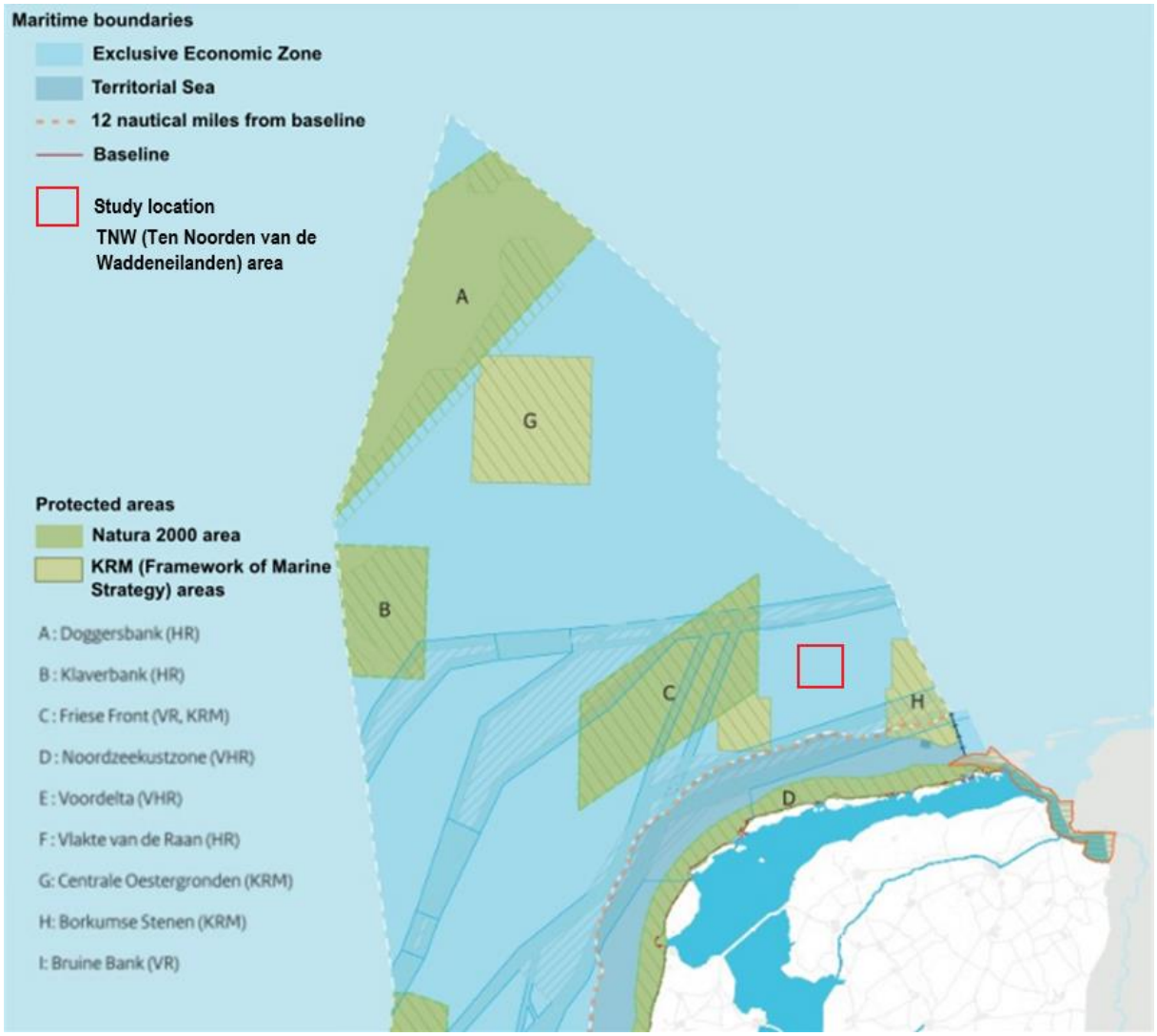

Figure 5. *The offshore wind region of TNW (Ten Noorden van de Waddeneilanden) depicted in relation to marine conservation zones.*

Note. Adapted and modified from Rijksoverheid (2023). Protected areas translated in English; A: Doggersbank. B: Cleaver Bank. C: Frisian Front. D: North Sea Coastal Zone. E: Foredelta. F: de Raan Plain. G: Central Oystergrounds. H: Borkum Reef Ground. I: Brown Bank.

West and south of the TNW area, three areas of conservation and marine protection are situated: Frisian Front (C in Figure 5), North Sea Coastal Zone (D in Figure 5), and Borkum Reef Ground (H in Figure 5). The Frisian Front, 80 kilometres off the coast, is a biologically diverse transition zone in the North Sea, home to various benthic species and a bird foraging area (Dewicke et al., 2002; Baars et al., 1991; Creutzberg et al., 1984). The North Sea Coastal Zone, from Bergen to the Eems, is a fish nursery, particularly for herring, plaice, and sole, and has a rich bottom life (Troost et al., 2013). Borkum Reef Ground, north of Schiermonnikoog, is a habitat for both epifauna and infauna, with 123 distinct species identified (Hahn et al., 2022), and is significant for reef conservation projects (Pogoda et al., 2020).

Dispersion patterns of density plumes

It is difficult to accurately predict the dispersion pattern of a wastewater plume of a given temperature and salinity. The current scientific literature on marine plume dispersal is heavily biased towards coastal discharge by thermal power plants and desalination facilities. While these studies may not directly correspond to the TNW area, the similarity in water depths (approximately 30 meters) across most study areas offers valuable insights into the dispersal of wastewater in similarly shallow aquatic environments.

At the outset of a discharge channel, momentum is induced within the wastewater stream. Thus, the plume is initially dominated by inertial processes (Laguna-Zarate et al., 2021). Given the high initial momentum of the discharge, a high degree of mixing occurs in close proximity to the outlet.

Increased water temperatures lead to a reduction in water density, whereas an increase in salinity result in a higher water density. This causes contrasting behaviours in the discharged plumes: negatively buoyant brine plumes generally sink to the ocean floor, whereas positively buoyant thermal plumes disperse at surface level (Fernández-Torquemada et al., 2009; Laguna-Zarate et al., 2021). Therefore, the trajectories of brine and thermal plumes are governed by different processes; the propagation of thermal plumes is almost fully dictated by surface winds, whereas the propagation of brine plumes is influenced by the ambient current within the water column (often forced by tidal influence) and bathymetric features (Gaeta et al., 2020; Morelissen et al., 2016; Wood et al., 2021).

A consensus exists regarding the importance of seasonal variability on the manner of which brine and thermal plumes disperse. In most near-shore marine areas, the water column is generally more vertically well-mixed during winter, as winter storms induce mechanical mixing and convective vertical mixing occurs due to net heat losses to the atmosphere (Wood et al., 2021). During summer, a lower frequency of wind-induced mechanical mixing events along with heat uptake from the atmosphere by the water surface induces stratification of the water column, along with the formation of thermoclines (Li et al., 2020). This is of importance, as the TNW area is subject to intermittent stratification and heightened freshwater influence, albeit with interannual variability (van Leeuwen et al., 2015). Heavy stratification has been recorded to prevent brine from reaching the ocean floor in the western Mediterranean (Fernandez-Torquemada et al., 2009). Cold bottom waters can reach higher density than the emitted brine from desalination facilities, preventing the formation of a saline bottom layer which could potentially be favourable for the local benthic ecosystem. Summer stratification can also induce the entrainment of warm waters when brine descends through a stratified water column, resulting in both salinity and temperature anomalies at depth according to a modelling study of the eastern Mediterranean (Wood et al., 2021).

The affected area, thus the area where changes in temperature and salinity are a measurable result of wastewater discharge, is primarily dictated by the volumetric flowrate of the

wastewater and its composition in combination with the local hydrodynamic conditions. Some key trends can be identified. For thermal plumes, a decrease in wind forcing shows an increase in affected area as well as a decrease in diffusion rate, found in modelling studies for the Red Sea and the Mediterranean Sea (Aljohani et al., 2021; Deabes, 2020; Gaeta et al., 2020). Furthermore, dispersal tends to be unidirectional for scenarios of high wind forcing. Thus, while higher wind speeds may enhance the dispersal rate of the water, the increased mixing and diffusive processes prevail, leading to a smaller affected area. For brine plumes a similar trend is visible: during winter months, propagation of brine is more limited in space and velocity according to modelling studies in the Red Sea and eastern Mediterranean Sea (Aljohani et al., 2021; Wood et al., 2021). This is likely attributed to the higher degree of mechanical mixing during winter induced by increased ambient current velocities. Some studies have shown that when a high salinity brine and a thermal discharge are simultaneously released, a substantial degree of initial mixing occurs. Subsequently, the negative buoyancy of the brine plume is largely negated, preventing downward movement in the water column (Fernández-Torquemada et al., 2009; Wood et al., 2021). The result is a reduction in spatial extent of the combined plume, as well as a reduction in propagation velocities.

It is difficult to evaluate the effects of brine and thermal plume dispersal in an open sea condition, given the absence of a land-boundary and sharp bathymetric slopes. In fact, the bedslope has a pronounced enforcing effect on the far-field dispersal of brine (Wood et al., 2021; Fernández-Torquemada et al., 2009). In order to assess the impacts and implications of brine- and thermal discharge, it is critical to assess the ecological effects of such effluents.

Ecological effects of brine discharge

It is evident that in order to produce ultrapure water for hydrogen electrolysis, utilizing SWRO desalination is potentially harmful to the marine environment (Omerspahic et al., 2022). SWRO has several harmful byproducts, such as heavy metals, anti-fouling agents, chlorine, acids and hypersaline brine (Frank et al., 2017). Hypersaline brine is considered to be the most impactful byproduct of the desalination process as it alters local hydrography and interferes with physiological processes of a large share of marine biota (Belkin et al., 2015). Studies on the harmful effects of desalination and its saline byproducts have been conducted on a global scale. An overview of existing literature on this topic is shown in Table 2.

Table 2. *The impact of salinity increases on global marine ecosystems*.

Location	Species	Salinity (psu)	Salinity effects	Reference
Mediterranean coast of Israel	Phytoplankton	40	Cell number decrease with increasing salinity	Drami et al. (2011)
Eastern Mediterranean	Phytoplankton	38.8-45.5	Rapid declines in primary productivity and microbial diversity	Belkin et al. (2015)
Monteray Bay, California, Pacific Ocean	Topsmelt, sand dollar, purple urchin, mysid shrimp, kelp, mussel, sea snail	35-70	Significant developmental inhibition in larval stages, growth rate reduction.	Voorhees et al. (2013)
Balearic Islands, northwest Mediterranean, Spain	Shallow seagrass	37-45	Increase in nitrogen content in leaves, high frequency of necrosis marks, decrease in non-structural carbohydrate content – high sensitivity to salinity changes.	Gacia et al. (2007)
Murcia, southeastern Spain, Mediterranean	Shallow seagrass	38.4 & 39.8	Necrosis marks, lower population density, significant reduction of leaf size, overload in epiphytes.	Sanchez-Lizaso (2008)
Spencer Gulf, south Australia, Great Australian Bight	Cuttlefish	> 40	Higher salinity reduced embryo survival, with none surviving above 50 psu, and decreased mean specimen weight and mantle length.	Dupavillon & Gallander (2009)
Eastern coast of Japan, Pacific Ocean	Bivalves, sea bream, flounder – specimens and larvae	50-70	Bream experienced body darkening at 50 psu after 30 min, lethal after 24 hours. Flounder larvae experienced increased death rate at 60 psu. Flounder eggs stopped hatching at 60 psu. Bivalves could not survive 70 psu. Bream showed avoidance by migration.	Iso et al. (1995)
New South Wales, Australia, Tasmanian Sea	Benthic community: polychaetes, amphipods, copepods, shrimp, gastropod, bivalve, crab	50-65	Inhibition of motility, reduction of burrowing activities, embryotic death, increased stress levels, reproductive inhibition.	Remaili et al. (2018)
Monteray Bay, California, Pacific Ocean	Ricefish	> 35	Embryotic deformities, hatching percentage decrease, swim bladder inflation, median day to hatch increase.	Kupsco et al. (2017)
Canary Island coast, Atlantic Ocean	Amphipoda, Copepoda, Cumacea, Mysidacea, Nematoda, Oligochaeta, Ostracoda, Polychaeta, Sipuncula, Tanaidacea and Turbellaria	44-46	Avoidance by migration, large scale decrease in population size.	Riera et al. (2011)

Note. Table 2 shows a summary of literature findings on the impact of increased salinity on global marine ecosystems. Salinity is measured in Practical Salinity Units (psu). Species also found in the North Sea are underscored.

The vulnerability of marine organisms to salinity changes is governed by several factors. One of these factors is their motility (Missimer & Maliva, 2018). Mobile organisms can exhibit avoidance behaviour in response to increased salinity (Kültz, 2015). For instance, Iso et al. (1995) noted that bream juveniles migrated to less saline areas when the salinity exceeded 50 ppt. However, another factor that governs susceptibility to salinity changes is the ability for osmotic regulation. A significant portion of marine (in)vertebrates are considered to be ineffective osmotic regulators when it comes to large salinity changes, as osmotic regulation is an energetically demanding process (Rivera-Ingraham & Lignot, 2017). As a result, marine macro- and meiofauna experience physiological constraints due to the dispersion of brine. These constraints include increased oxygen consumption (Kupsco et al., 2017), a reduction in individual weight and size (Dupavillon & Gallander, 2007), a darkening of the body (Iso et al. 1994) and a heightened mortality rate (Riera et al., 2011). However, more halotolerant species such as topsmelt and crabs were identified, which remained relatively unaffected up to 60 ppt in salinity.

Marine flora such as oceanic seagrass are susceptible to damage from salinity increases due to their sessile nature, as well as their inability to provide sufficient osmotic regulation in high salinity environments. As a result, oceanic seagrass was shown to exhibit a high frequency of necrosis marks, significantly reduced leaf sizes, increased nitrogen content and lower population density resulting from a relatively weak increase in salinity (Gacia et al., 2007; Voorhees et al., 2013).

The marine microbiome has been shown to deteriorate as a result of brine disposal driven salinity increases (Belkin et al., 2015). The study investigated a thermally stratified water column for a summer scenario in the and a homogeneous water column for a spring scenario in the Eastern Mediterranean. They found that photosynthesis was supressed due to salt stress, as well as near immediate decreases in chlorophyll-a and photosynthetic pigment. Heterotrophic species increased bacterial productivity due to salinity stress, while halosensitive species underwent immediate death. A field study on the effects of desalination brine on the microbial community was performed by Drami et al. (2011). They found that in spring and winter, a 60% reduction in average chlorophyll a content occurred, while in summer the reduction was 32%. It should be noted that this field study investigated a brine discharge that was also elevated in temperature.

Reproductive processes are significantly negatively impacted due to observed increases in salinity, which contributes to the decline in populations of marine meio- and macrofauna. A widely found effect is the delayed hatching of macrofaunal eggs, found in species such as cuttlefish (Dupavillon & Gillanders, 2007), flounder (Iso et al., 1995), shrimp (Remaili et al., 2018) and ricefish (Kupsco et al., 2017). Furthermore, fauna in the embryotic and larval stages were shown to have increased mortality rates, as well as increased frequency of deformities and decreased growth rates (Remaili et al., 2018).

Del Bene et al. (1994) highlighted the stratifying effect of brine dispersal. The disparity in density between brine and seawater leads to the development of stratification. Consequently, the brine forms a saline bottom layer that can significantly impact benthic communities (Riera et al., 2012). It was found that the total macrobenthic assemblage was negatively influenced by a local brine discharge. However, changes in sediment particle size distribution resulting from the turbid discharge stream were observed, which may have positively influenced the populations. Reproductive processes that involve utilization of the benthic environment (laying of eggs, hatching etc.) can be negatively influenced by the saline bottom layer formation (Del Bene et al., 1994).

A crucial distinction between the findings in existing literature and the methodology proposed in this report is that of environmental context - the impact of brine discharge, as studied in the literature, applies to a coastal environment. In contrast, the methodology in this report is applicable to an open shelf sea setting. This is an important distinction as brine dispersal and its effect in an open shelf sea setting may differ substantially compared to a coastal setting. Firstly, bed shear effects differ between the two settings as in coastal environments the seabed gradient is significantly higher, as well as the occurrence of much shallower water depths, especially in the North Sea (Stanev et al., 2009). Secondly, coastal processes such as wave-induced mass fluxes and longshore drift govern the dispersal of water in proximity to the coast, whereas these processes do not apply to open ocean conditions (Bosboom & Stive, 2021). This may significantly change the dispersal and long-term dilution of brine. Lastly, ecological effects may differ between the two settings due to the contrast in biodiversity and density (Gray, 1997). In coastal settings, impact due to brine wastewater may be substantially higher as marine populations may be denser and more diverse. However, they may also be more resistant to changes in salinity (Boyd & Brown, 2015). Given the limited availability of literature

on open sea effects of brine wastewater, the effect of brine on an open sea ecosystem remains unknown.

In conclusion, there is a consensus in the current understanding of the effects of brine discharge on the aquatic environment, specifically regarding its widespread negative impacts on marine ecosystems. Studies have shown that brine discharge leads to significant reductions in population density, inhibited reproduction, and impaired physiological processes in flora, fauna, and microbes across a salinity range of 40-70 ppt. Benthic communities appear particularly vulnerable due to density stratification caused by brine discharge. Existing research primarily focuses on coastal environments. It remains uncertain whether these findings are applicable to brine discharge at sea.

Ecological effects of coolant discharge

The effects of thermal effluent in the marine environment have largely been investigated within the context of coastal power plants, and laboratory experiments. Table 3 shows an overview of existing literature regarding the effects of coolant on temperate marine ecosystems.

Table 3. *The impact of increased water temperature on temperate marine ecosystems.*

Location	Species	Temperature increase over ambient (ºC)	Effects of heat stress	Reference
Narragansett Bay, north-east USA	*Arcartia tonsa* (marine copepod)	6.4	Significant decrease in respiration rate: from 9.2 (intake) to 3.4 (discharge) [µl O_2/h (100 animals)]	Capuzzo (1980)
Hamnefjärden Bay, south-east Sweden	Eurasian Perch	4 to 8	Disturbed reproductive processes: egg spawning occurred earlier, increased egg mortality, decreased egg strand quality. Warmer effluent attracted fish at the expense of reduced reproductive performance.	Sandström et al. (1997)
Laboratory experiments	Sockeye Salmon, Brook Trout, Juvenile Bluefish, Atlantic Mackerel	1.5 to 5.6	Small temperature increases (< 2ºC) induced decreased swimming speeds in trout, loss of equilibrium in bluefish. Higher temperature increases > 2ºC induced temporary swimming speed increases. Increased hatching speed occurred in salmon.	Shiomoto & Olson (1978)
Laboratory experiments	Yellowtailed Fusilier, Five-lined Cardinalfish	3	Immediate stress responses (first week of exposure) were doubled blood glucose levels, increased metabolic O_2 transport and changes in gill morphology. After 3-5 weeks, physiological parameters began stabilizing.	Johansen et al. (2021)
Daya Bay, eastern China	Phytoplankton	2 to 5	Structural changes in phytoplankton abundance and community structure. Photosynthetic activity was negatively correlated with temperature. Growth of harmful algal species is favoured.	Hu et al. (2023)
Haizhou Bay, north-east China	Phytoplankton	1 to 5 & <1*	Significant shifts in abundance and composition both in- and outside of the discharge area during summer months. Higher proportions of diatoms inside heated area during summer.	Zhang et al. (2023)
Daya Bay, eastern China	Phytoplankton	Up to 5.6	Large-scale shift in abundance of diatoms to dinoflagellates when temperatures reached a 3.7ºC differential compared to ambient	Li et al. (2011)
Haizhou Bay, north-east China	Pacific Oyster	2 to 10	Increased water temperatures promoted growth of oyster shells, the effect being most significant in winter. Thermal discharge negatively affects gonadal and soft parts development, as well as their filtration rate.	Dong et al. (2018)

Note. *Values obtained from previous study in the same area (Nie et al., 2021).
Aquatic species also found in the North Sea are underscored.

Various laboratory experiments have shed some light on the reactions of different fish species to temperature changes. Shiomoto & Olson (1978) observed that when water temperatures were moderately adjusted (ranging from 1.5 to 5.6 ºC), there were noticeable alterations in the swimming speeds and spontaneous activity of the fish. For instance, the Brook Trout exhibited a reduction in swimming speed when the water temperature was raised to 21.0 ºC from 18.9 ºC. Similarly, juvenile Bluefish experienced a loss of equilibrium when subjected to a temperature increase of 1.5 ºC to 2.6 ºC. The research also highlighted changes in reproductive processes. A decrease in hatching times by 24 days was observed when Atlantic

Salmon were exposed to a 5 ºC increase in water temperature. Comparable findings were recorded in a study of Eurasian Perch in a small bay in South-East Sweden, where a temperature rise of 2-4 ºC resulted in earlier spawning of juveniles (Sandström et al., 1997). Temperature elevations of 5 ºC led to a higher mortality rate among eggs, primarily due to increased susceptibility to bacterial and fungal infections.

Johansen et al. (2021) explored the metabolic and cardiorespiratory changes in coral reef fish under thermal stress caused by a 3 ºC increase in water temperature. The study found that the elevated temperatures triggered significant changes in the metabolic and cardiorespiratory systems of the fish species examined. During the initial two weeks of the five-week study period, there were significant increases in metabolic rates, heart rate, respiratory rate, and oxygen uptake, indicating substantial physiological stress due to prolonged thermal exposure. In one of the two species studied, over half of the individuals did not survive the five-week period. After four to five weeks of continuous exposure to elevated water temperatures, most parameters returned to their original values. However, lasting effects were observed, the most significant being a reduced release of red blood cell stores, suggesting less efficient oxygen circulation.

Phytoplankton are cited to be more sensitive to thermal effluent, given their natural sensitivity to chemical- and temperature changes (Zhang et al., 2023). In temperate marine ecosystems such as the North Sea, seasonal variations in phytoplankton populations can contribute to different response to thermal stress and are thus important to consider. Zhang et al. (2023) investigated the influence of thermal discharge from a nuclear power plant across a 5-year study period in Eastern China. The affected area was defined as waters experiencing a temperature increase of 1 ºC compared to baseline conditions. Results showed that phytoplankton abundance and community structure were affected most during summer, with a shift to better adapted species to thermal stress. Furthermore, an increased proportion of diatoms and decreased proportion of dinoflagellates was systematically recorded in summer months. Interestingly, no statistically significant effect on abundance and composition was found from autumn to spring.

A similar study conducted by Begun & Maslennikov (2021) in the Sea of Japan likewise highlighted the importance of seasonality, where thermal pollution effectively extended the phytoplankton summer to autumn growth period by up to 2 months. This prevented winter freeze-up in the intake area, delaying the start of winter growth compared to unaffected areas. The increased production capacity of the plant, combined with thermal pollution, caused significant reduction in phytoplankton density and biomass during colder periods. Although mechanical factors within the system may contribute to these differences, their impact on phytoplankton abundance is considered minor. The rise in water temperature by 5–6 °C during the cold season negatively affected microalgae, impairing their photosynthetic activity and abundance.

Li et al. (2011) conducted a study analysing the phytoplankton community at a similar site in Eastern China over a span of multiple decades, from 1982 to 2005. Throughout the 23-year observation period, a significant transition towards dinoflagellate dominance was observed, ultimately constituting 50% of the total phytoplankton abundance. Meanwhile, the contribution of diatoms decreased by nearly 30% over the duration of the study. This shift from diatom predominance to dinoflagellate prevalence occurred when temperatures reached a threshold difference of 3.7 ºC due to thermal effluents compared to ambient temperatures. Interestingly, these results highlight an opposite pattern compared to the results published in Zhang et al. (2023), where dinoflagellate abundance rose as a result of thermal effluent.

Furthermore, Hu et al. (2023) found that thermal effluent can lead to elevated nutrient concentrations, particularly dissolved inorganic nitrogen and dissolved inorganic phosphorus, especially near the discharge point. This alters nutrient ratios, shifting towards phosphorus limitation for phytoplankton growth, exacerbating eutrophication trends. Phytoplankton abundance varies spatially, with lower levels at the discharge site but higher near the outlet, potentially increasing harmful algal blooms. Thermal discharge also alters phytoplankton community structure, favouring smaller size fractions, impacting trophic interactions. Additionally, fluorescence measurements indicated reduced photosynthetic efficiency under high temperatures, affecting phytoplankton physiology, although they can recover away from these regions. Long-term changes in community composition may result from differential species responses to thermal stress.

Similar to animals residing within the water column, benthic filter feeders such as oysters have been shown to be impacted by thermal discharge. In a study conducted by Dong et al. (2018), the development of both soft tissues and shells of Pacific Oysters were analysed in Haizhou Bay, where water temperatures where observed to gradually increase towards 2 ºC higher than ambient as a result of thermal discharge. It was found that thermal effluent positively influenced shell growth across all dimensions, with the most pronounced effects observed during the winter months. However, the rise in temperature had adverse effects on gonadal development and the growth of soft tissues. It is important to highlight that the growth of soft tissues has been demonstrated to heavily rely on nutrient availability, which is essentially reflected in the phytoplankton density for benthic filter feeders, as elucidated by Liu et al. (2010). In the study by Dong et al. (2018), it was consistently noted that phytoplankton density remained higher at sample stations characterized by lesser temperature elevation compared to those stations subjected to higher temperature elevations resulting from thermal discharge. This finding underscores the cascading impact of thermal pollution on inhibiting phytoplankton density, thereby affecting the growth and reproduction of benthic filter feeders.

The presented body of evidence suggests that thermal pollution imposes measurable stress on both planktonic and benthic marine fauna. These stresses are found in terms of reduced reproductive performance, inhibited mobility, changes in community structure and size, and increased metabolic rates. It is important to note that the cooling systems of devices like electrolysers introduce additional ecological stressors, including chemical and mechanical strains (Guimaraes et al., 2023). These factors could complicate the process of independently quantifying the impacts of these stressors.

3. Methods

The Delft3D Suite

Delft3D-FLOW is a versatile numerical model distinguished by its application in hydrodynamic studies. Its foundational equations contain the dynamics of fluid flow, accounting for the various forces and processes governing water movement. The core equations of this model comprise the Navier-Stokes equations, expressed in a form suitable for computational fluid dynamics. These equations represent the conservation of momentum in the horizontal directions, coupled with the continuity equation ensuring mass conservation. Coriolis force, gravitational acceleration, and the effects of varying water levels are integrated into the equations, enabling the simulation of tidal and wind-driven flows. Key parameters such as horizontal and vertical eddy viscosity and diffusivity coefficients play crucial roles in modelling turbulent processes. These coefficients, determined by a combination of empirical constants and physical properties, govern the dispersion of momentum, heat, and constituents within the water body. Temperature dynamics are addressed through an additional transport equation, accounting for advection, diffusion, and external heat sources. This equation provides insights into thermal variations, essential for understanding phenomena such as thermal discharge and effluent dispersion. Turbulence modelling forms an integral part of Delft3D-FLOW, with options including the k-ε, k-L, algebraic, and constant coefficient models. These models allow for the characterization of turbulent processes, enhancing the fidelity of simulations. In practical applications, the model accommodates diverse scenarios, from Cartesian to spherical coordinates, and offers flexibility in boundary conditions and input parameters. It seamlessly integrates with other modules within the Delft3D suite, facilitating comprehensive studies encompassing both hydrodynamics and water quality. Beyond its hydrodynamic capabilities, Delft3D-FLOW addresses vertical exchange processes through turbulence closure schemes, ensuring accurate representation of near-field phenomena. This feature is particularly relevant in assessing the environmental impact of wastewater discharge and thermal effluents. For further examination of the physical phenomena and modules considered during their implementation, reference is made to the Delft3D-FLOW user manual (Deltares, 2024).

Model configuration – Outer model (GETM)

For this study, a pre-validated large-scale hydrodynamic model was used as an outer framework, feeding all necessary boundary conditions to a nested high-resolution Delft3d-FLOW simulation. The large-scale model used is the General Estuarine Transport Model (GETM), a model that is openly accessible via www.getm.eu (Burchard and Bolding, 2002). GETM operates as a fully baroclinic model, including sea surface elevations, current dynamics, land cell inundation and drying, and temperature- and salinity distributions. To delineate vertical processes, GETM incorporates the General Ocean Turbulence Model (GOTM). GETM uses generalized vertical coordinates and a spherical, staggered C-grid layout in the horizontal plane. For more information about this model, a comprehensive overview and validation by Van der Molen et al. (2016) can be referred to. The grid and domain used for GETM, along with the position of the high-resolution nested grid are illustrated in Figure 6. It should be noted that the GETM setup utilized in this study as portrayed by Figure 6 does not fully encompass the total grid as used in Van der Molen et al. (2016); rather, the grid was modified to only contain the North Sea.

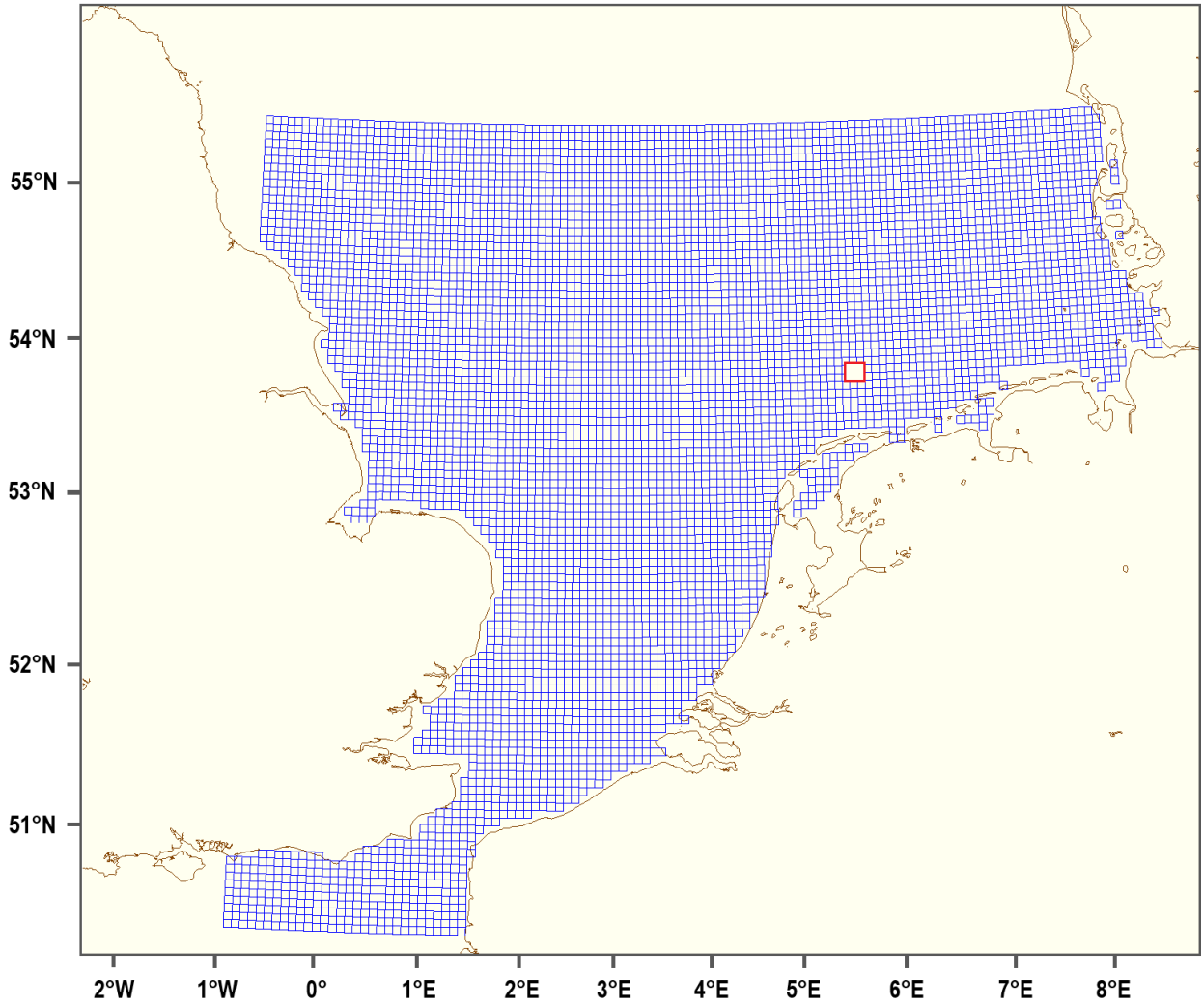

Figure 6. *The grid domain utilized by the General Estuarine Transport Model (GETM).*

Note. The outer grid utilized by GETM is portrayed with blue lines. The location and relative dimensions of the high-resolution nested Delft3D grid are displayed in red.

Meteorological data provided by the European Centre for Medium-Range Weather Forecasts (ECMWF) ERA-5 and Operational Analysis Hindcasts was used to force the model. This data includes parameters such as pressure, air temperature, windspeed at 10 meters height, dew point humidity and total cloud cover on an hourly interval. Tidal constituents of the model were derived from TOPEX-POSEIDON satellite altimetry data (Le Provost et al., 1998). The bathymetry for the model was sourced from the Northwest European Shelf Operational Oceanographic System (NOOS) database at www.noos.eurogoos.eu. Depth-resolved temperature and salinity boundary conditions were obtained from ECMWF-ORAS4 (Ocean Reanalysis System) (Balmaseda et al., 2013; Mogensen et al., 2012). Subsequently, the GETM configuration was executed for both January 2019 and July 2019 to establish boundary conditions for the nested Delft3d-FLOW model for both a winter and summer scenario.

Model configuration – Grid

To optimize both detail and computational efficiency in the high-resolution Delft3D-FLOW model, a Cartesian grid measuring 15 km by 15 km was devised. In order to balance detail and simulation time, grid cell sizes were set as variable. The central grid cells were set at 40 by 40 meters to capture fine-scale features of discharge dispersion, coursing outward to a resolution of 800 by 800 meters in the outermost cells. Bathymetric data obtained from the GETM was used to interpolate water depth over the high-resolution grid. The grid dimensions and corresponding bathymetry are displayed in Figure 7. In the vertical, the grid was set at 25 equidistant layers, each corresponding to 4% of the total water depth.

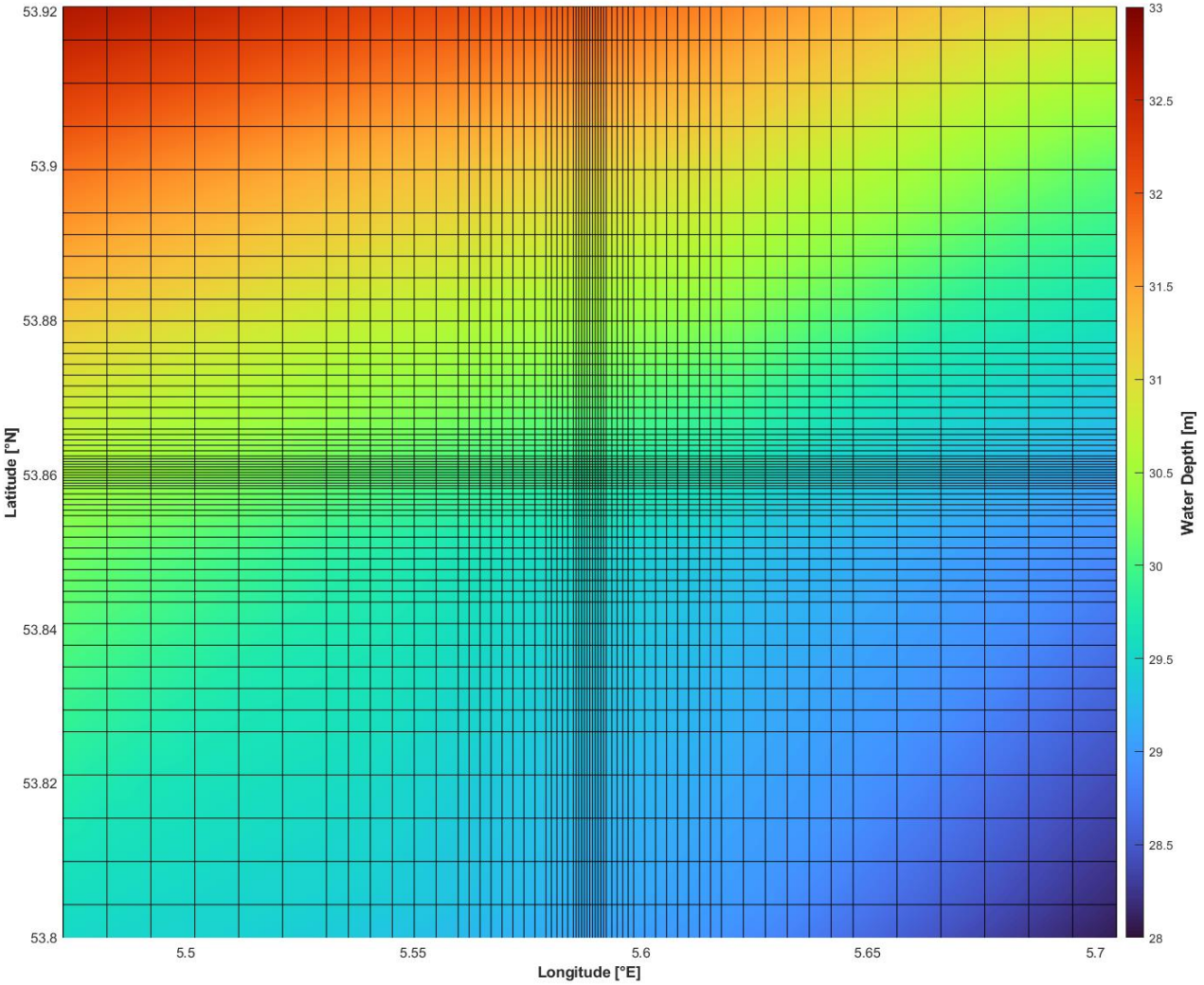

Figure 7. *High-resolution Delft3D grid* overlying the bathymetry of the study area.

Note. The high-resolution grid utilized in Delft3D. The total domain encompassed by the grid entails 15 by 15 kilometers. The grid cells are of variable size, with the finest grid cell resolution being 40 by 40 meters, and the coarsest grid cell resolution encompassing 800 by 800 meters.

Model configuration – Input parameters

An overview of the physical parameters and assumed constants are displayed in Table 4.

Table 4. *The physical parameters and input configuration of the Delft3D model*.

Physical parameter	**Value**	**Unit**
Air density	1	kg/m^3
Water density	1023	kg/m^3
Horizontal eddy viscosity	0.1	m^2/s
Vertical eddy viscosity	0.0001	m^2/s
Horizontal eddy diffusivity	0.1	m^2/s
Vertical eddy diffusivity	0.0001	m^2/s
Chézy roughness constant (u-direction)	65	-
Chézy roughness constant (v-direction)	65	-
Secchi depth	2	m
Dalton number for evaporative heat flux	0.0015	-
Stanton number for heat convection	0.00145	-
Input option	**Configuration**	
3D turbulence model	k-Ɛ	
Wall roughness slip condition	Free	
Heat flux model	Ocean	
Advection scheme - momentum	Cyclic	
Advection scheme – transport	Cyclic	
Discharge model	Normal	

Model configuration – Scenarios

A total of 14 model scenarios were run, the configuration of which is displayed in Table 5. In addition to runs including discharge, a zero-discharge reference scenario was run for both summer and winter simulations. This was done so that data obtained from the reference runs could subsequently be subtracted from results resulting from discharge runs, allowing for the depiction of salinity and temperature differences after the emission of wastewater. All discharges were invoked in the ‘normal’ setting, so the velocity of the discharge, dimension of the discharge pipe and the angle of outflow are not taken into account. This option was selected as no such data was available at the time of performing this study, and small-scale local flow interactions were deemed irrelevant given the scale of the study performed: such investigation is of larger importance only in weak dynamic systems where discharge-induced flows considerably influence ambient flows (Morelissen et al., 2013).

In the ‘combined’ simulations, brine and coolant were simultaneously discharged. For the coolant stream in these simulations, the ambient salinity from the centre cell (where the discharge occurs) was extracted as a time series from the reference runs. This salinity curve over time was subsequently set as the salinity value for the coolant. This approach ensures that the salinity signal from the coolant stream does not interfere with the salinity signal of the brine stream, which is essential due to the significantly higher coolant discharge rate compared to brine.

Table 5. *The configuration of simulation scenarios*.

Scenario number	Season	Electrolyser capacity [GW]	Wastewater flowrate [m^3/s]	Wastewater salinity [psu]	Wastewater temperature [ºC]
Brine simulations					
Scenario 1	Summer	0.5	0.055	52.5	18
Scenario 2	Summer	1.0	0.111	52.5	18
Scenario 3	Summer	5.0	0.555	52.5	18
Scenario 4	Winter	0.5	0.055	54.2	7
Scenario 5	Winter	1.0	0.111	54.2	7
Scenario 6	Winter	5.0	0.555	54.2	7
Coolant simulations					
Scenario 7	Summer	0.5	3.071	31.0	30
Scenario 8	Summer	1.0	6.142	31.0	30
Scenario 9	Summer	5.0	30.71	31.0	30
Scenario 10	Winter	0.5	3.071	32.0	19
Scenario 11	Winter	1.0	6.142	32.0	19
Scenario 12	Winter	5.0	30.71	32.0	19
Combined simulations					
Scenario 13	Summer	5.0	30.71	Ambient	30
			0.555	52.5	18
Scenario 14	Winter	5.0	30.71	Ambient	19
			0.555	54.2	7

Volumetric flowrates and TDS for brine were derived from equations 1, 2 and 3, assuming that the desalination unit of the electrolyser contains an ultrapure water recovery rate of 0.33, and the amount of ultrapure feedwater needed per kilogramme H_2 produced were assumed to be 11 L per kg H_2 (Shi et al., 2020). Note that the TDS of the brine discharged in winter is slightly elevated compared to that during summer, as surface salinity in winter is marginally higher. Volumetric flowrates for coolant were derived from equation 5, assuming that the electrolyser runs at a constant 70% efficiency, meaning that 30% of its total capacity is converted to heat. It is important to note that while current PEM electrolyser systems can achieve efficiencies of over 80% and are expected to become more efficient as technology progresses, the efficiency of PEM electrolysers decreases over their lifespan due to material wear (Scheepers et al., 2020). This wear leads to a gradual increase in heat generation. Therefore, for the purposes of this study, an average efficiency of 70% was assumed. Coolant temperature was set at 12 ºC above the average ambient temperature for both summer and winter over the simulated period. It was assumed that the electrolyser operates continuously at its full capacity, resulting in constant discharge flowrates.

The simulated period for all simulations was set at 10 days, with calculated timesteps of 18 seconds. For the winter scenarios, the simulation period was configurated from 13 January 2019, 0:00h to 23 January 2019, 0:00h. The simulation period for the summer scenarios was set at 10 July 2019, 0:00h to 20 July 2019, 0:00h. The simulation periods were set in such a way that both periods encompassed the same phase of the spring-neap tidal cycle. The smoothing period was set at 0 hours. Map results were saved at an hourly interval.

Model configuration – Forcings

The wind data originating from GETM for both the summer and winter simulation periods were applied as open boundaries. Figure 8 visualizes the wind speeds and direction as wind roses, with wind speeds averaged over the Delft3D grid and transformed to vectors for both simulation periods. In order to assess whether the governing winds were characteristic in velocity, direction and variability, the same wind roses were plotted for summer months July, August and September, and for winter months January, February and March for the years 2017, 2018, and 2019. The results are displayed in Appendix A.

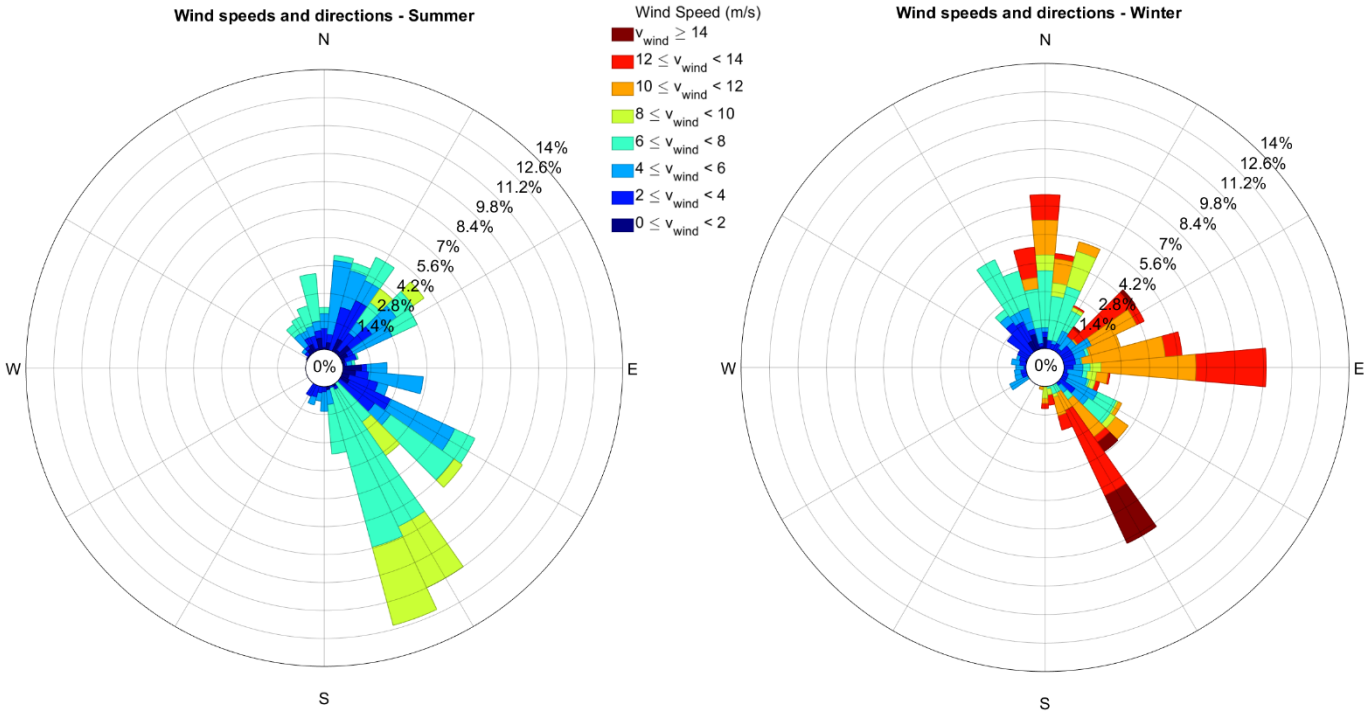

Figure 8. *Average wind speed at 10 meter elevation over the simulated domain for summer (10th to 20th of July 2019) and winter (13th to 23rd of January 2019).*

Similarly, the sea surface level data from GETM, indicative of the tidal cycle, were applied as open boundary forcings. Figure 9 shows the sea surface level at the discharge point.

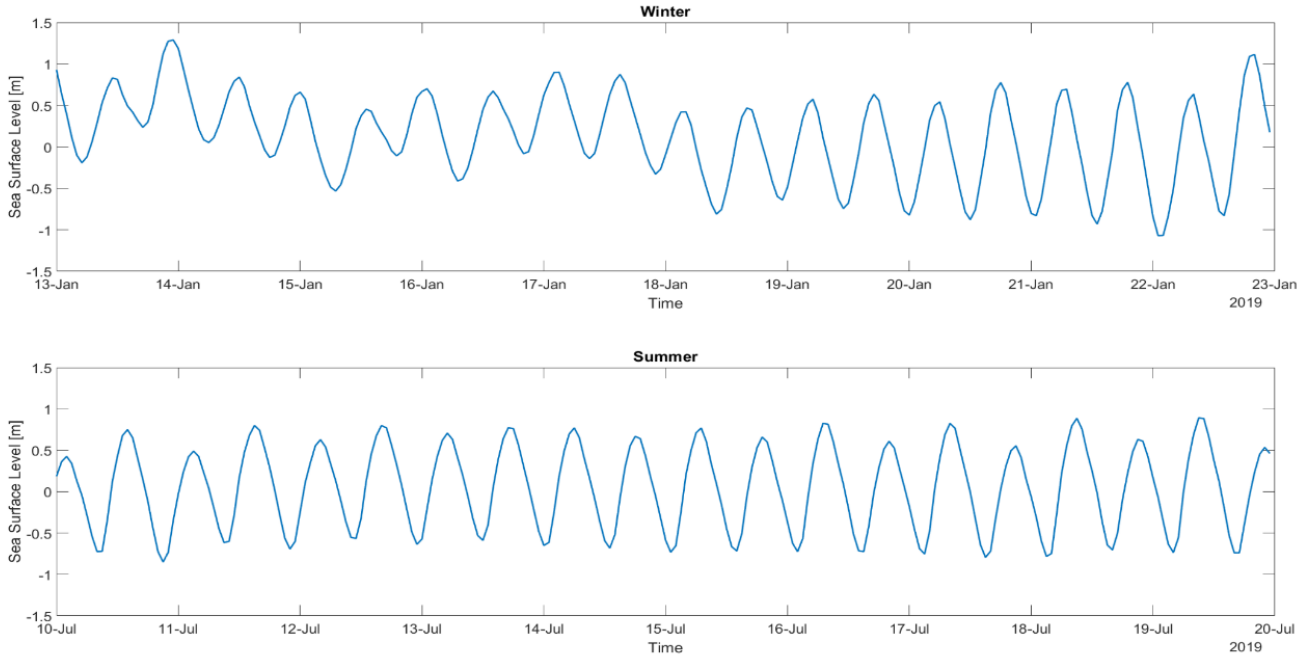

Figure 9. *Sea surface level over simulation time for winter (top) and summer (bottom)*.

Results

Average temperature and salinity distribution – no discharge

In order to investigate the effect of the simulated discharge types within the TNW area, it is critical to firstly assess the base hydrodynamic conditions of the domain. In Figure 10, the average vertical distribution of salinity is depicted for both 10-day simulation periods during summer (top) and winter (bottom). The cross-section is taken from the western to the eastern border of the simulation domain, across the latitude of the discharge point (thus 53.86 °N). The average standard deviation of salinity over the 10-day simulation periods was calculated and displayed in Table 6.

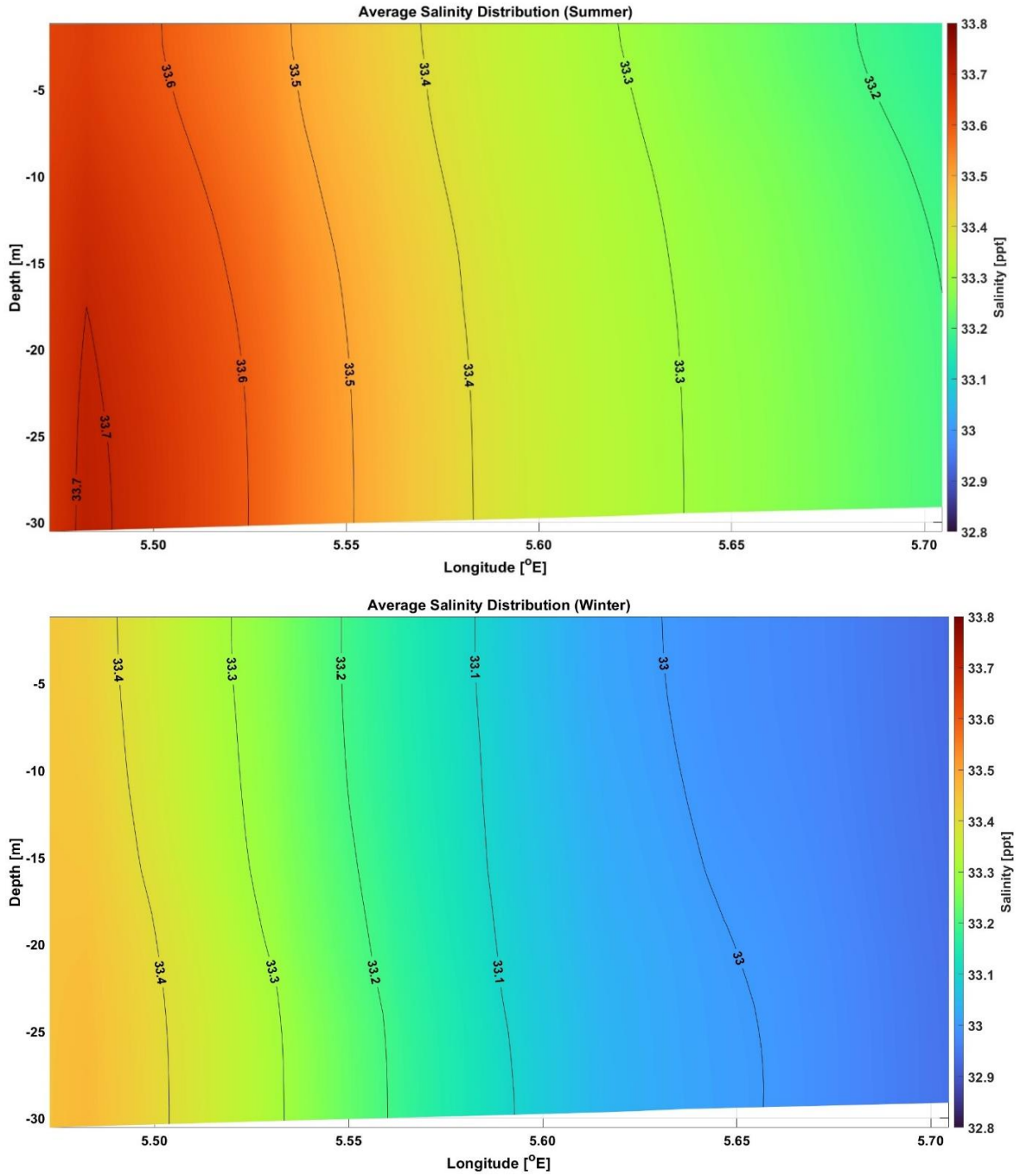

Figure 10. *Average cross-sectional salinity distribution for the summer (top) and winter (bottom) simulation scenarios.*

For the same 10-day summer (top) and winter (bottom) simulation periods, the vertical distribution of temperature was plotted within the same cross-section (Figure 11). Moreover, the average standard deviation of temperature over the 10-day simulation periods was calculated and displayed in Table 6.

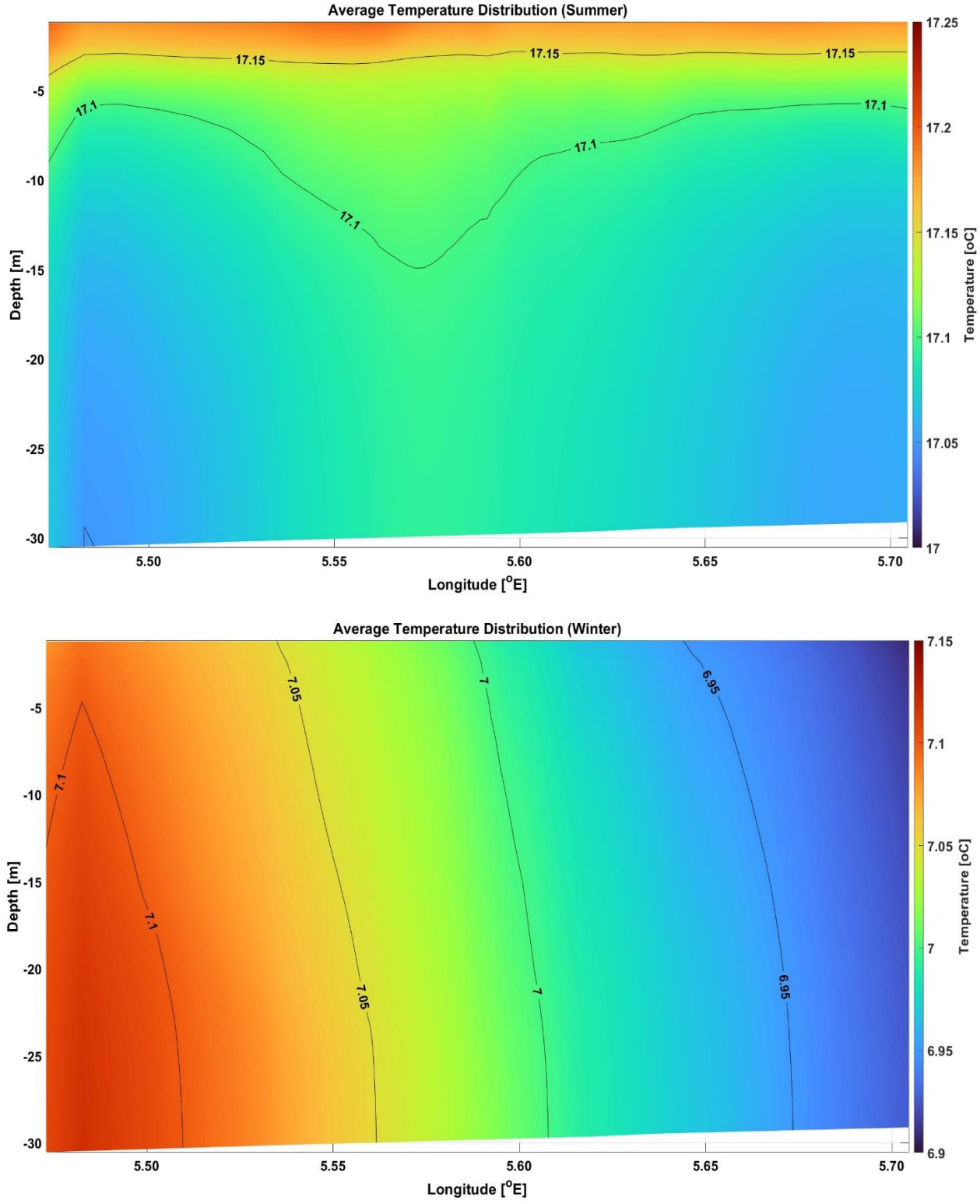

Figure 11. *Average cross-sectional temperature distribution for the summer (top) and winter (bottom) simulation scenarios.*

Table 6. *Average cross-sectional standard deviation in salinity and temperature for both 10-day simulation periods.*

Parameter	Season	Standard deviation
Salinity	Summer	0.1216 [ppt]
Salinity	Winter	0.1393 [ppt]
Temperature	Summer	0.0580 [°C]
Temperature	Winter	0.0487 [°C]

Averaged temperature and salinity change – surface layer

Figures 12 and 13 illustrate the variation in surface water temperature due to the discharge of coolant by a 5 GW electrolyser, with separate simulations for summer (Figure 12) and winter (Figure 13). These simulations are averaged over their respective durations.

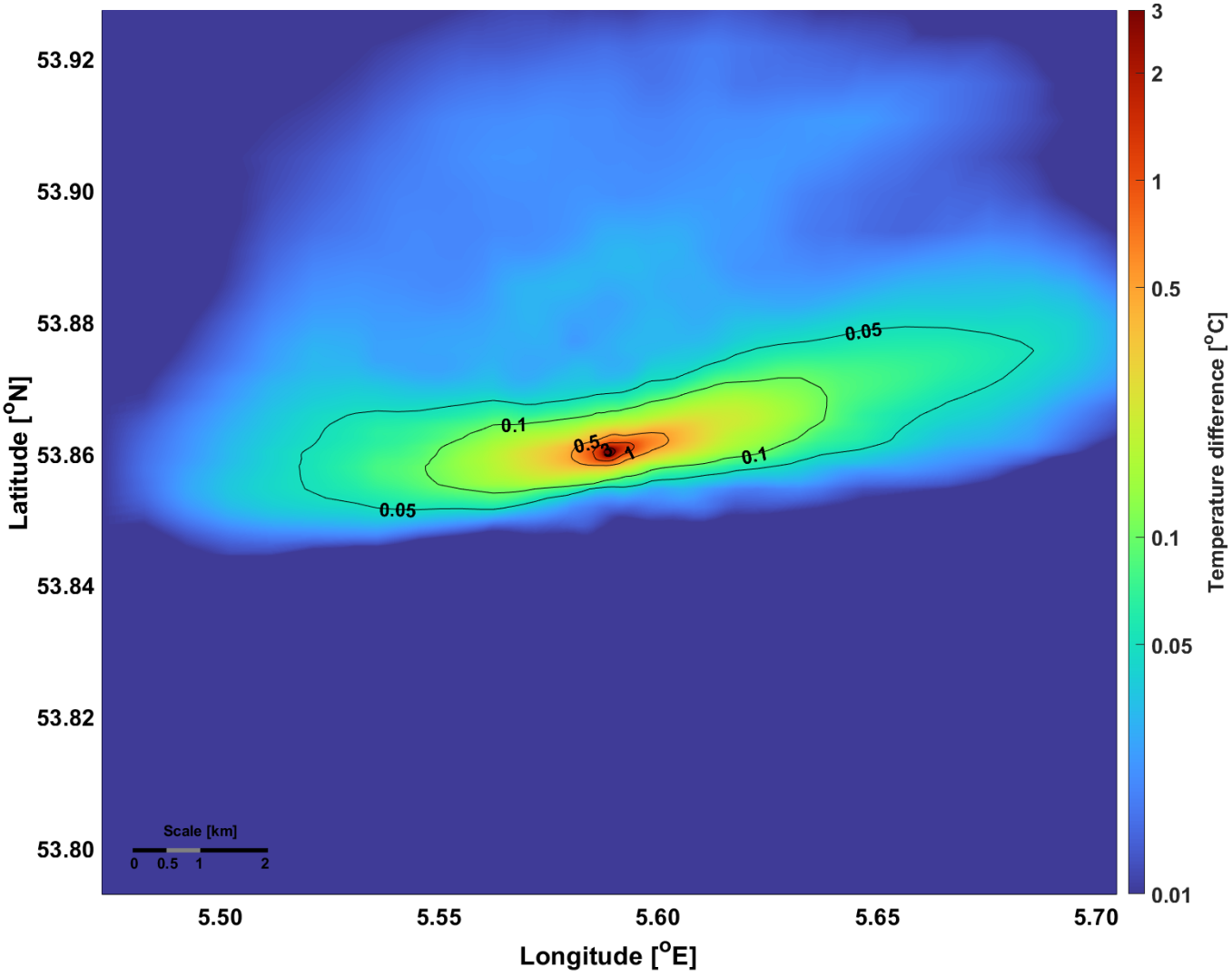

Figure 12. *Average sea surface temperature difference for a 5 GW electrolyser discharging coolant for the summer* scenario.

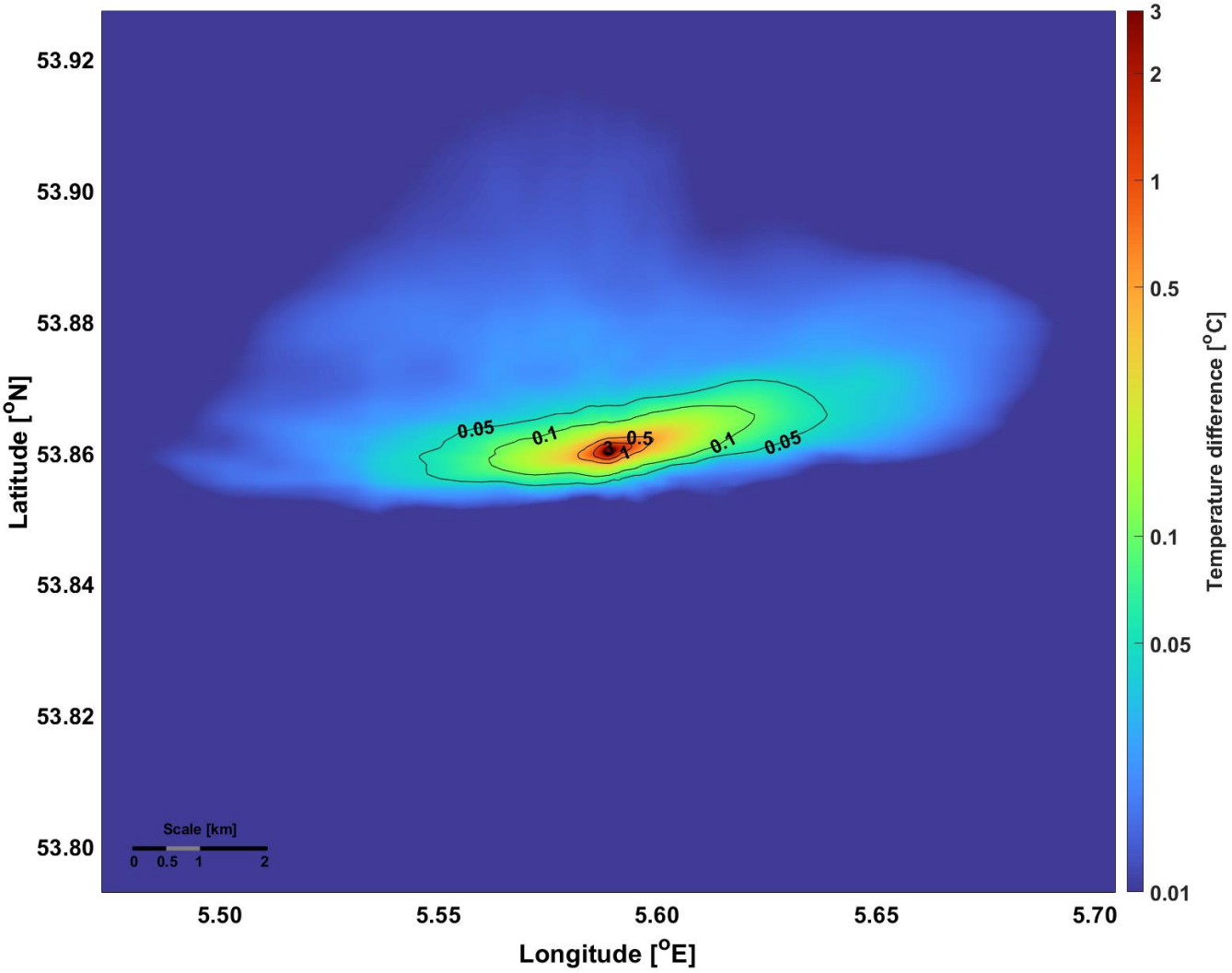

Figure 13. *Average sea surface temperature difference for a 5 GW electrolyser discharging coolant for the winter* scenario.

The data reveal consistent dispersion patterns across both seasons, characterized by a pronounced temperature gradient radiating from the discharge point. Temperature increases of 1 ºC or more are confined to the immediate vicinity of the discharge. The direction of diffusion is predominantly east-west for both summer and winter. No temperature differences are found south of 53.85 ºN during winter, and south of 53.84 ºN during summer. Around 1 kilometre east and west of the discharge point, the water temperature is on average ≤0.5 ºC above the ambient temperature, a finding consistent across both seasonal scenarios. However, the outer margins of the distribution show more extensive effects during the summer simulations compared to winter. As displayed in Appendix D to G, decreasing electrolyser capacity leads to a decreased in affected area in the surface layer, whilst showing the same general dispersion pattern. In conclusion, the surface area impacted by the average temperature change in the surface layer is smaller in winter than in summer.

Figures 14 and 15 illustrate the variation in surface water salinity due to the discharge of brine by a 5 GW electrolyser desalination unit, with separate simulations for summer (Figure 14) and winter (Figure 15).

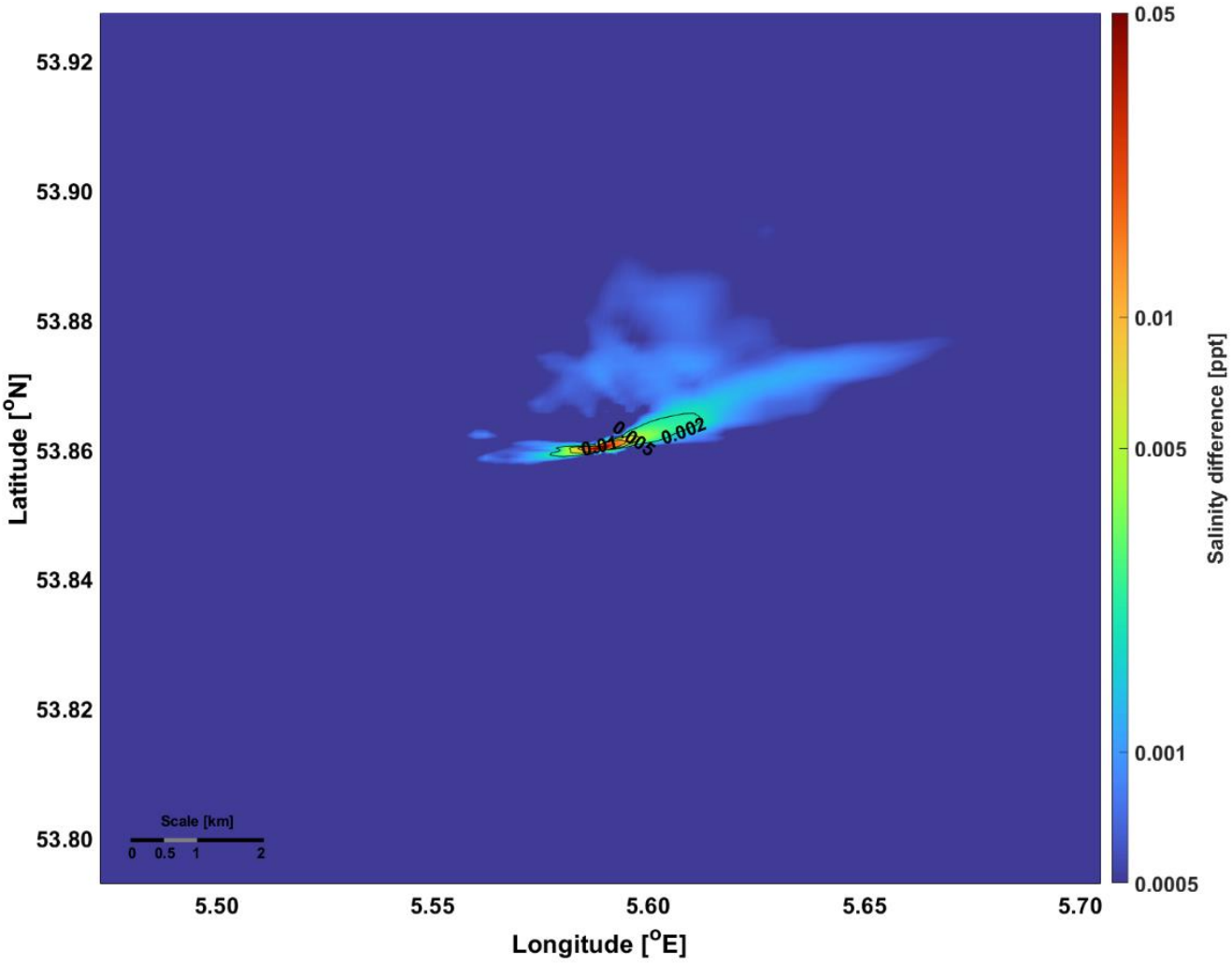

Figure 14. *Average sea surface salinity difference for a 5 GW electrolyser discharging brine during the summer scenario.*

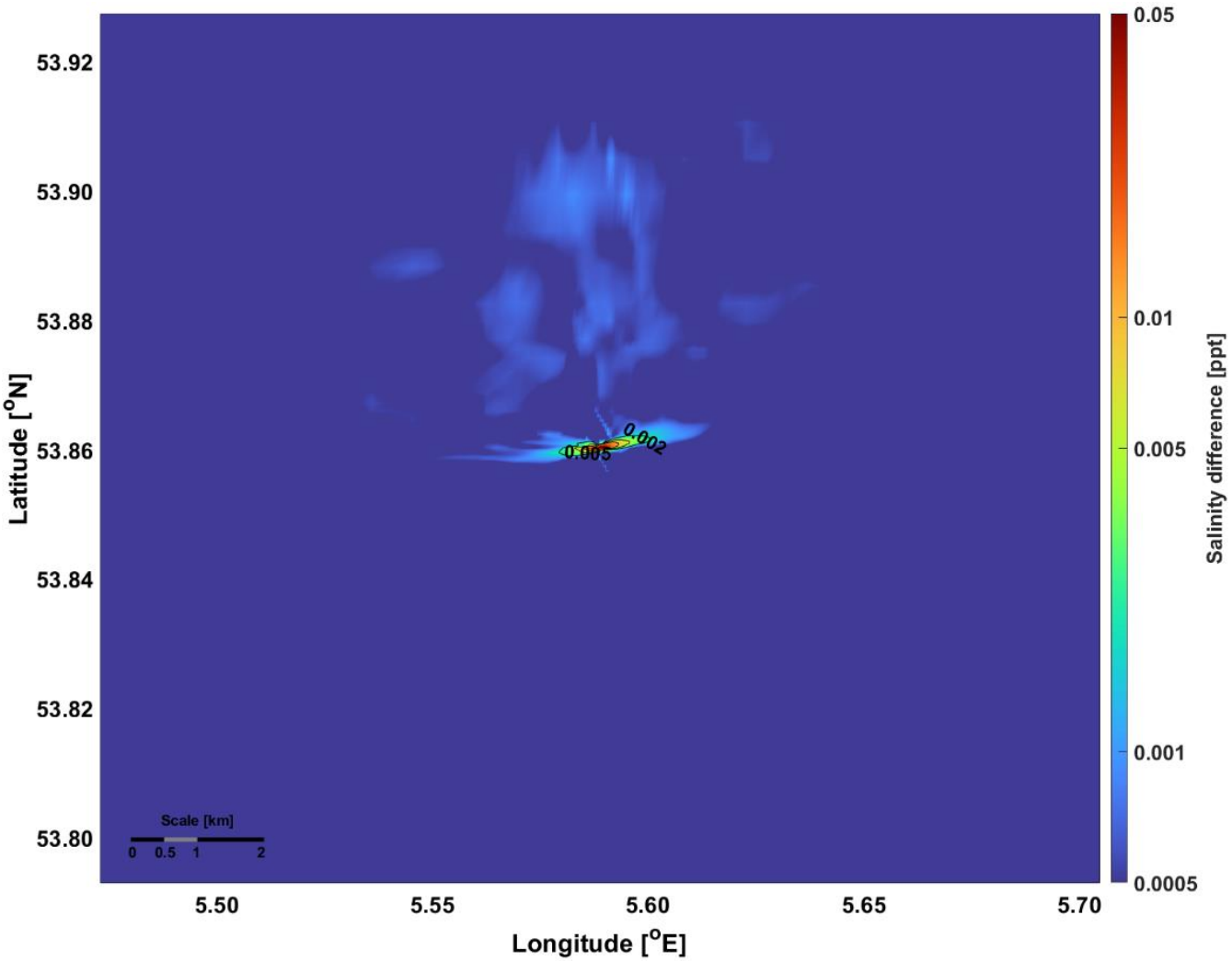

Figure 15. *Average sea surface salinity difference for a 5 GW electrolyser discharging brine during the winter scenario.*

The results show that sea surface salinity is only marginally affected by the discharge of brine in both summer and winter. In close proximity to the discharge point, salinity is on average heightened by 0.05 ppt, a value that rapidly decreases moving away from the discharge point. Similar to the results obtained from coolant discharge, the most significant surface salinity changes are found east and west of the discharge point, with the lowermost measured changes (≤0.001 ppt) only appearing in the northern part of the domain. In summer, larger salinity changes are found further away from the discharge point compared to winter, implying a larger impacted surface area. The sea surface salinity changes for lower electrolyser capacities are displayed in Appendix H to K. Here, similar dispersion patterns are visible, with the affected area greatly reduced.

In Appendix B and C, the average sea surface temperature difference resulting from the release of both salinity and coolant simultaneously is displayed for summer and winter respectively. No discernible difference in sea surface temperature was observed when compared to the results from coolant discharge alone.

For the same combined simulations, the average surface salinity difference for both summer and winter are displayed in Figure 16 and Figure 17 respectively.

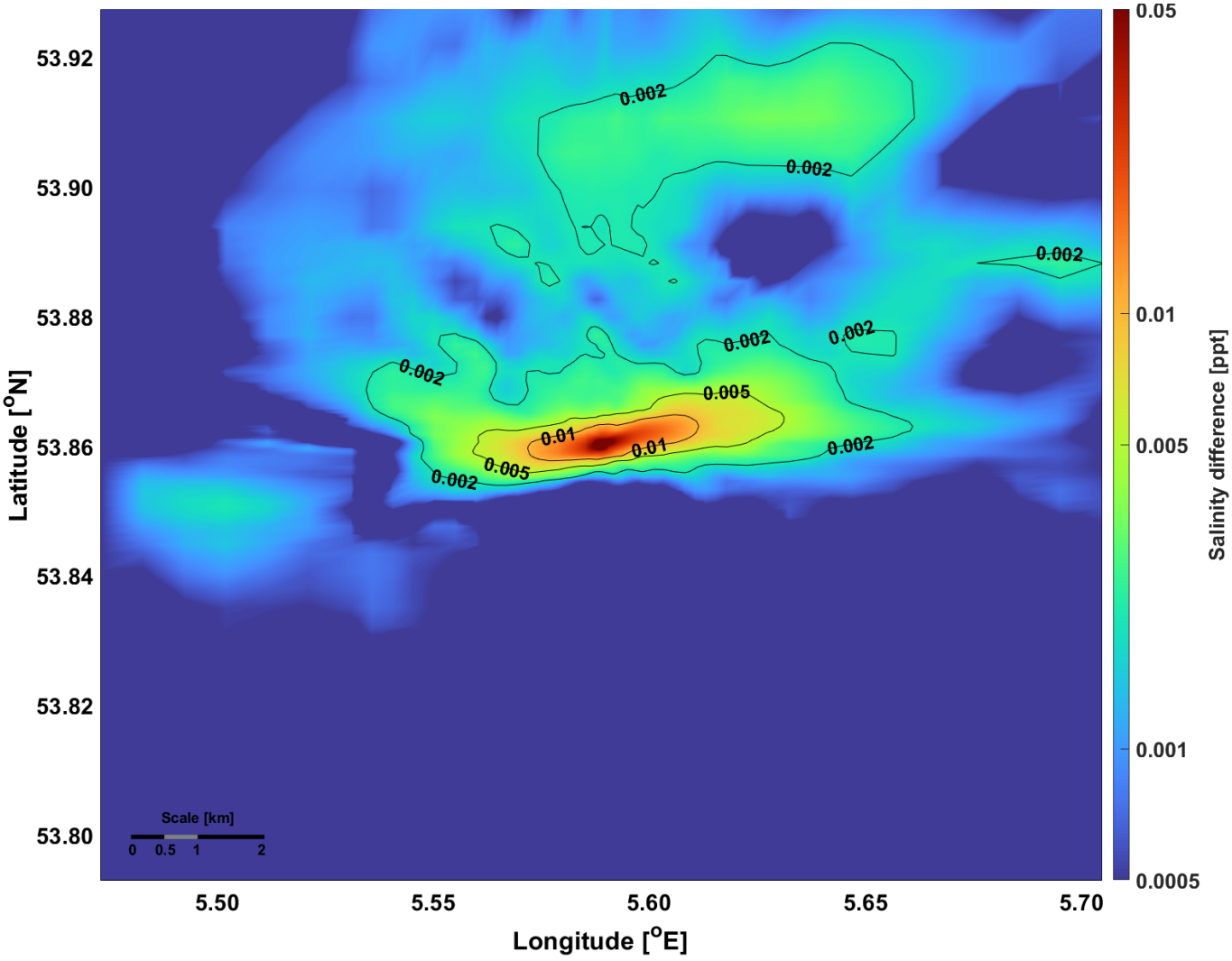

Figure 16. *Average sea surface salinity difference for a 5 GW electrolyser discharging both brine and coolant during the summer simulation*

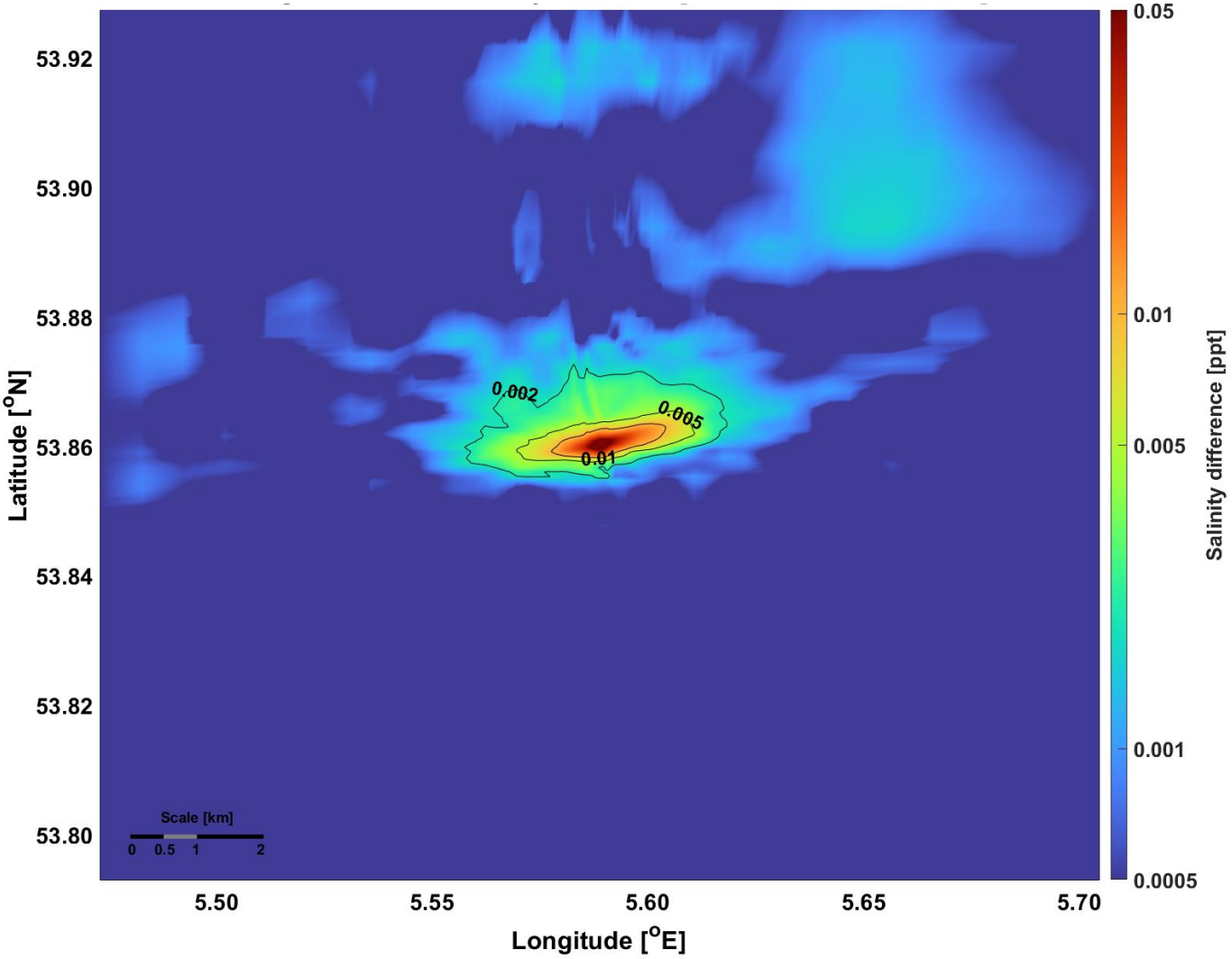

Figure 17. *Average sea surface salinity difference for a 5 GW electrolyser discharging both brine and coolant during* the *winter* simulation.

Figures 16 and 17 again reveal a generally east to west dispersion pattern of salinity, with the highest salinity differences found directly around the discharge point. The results found in the summer period show a greatly increased area of increased salinity both around the discharge point as well as in the far-field. For both seasons, scattering of lower (<0.002 ppt) salinity anomalies is found, generally in the northern part of the domain. The far-field salinity anomalies for summer are also higher in magnitude compared to winter. Compared to Figures 14 and 15, the surface area affected by salinity increases are significantly higher when discharges are invoked simultaneously. Furthermore, the salinity anomalies are found further away from the discharge point.

Averaged temperature and salinity change – vertical distribution

Figure 18 illustrates the average vertical extent of the temperature difference for summer, presented as a west-to-east cross-section across the latitudinal coordinate of the discharge point. Figure 19 shows the same result but for the winter simulation. These results depict the temperature elevation resulting from a 5 GW electrolyser discharging coolant at 12ºC above ambient temperatures.

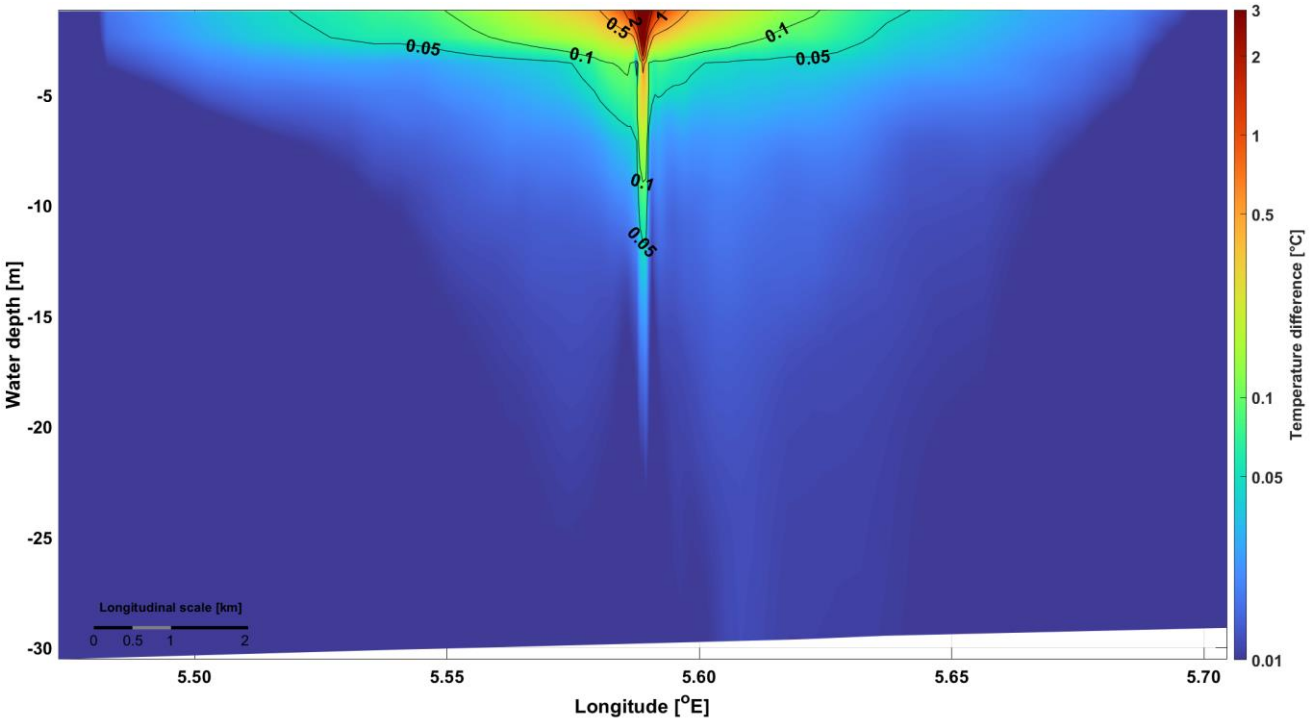

Figure 18. *Average cross-sectional temperature difference for a 5 GW electrolyser discharging coolant during summer.*

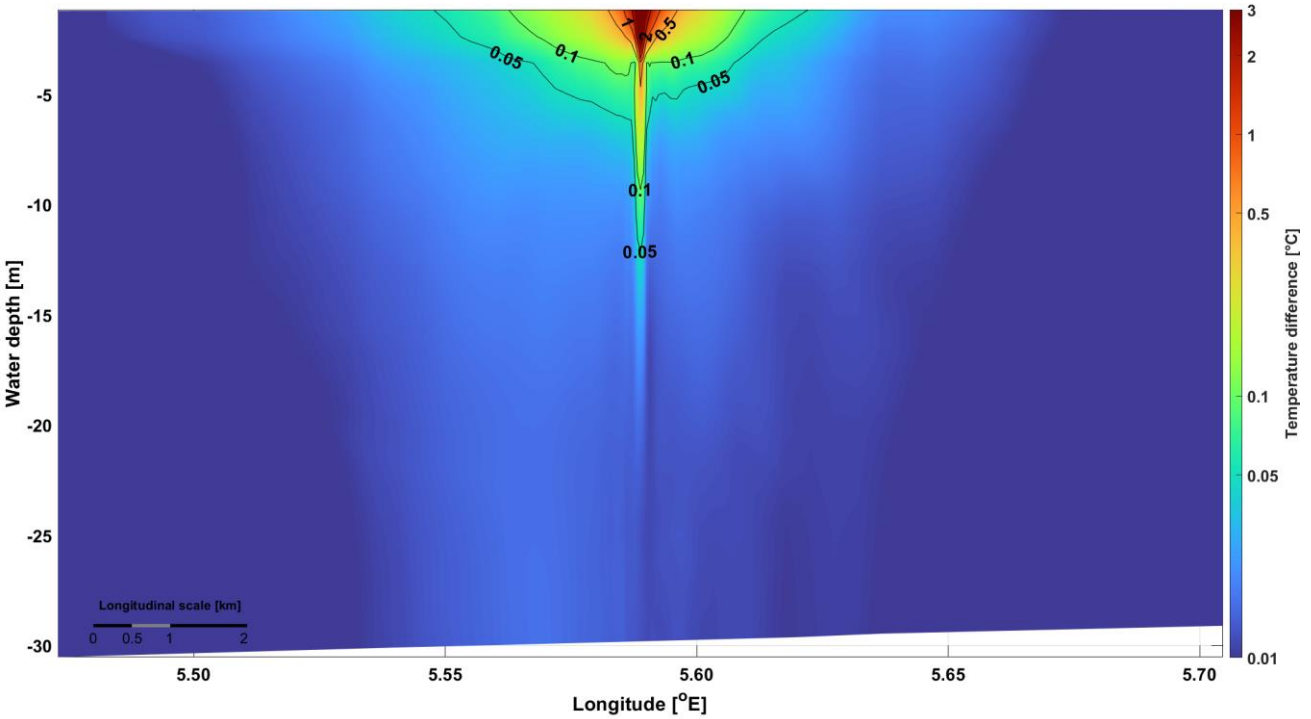

Figure 19. *Average cross-sectional temperature difference for a 5 GW electrolyser discharging coolant during the winter simulation.*

The results show that the average vertical distribution of the elevated temperature signal is limited, with only smaller temperature differences (< 0.5 ºC) reaching water depths greater than 5 meters in both summer and winter simulations. The highest temperature differences are found at the discharge point, which is also the location where all temperature anomalies reach the largest water depths. It is apparent that while the elevated temperature plume is, on average, more centralized in winter compared to summer, no difference is found with respect to the maximum depth of temperature change of any degree. However, the average depth of temperature changes is slightly greater during winter. For lower electrolyser capacities, the average dispersion pattern and its vertical extent is reduced (Appendix L to O).

Figures 20 and 21 display the average vertical distribution of salinity changes for both seasons within the same cross-section, representing the brine discharge from a 5 GW electrolyser.

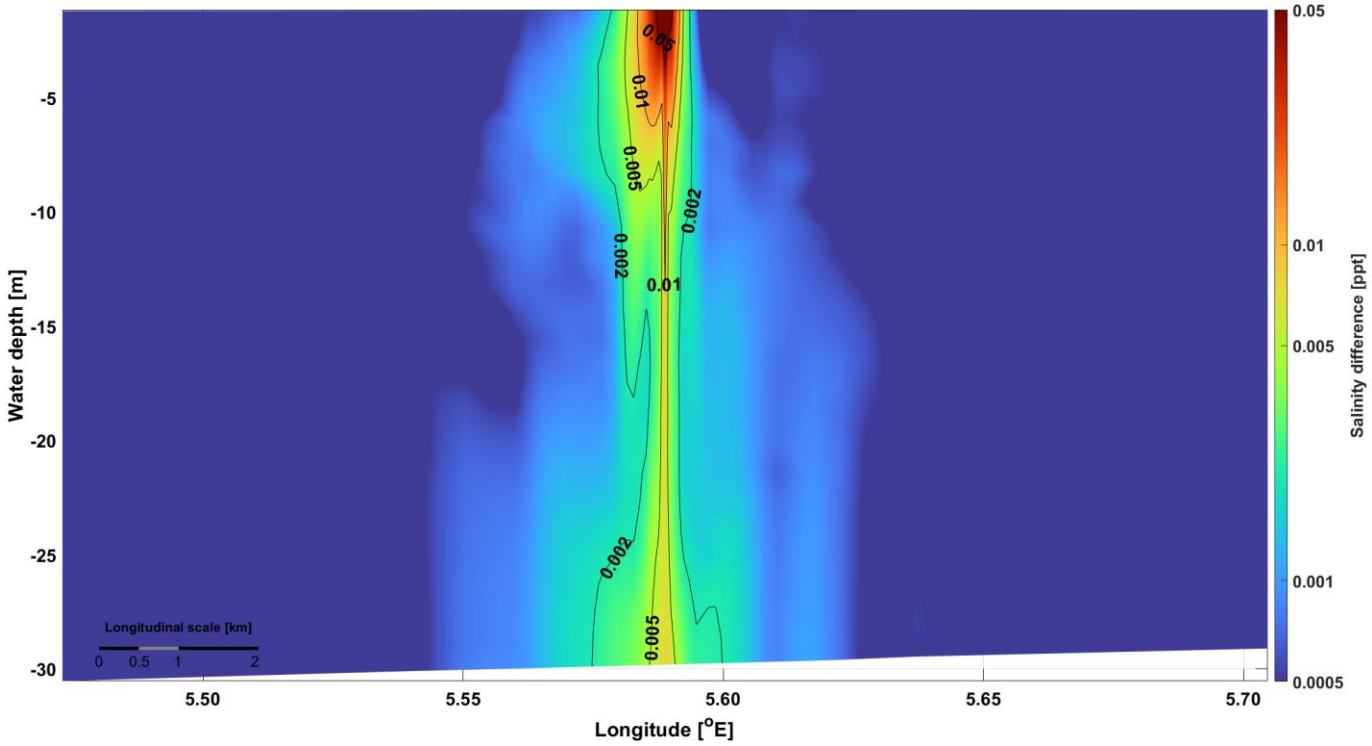

Figure 20. *Average cross-sectional salinity difference for a 5 GW electrolyser discharging brine during the summer simulation.*

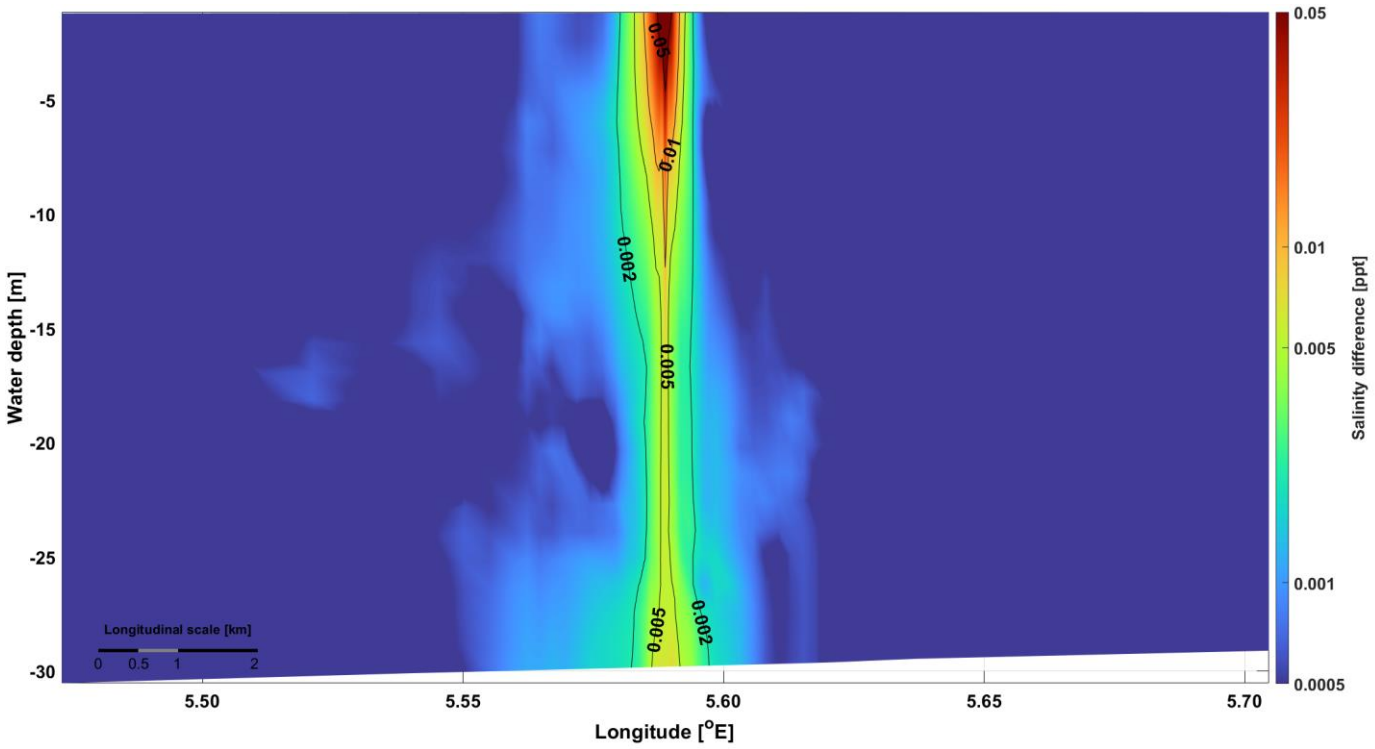

Figure 21. *Average cross-sectional salinity difference for a 5 GW electrolyser discharging brine during* the *winter* simulation.

Although the absolute increases in salinity are marginal, the vertical impact of the brine discharge is immediately apparent. For both seasons, salinity increases are observed at every water depth, with the highest changes occurring at and below the discharge point. As the plume descends, the salinity changes gradually decrease. Notably, significant salinity increases are found at the bottom of the water column. During the summer, there is a slight lateral spread of the bottom salinity anomaly, a pattern that is also observed in winter to a lesser extent. This is evidenced by the broader distribution of the lowest salinity increases in the lower half of the water column compared to the more concentrated surface anomalies. As evidenced in Appendix P to S, lower electrolyser capacities show the general distribution pattern. However, it is notable that for summer (1 GW), the vertical extent of the brine plume is significantly greater than that for winter (1 GW), with the brine reaching the bottom only in summer. This is however only true for the slightest salinity changes. For a 500 MW electrolyser, no salinity increases are found at the bottom of the water column, implying that the brine is fully dissipated before reaching the bottom.

The average cross-sectional thermal effects of a combined discharge scenario from a 5 GW electrolyser are displayed in Appendix T for summer and Appendix U for winter. No discernible difference in cross-sectional temperature difference was observed when compared to the results from coolant discharge alone.

Figures 22 and 23 display the average vertical distribution of salinity changes for both seasons within the same cross-section, representing the combined brine- and coolant discharge from a 5 GW electrolyser.

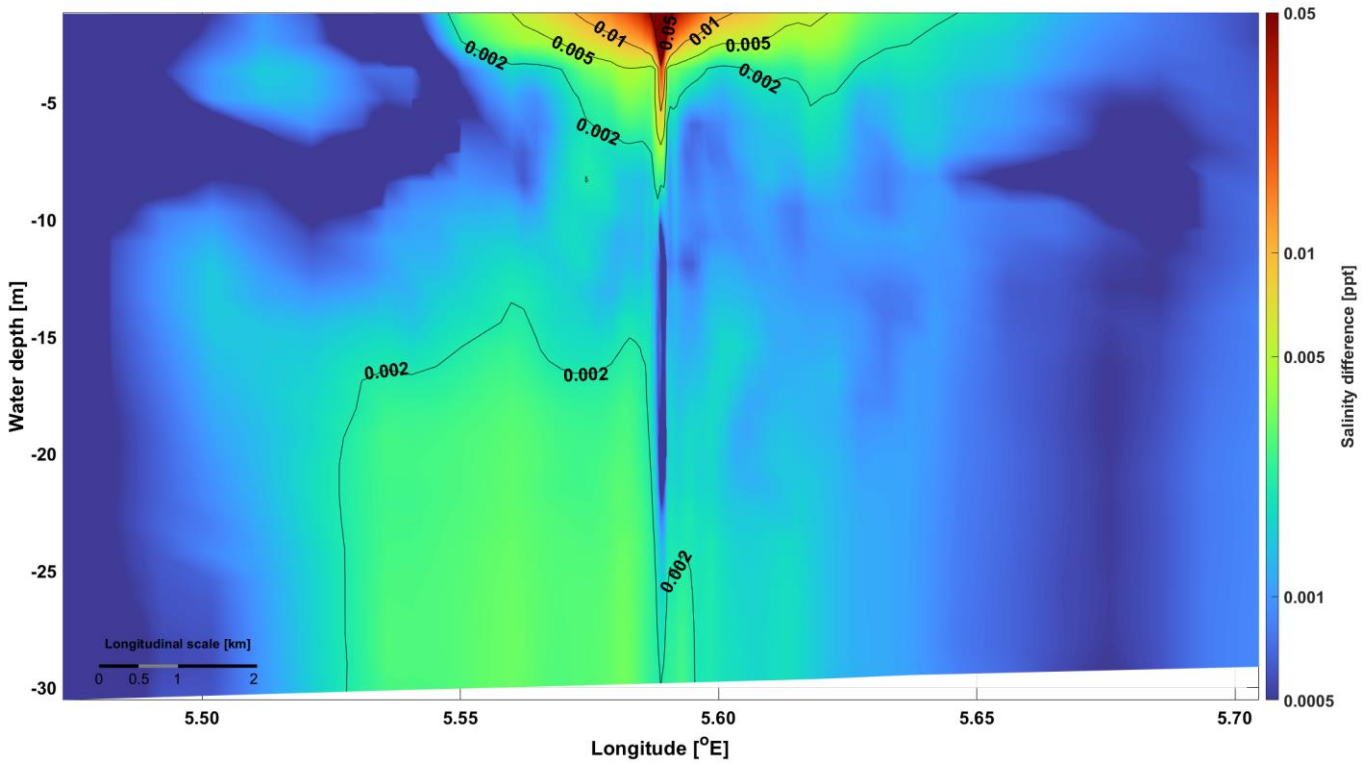

Figure 22. *Average cross-sectional salinity difference for a 5 GW electrolyser discharging brine and coolant simultaneously during* the *summer* simulation.

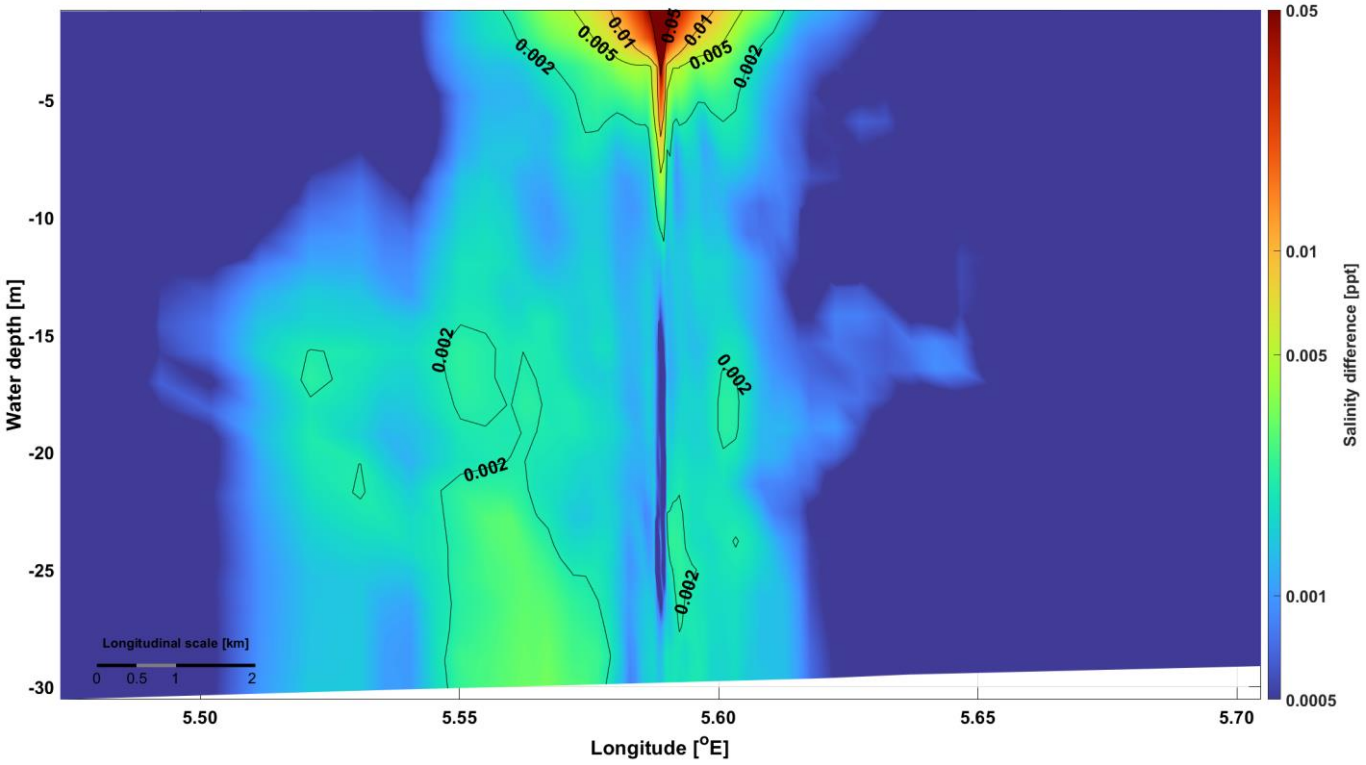

Figure 23. *Average cross-sectional salinity difference for a 5 GW electrolyser discharging brine and coolant simultaneously during* the *winter* simulation.

It is apparent from Figures 22 and 23 that the vertical distribution of salinity during combined discharges is substantially different from that of brine alone. Higher (>0.005 ppt) salinity increases are found more widely in the surface part of the water column but are on average not found deeper than 9 metres water depth, true for both summer and winter. The sinking pattern observed in Figures 20 and 21 are not found. The lowest salinity increases (≤ 0.002 ppt) are observed more widely spread throughout the water column, with summer showing the largest spread. In both seasons, a concentrated plume of moderate salinity increase (0.002 ppt) is found between 15 and 30 meters water depth directly west of the discharge position. In both seasons, patches of zero salinity increase are found within the affected area.

Averaged temperature and salinity change – bottom layer

Figures 24 and 25 show the change in salinity in the bottom layer for summer and winter respectively resulting from the brine discharge of a 5 GW electrolyser. A similar analysis was conducted for thermal effects from coolant discharge; however, no measurable change in temperature was observed in the bottom layer for either season for any simulation.

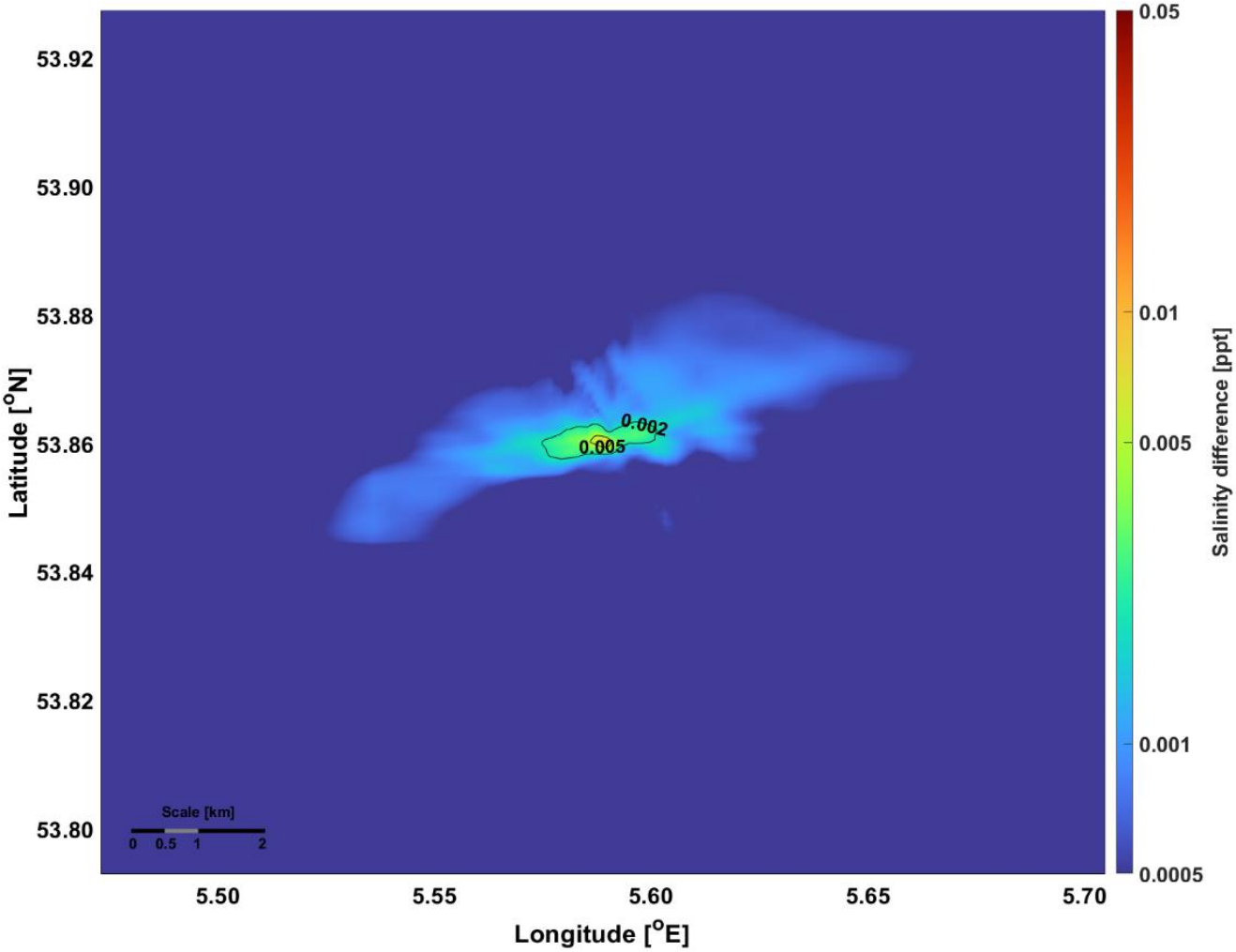

Figure 24. *Average bottom salinity difference for a 5 GW electrolyser discharging brine during the summer simulation.*

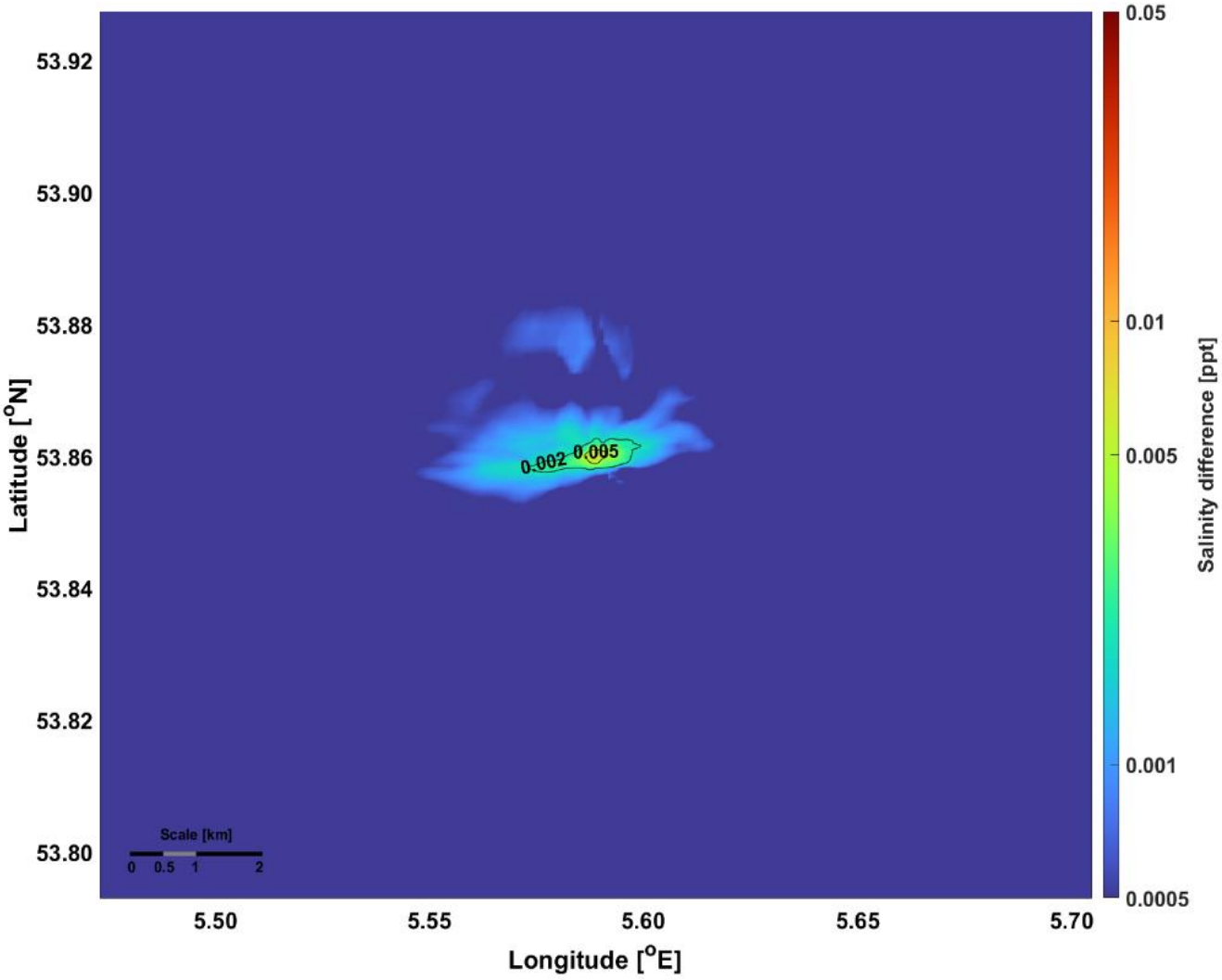

Figure 25. *Average bottom salinity difference for a 5 GW electrolyser discharging brine during the winter simulation.*

While the magnitude of the salinity increases in the bottom layer are slightly lower than in the surface layer (Figure 14 and 15) the lower salinity anomalies are comparable in size, implying lateral dispersion and dissipation of the brine plume at the sea bottom.

For a scenario discharging both coolant and brine simultaneously, the change in salinity in the bottom layer for summer and winter simulations are displayed in Figures 26 and 27 respectively.

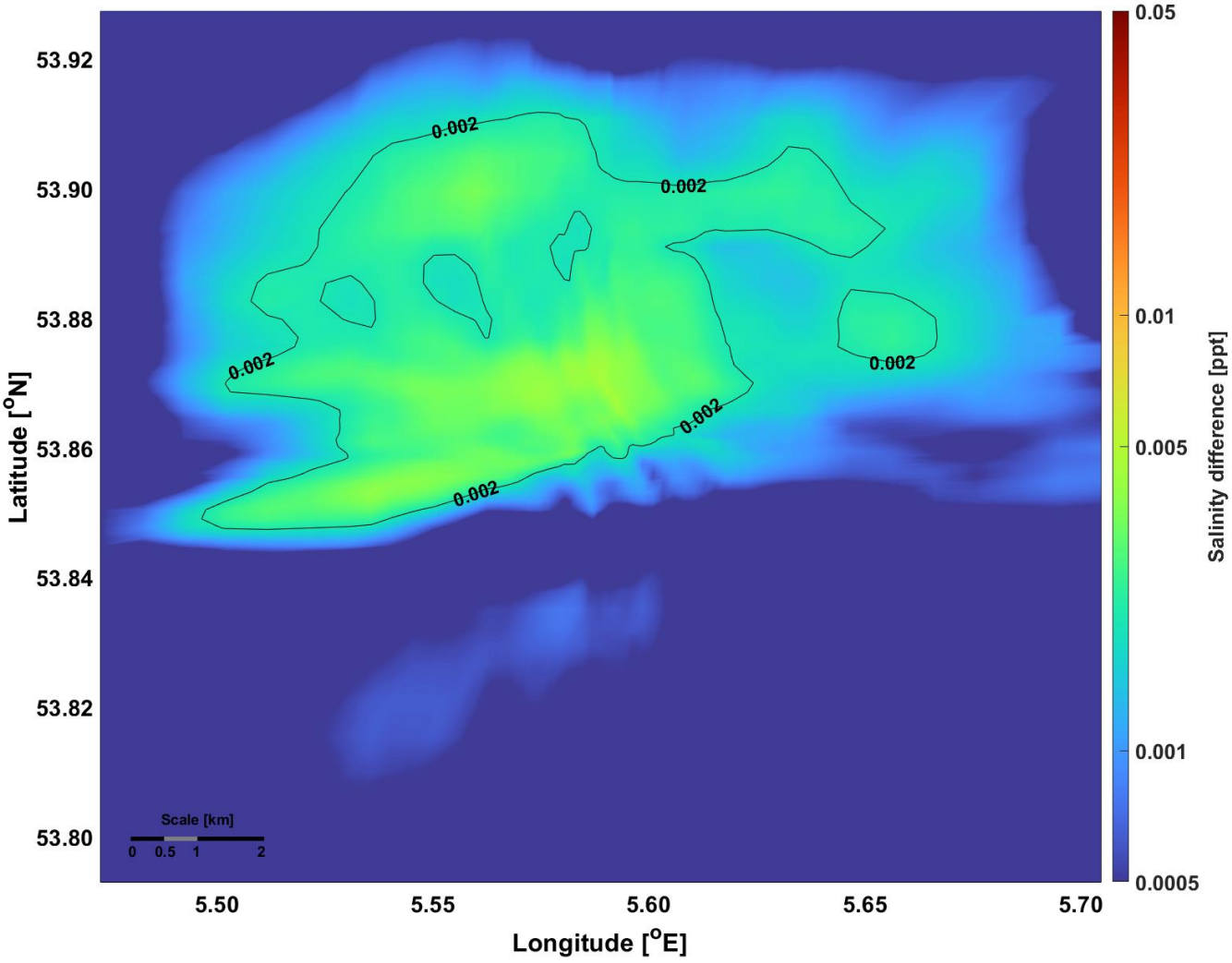

Figure 26. *Average bottom salinity difference for a 5 GW electrolyser discharging brine and coolant simultaneously during the summer simulation.*

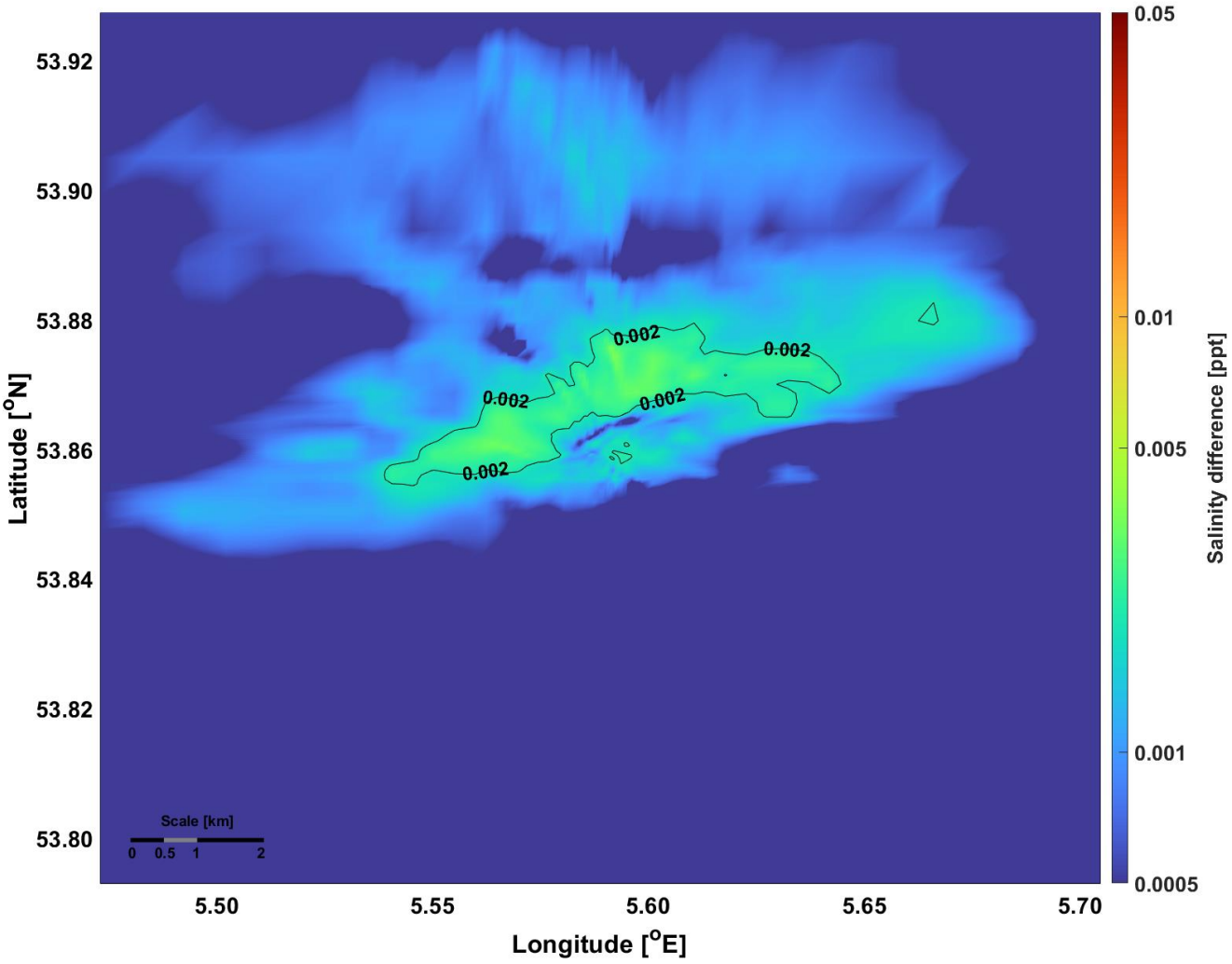

Figure 27. *Average bottom salinity difference for a 5 GW electrolyser discharging brine and coolant simultaneously during the winter simulation.*

The behaviour of the thermal plume in the surface waters of the domain resulting from a 5 GW electrolyser during winter during one characteristic tidal cycle is depicted in Figure 28. The sea surface level of the discharge point during the same tidal cycle is shown in Figure 29 (top), coupled with the surface current velocity in the X-direction at the point of discharge (Figure 29, bottom).

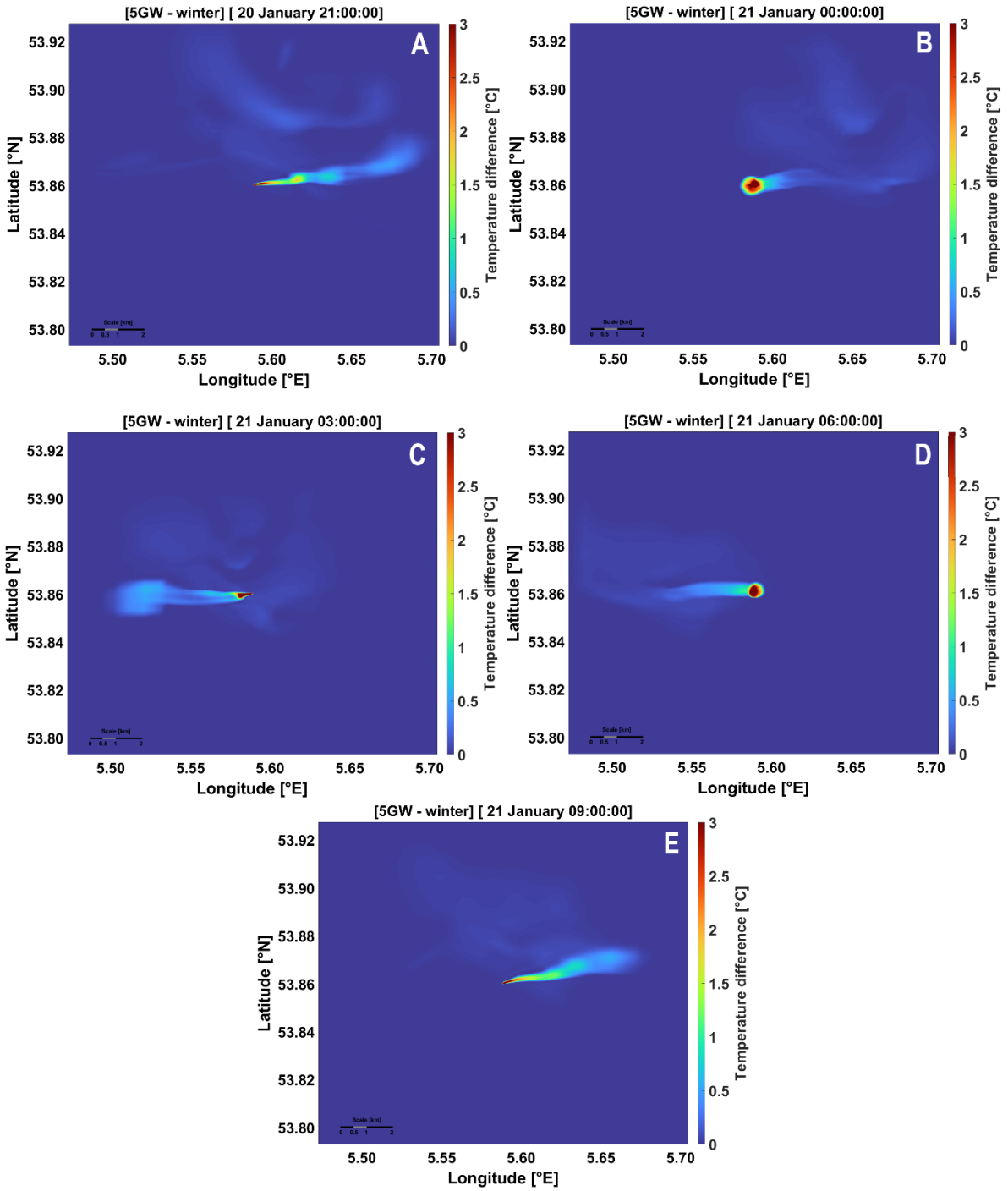

Figure 28. *Sea surface temperature difference for a 5 GW electrolyser discharging coolant during the winter simulation over one tidal cycle.*

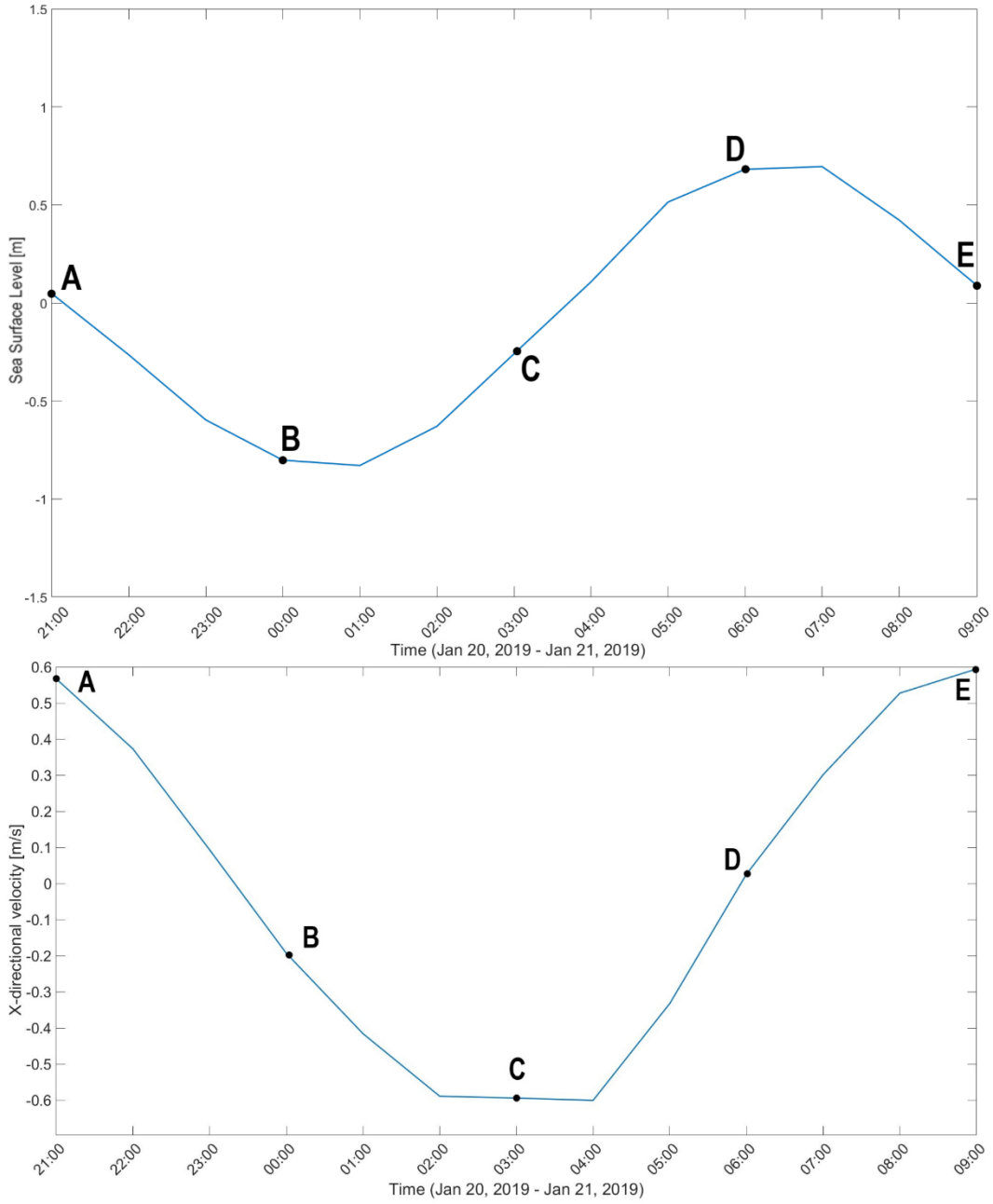

Figure 29. *Sea surface level per hour (top) and sea surface current velocity in the X-direction (bottom) for one tidal cycle (21:00 Jan 20th – 09:00 Jan 21st).*

In Figure 28-A, the thermal plume extends largely eastward, with temperature differences being relatively low (<1ºC) across most of the affected area. In point A, the surface current velocity in the X-direction are maximal (Figure 29). The highest temperature differences are observed in the surface waters directly adjacent to the discharge point. Three hours later, in Figure 28-B, the plume becomes centralized around the discharge point, with temperature elevations exceeding 3ºC. This point B coincides with relatively low surface current velocity. To the east of the discharge point, residual temperature elevations of 0.5ºC and lower are present, indicating some retention of the previous warming. In Figure 28-C, the plume extends west of the discharge point, with surface current velocities now maximal in the opposite direction. Similar to the pattern observed in Figure 28-A, temperature differences are relatively low (<1ºC) but affect a large surface area towards the west. Three hours later,

in Figure 28-D, the plume is centralized once again around the discharge point, with a trail of slight temperature elevations extending to the west. Again, current velocity is near 0 as displayed in Figure 29. In Figure 28-E, the plume extends back to the east. This extension shows high diffusion and dispersion, resulting in low temperature elevations over a broader area. The heat appears to diffuse quickly away from the discharge point, extending into the far field, similar to the situation depicted in Figure 28-A. Here, the current velocity is again maximal in the positive X-direction.

Figure 28 clearly illustrates the behaviour of the thermal plume in relation to the tidal cycle. During periods of significant sea surface level change, characterized by the steepest slope in the tidal cycle (Figure 29-A, 29-C and 29-E) and thus maximum surface current velocity, the thermal plume extends into the far-field, either westward or eastward. This extension of the plume structurally aligns with these high-change phases of the tidal cycle. Conversely, right before the tidal maximum of either the ebb or flood phase, the rate of sea surface level change is minimal (Figure 28-B and Figure 28-D), indicative of near stagnant water in terms of velocity (Figure 29). Here, the thermal plume shifts direction and becomes centralized around the discharge point.

For the same part of the tidal cycle, the cross-sectional temperature differences are displayed in Figure 30.

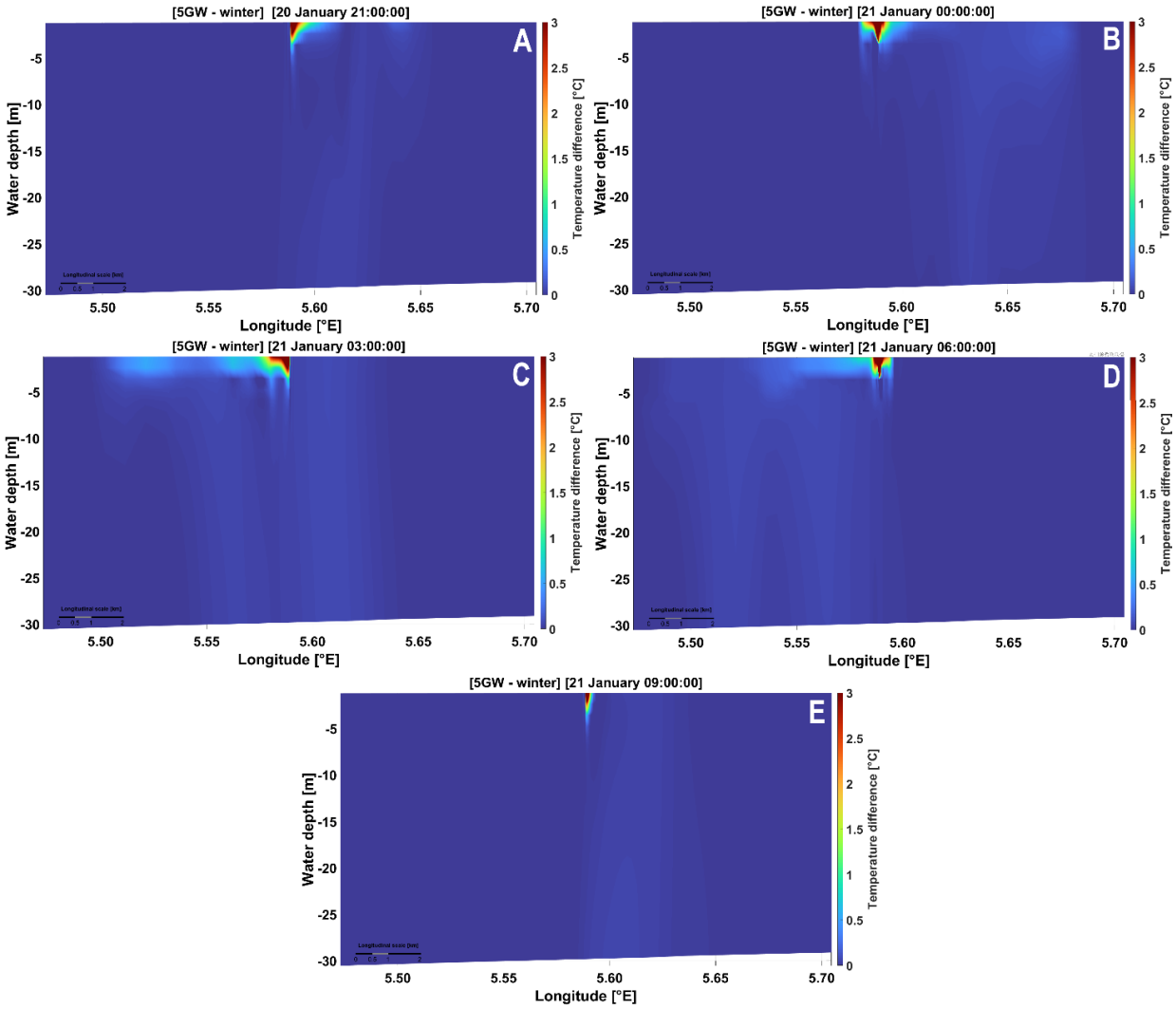

Figure 30. *Cross-sectional temperature difference for a 5 GW electrolyser discharging coolant during the winter simulation over one tidal cycle.*

A similar pattern to the surface layer is observed in the cross-sectional plot. The eastward dispersion seen in Figure 30-A appears to be confined to the top 5 meters of the water column. Directly below the discharge point, there is a downward spike in increased temperature. At this point, a steep temperature gradient is recorded, with temperatures over 3 degrees higher than ambient directly at the discharge point, rapidly dissipating in all directions. This pattern remains consistent throughout the tidal simulation. In Figure 30-B, the plume is centralized, again confined to the surface part of the water column. Figure 30-C shows a similar pattern to Figure 30-A but directed westwards. In Figure 30-D, the plume centralizes again. As shown in Figure 30-E, the central plume becomes asymmetrical, extending more towards the east. However, it is apparent that the eastward dispersion seen previously in surface waters is not visible within this cross section.

Plume dispersion during a tidal cycle – brine

The distribution of the brine plume in the surface waters of the domain, resulting from a 5 GW electrolyser during the winter, is depicted in Figure 31.

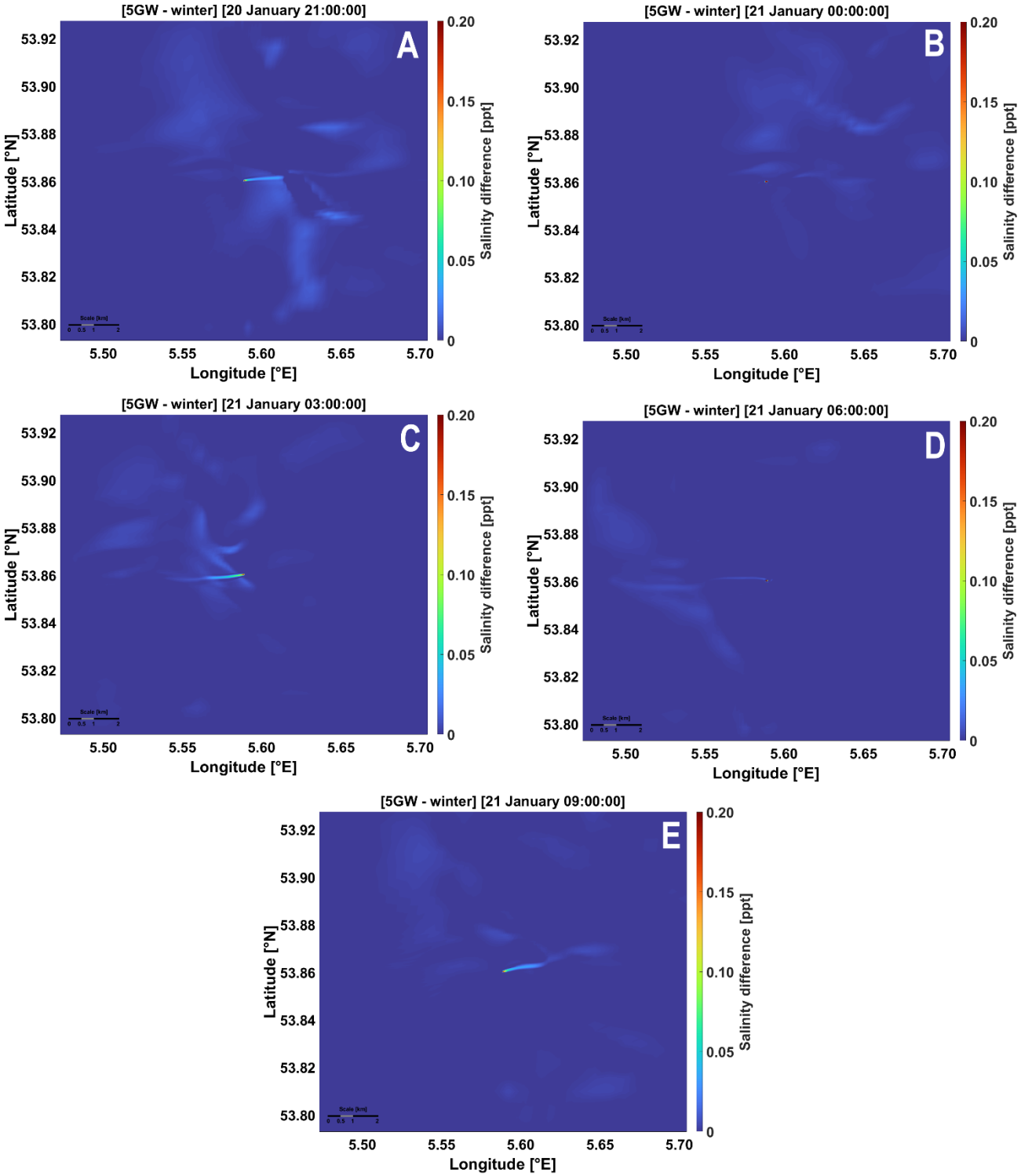

Figure 31. *Sea surface salinity difference for a 5 GW electrolyser discharging brine during the winter simulation over one tidal cycle.*

It is immediately apparent that the affected surface area due to the discharge of brine is very limited. The distribution pattern is similar to that of the surface dispersion of coolant, though to a much smaller degree. In Figures 31-A, 31-C, and 31-E, the plume extends laterally, but the salinity anomaly quickly decreases away from the discharge point to values lower than 0.05 ppt. In Figures 31-B and 31-D, no lateral transport is observed in the surface layer. The only salinity increases during these phases of the tidal cycle are found directly at the point of discharge.

Figure 32 shows the cross-sectional salinity difference for a 5 GW electrolyser during winter at various times during a tidal cycle.

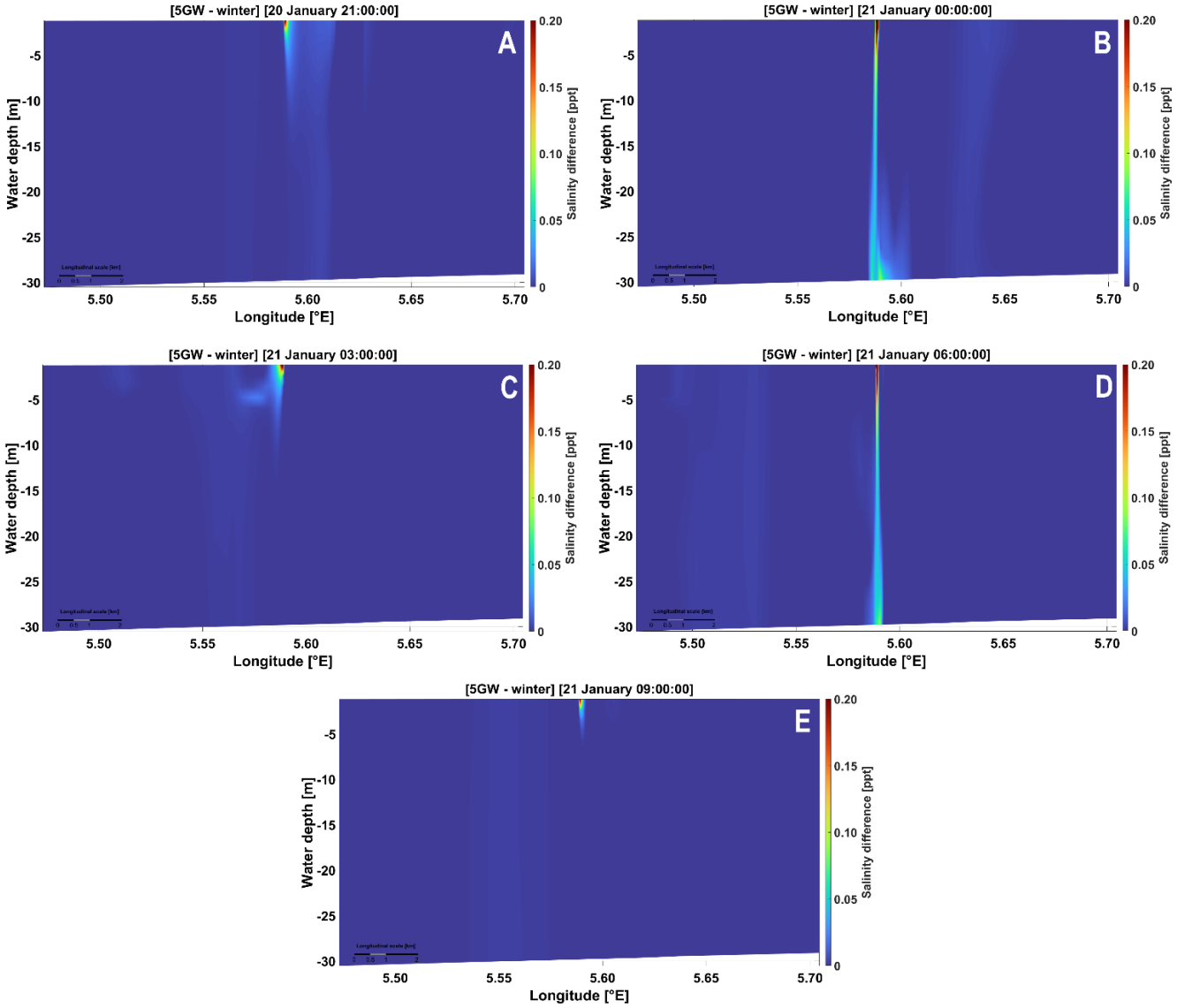

Figure 32. *Cross-sectional salinity difference for a 5 GW electrolyser discharging brine during the winter simulation over one tidal cycle.*

In Figure 32-A, the salinity plume is marginally extended downwards, primarily confined to the top 10 meters of the water column, with the highest salinity differences exceeding 0.20 ppt at the discharge point. No significant horizontal transport and diffusion is visible. By Figure 32-B, the plume is centralized around the discharge point and undergoes sinking, reaching the seabed. This process occurs right before slack waters during ebb (Figure 29-B). During sinking, the plume exhibits a sharp decreasing gradient of salinity increase from the surface towards the bottom, with the salinity anomaly at the seabed approximately 0.08 ppt. Directly westward of the sinking plume, slight salinity increases indicate lateral diffusion within the water column. Three hours later, in Figure 32-C, the downward diffusion of the salinity anomaly is limited vertically, with no significant horizontal diffusion. In the next phase, as seen in Figure 32-D, the brine plume fully sinks, reaching the seabed without visible lateral diffusion in the water column. Again, this sinking process coincides with the period right before slack waters found now during flood (Figure 29-D). In Figure 32-E, the plume's direction of diffusion and vertical extent is comparable to that of Figure 32-A.

Volume of seawater affected by a temperature and salinity increase

The volume of seawater affected by given increases in temperature and salinity for all scenarios, averaged over the 10-day simulation period, is displayed in Figure 33. The results were obtained by calculating the affected area within a contour of temperature or salinity elevation for each of the 25 layers. These findings were then multiplied by the layer thickness (approximately 1.19 meters) to determine the affected volume for each layer. The affected volumes for each layer were subsequently summed to determine the total volume affected by this change or higher for a given simulation.

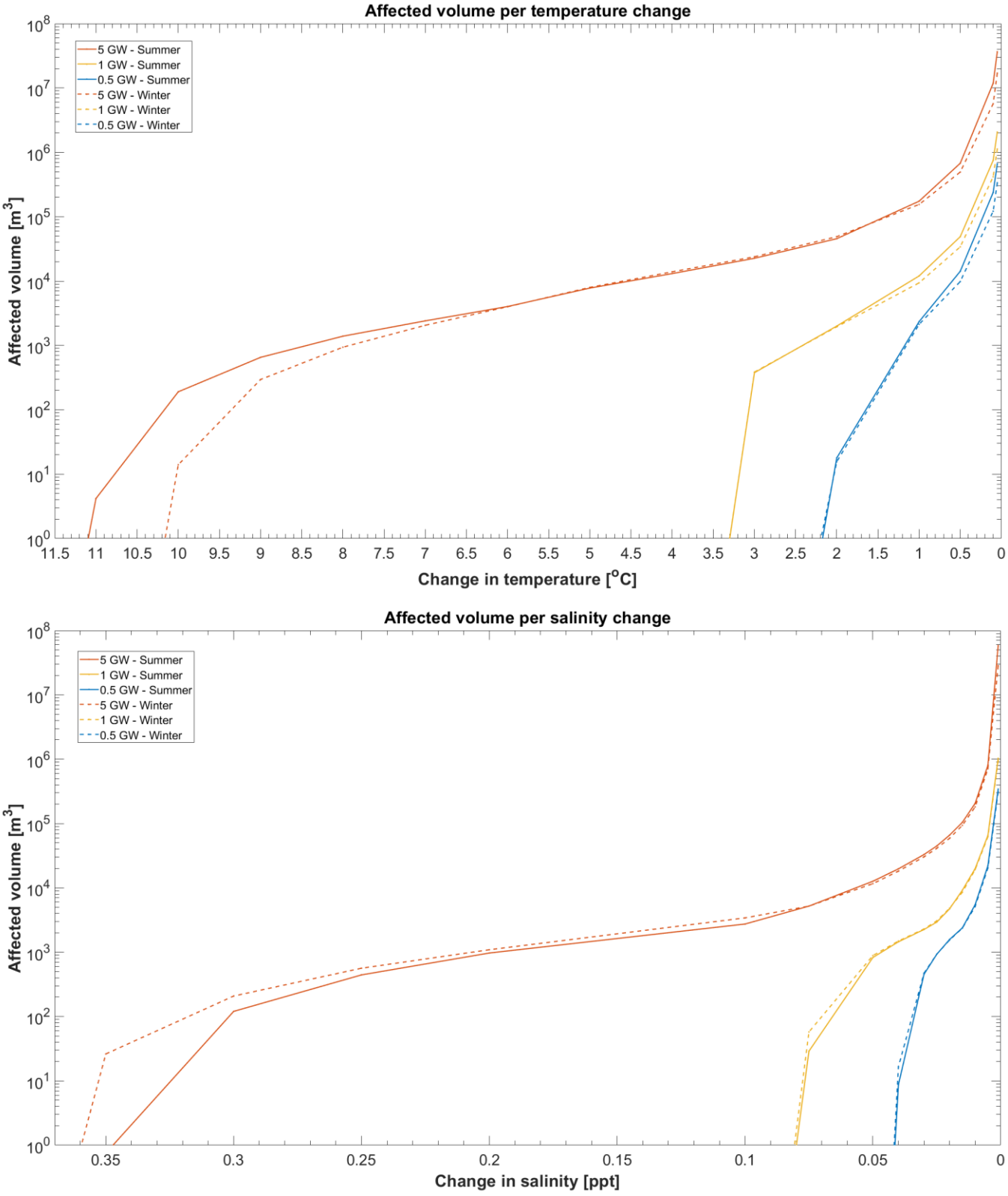

Figure 33. *The volume of seawater affected by change in temperature (top) and salinity (bottom) for all simulated scenarios.*

Note. The axes 'Change in temperature' and 'Change in salinity' are reversed, representing the gradient away from the discharge point from maximum values to minimum values.

Figure 33 portrays a clear inverse trend: lower total seawater volume is affected by higher differences in temperature and salinity. This finding is in line with previous findings, where the plumes spread and dilute whilst moving away from the discharge point. Interestingly, affected volume during winter is equal or lower to that during summer for all scenarios except the 5 GW coolant simulation. In this simulation, the thermal effluent appears to affect a larger part of the water column on average between 1.6 and 6.4 ºC during winter. Within this interval, the affected volume during the winter simulation is on average 6.8% larger compared to that during summer, with the largest difference found at the 3 ºC contour, where the difference is 8.6%. However, when taking the difference between summer and winter affected volumes, it can be concluded that during summer, the affected volume of thermal effluent is on average 17.7% lower during winter. For the brine effluent, the affected volume is on average 11.3% lower during winter. It is important to note that the average difference between seasons was consistently found within the lowest contour values, which coincides with the region prone to the largest degree of uncertainty.

4. Discussion

The influence of the tidal cycle on the dispersion pattern of wastewater plumes

The results presented in this study reveal a distinct cyclic behaviour of both thermal and brine plumes, which adhere to the tidal cycle. As expected, the results from coolant discharge show that the thermal plume is largely confined to the top 5 meters of the water column, likely due to its lower density compared to ambient waters. The extent of the thermal plume is consistently largest immediately after the maximum current velocity during falling ebb or rising flood, a finding consistent with recent studies (Kong & Guan, 2024). During this phase, diffusion and dispersion are both high, induced by increased momentum and mixing in the water column. Additionally, water heated by the plume is advected into the far field, contributing to the dispersion of heat.

Directly before low- and high tides, when current velocities are small, the plume becomes more centralized around the discharge point. Here, dispersion of the plume remains very low: heated water is not advected laterally; instead, transport of heat occurs primarily through diffusion, as evidenced by the low current velocity. Thereafter, as the momentum and velocity of the currents increase, dispersion of the plume also increases, but in the opposite direction as the flood rises or ebb falls. This pattern of a concentrated plume around tidal maxima and far-field dispersion during the rise and fall of ebb-flood is consistently observed across both modelled periods. Furthermore, this finding aligns with recent studies observing thermal plumes in areas influenced by tides (Faulkner et al., 2021; Kong & Guan, 2024).

The brine plume exhibits similar behaviour in the surface layer, though the affected surface area of the plume is much more limited. Notably, while coolant simulations show a concentration of heated water around the discharge point during tidal maxima, the brine influence is characterized by increased salinity directly at the discharge point (Figure 31-B & 31-D). This is explained by the heightened sinking of brine during these phases. Brine, being denser than surrounding waters, sinks more rapidly, especially during tidal maxima. However, it is only during these tidal maxima where current velocities are minimal that the brine reaches the seabed. The salinity anomaly decreases in magnitude at the seabed compared to surface waters, indicating some dilution during its descent. As illustrated in Figure 32-B, upon reaching the seabed, the brine plume is advected laterally and eventually dilutes. Thus, a bottom layer with heightened salinity does not form, though the seabed experiences periodic increases in salinity.

The influence of seasonality on the dispersion pattern of wastewater plumes

Seasonal differences in the affected volume have been identified for both brine and coolant scenarios. For coolant discharge, the affected volume is consistently lower during winter across all scenarios, applicable to both smaller temperature changes (in the far-field) and larger temperature changes (near the discharge point). Given that the dispersion of the thermal plume is mainly confined to the surface, seasonal differences in wind velocities and directions likely play an important role. Indeed, wind data over the domain show that wind speeds are substantially lower during summer, predominantly from the southeast (see Figure 8). Moreover, the interannual wind data (Appendix A) confirm that the prevailing winds during the 10-day simulation periods are generally characteristic of the governing wind patterns in the TNW area: summer months are generally characterized by slower wind speeds that are quite consistently (north)eastwards, whereas winter months are more variable in direction and show greater wind velocity on average.

Wind direction and strength are recurrent factors influencing thermal plume behaviour. Kong & Guan (2024) emphasized that calmer winds weakened surface flow fields, leading to expanded diffusion of heated water. Additionally, shifts in wind direction altered the flow direction and diffusion pattern of the thermal plume. A modelling study on the seasonal changes in atmosphere-ocean heat exchange in the North Sea found a linear relationship between increased ocean-to-atmosphere heat fluxes and high wind speeds (Schrum & Backhaus, 1999). However, the study implemented a local coupled ice-ocean model which is not suitable for assessing atmosphere-ocean heat exchange for longer timescales (i.e. interannual variability). Still, these findings do align with the results of this study, namely the observed lower surface temperature differences during winter when wind velocity is high. Conversely, Faulkner et al. (2021) found that different prevailing wind conditions during winter and summer did not significantly alter the overall dispersion pattern of thermal plumes on the west coast of the United Kingdom, underscoring the dominance of ambient current velocity and direction over seasonal wind variation. In modelling study scenarios where the tidal constituent was not considered, lower wind speeds resulted in a limited spread of the plume with higher heat concentrations near the source (Gaeta et al., 2020; Aljohani et al., 2022). The results of this study likely reflect the dominance of tidal constituents in governing the dispersion of the thermal plume. However, as warmer waters are advected, calmer prevailing wind conditions may hinder heat dissipation to some extent, due to less wind-induced surface shear, which hinders mixing in the surface water column and decreases latent and sensible heat fluxes towards the atmosphere (Laguna-Zarate et al., 2021).

In brine scenarios, the difference in affected volume between summer and winter exhibits a consistent pattern. Across all capacities, winter simulations indicate a slightly larger affected volume near the discharge point for higher salinity changes. However, the most significant difference in absolute volume occurs with lower salinity changes, where summer scenarios consistently show an increase in affected volume. Additionally, during summer, the area affected by salinity changes in the bottom layer is notably larger compared to winter simulations. This phenomenon may be attributed to lower wind velocity during summer, which reduces surface wind shear. Consequently, the low-energy conditions during tide overturning are slightly extended in summer. Notably, the recorded sinking of brine occurs only during periods of the lowest current speeds, and reduced surface winds might marginally extend this period, allowing for a slight increase in vertical transport of brine. However, surface dispersion patterns of brine show very limited distribution southwards, despite predominantly southward wind speeds, especially in summer. This suggests that surface wind shear does not profoundly affect the brine plume’s dispersion. Additionally, while the pattern of increased affected volume for lower salinity increases is consistent across multiple scenarios, such small values fall beyond the model's confidence interval. Studies on marine brine distribution highlight seasonal stratification's effects on brine dispersal. For instance, in thermally stratified waters, descending brine entrains warmer waters, reducing its density and propagating at shallower depths than in winter (Wood et al., 2020). Fernández Torquemada et al. (2009) found that stratified waters hinder brine from reaching the seabed due to higher bottom water density, causing stagnation at 12-15 meters depth. While the TNW area can experience intermittent stratification with interannual variability (van Leeuwen et al., 2015), no stratification was identified during both simulation periods (Figure 10 and Figure 11).

The effects of simultaneous discharge

When comparing the distribution of temperature in the surface part of the domain, as well as the vertical extent resulting from a 5 GW electrolyser discharging coolant alone versus discharging both coolant and brine simultaneously, no noticeable difference is found. Conversely, the distribution of salinity is substantially altered when brine is released together with coolant. The periodic sinking of brine during high and low tides is not observed in the combined discharge scenarios. The moderately saline parts of the brine plume reach similar depths (up to roughly 10 meters) as the thermal plume. This observation indicates that the brine outflow mixes significantly with the thermal plume, resulting in a combined density lower than that of the surrounding waters. Consequently, this prevents sinking even when current velocities are minimal. While the mixing of both wastewater discharges largely eliminates the higher salinity anomalies found at the bottom, the surface dispersion of increased salinity is significantly greater than that of a singular brine discharge. This is likely due to the increased lateral advection from the higher discharge rate of the thermal wastewater stream. In fact, modelling studies investigating the discharge of wastewater in the Sea of Japan (Morelissen et al., 2016) and the Eastern Mediterranean (Wood et al., 2020) recorded reduced salinity anomalies in the far-field and partly compensated negative buoyancy of the plume when brine mixed with thermal discharge, resulting in heightened surface propagation of the brine.

Throughout the water column, patches of moderate to low (≤ 0.002 ppt) salinity increases are found, implying that sinking of more diluted brine does occur. It should be noted that when observing the dispersion of salinity for a combined scenario at individual timeframes, negative salinity anomalies up to -0.004 ppt are sporadically found within the water column. This could result from very slight differences between the salinity of the coolant stream, which is specified on an hourly scale, and the salinity of the reference run, which is calculated every 18 simulated seconds. Additionally, because the volumetric flow rate of coolant is more than 55 times higher than the brine discharge, local hydrodynamic flow patterns may be altered. Consequently, subtracting the reference scenario from the combined discharge scenario may occasionally involve comparing two water bodies that do not necessarily correspond to one another, resulting in false salinity changes not directly attributable to brine discharge. This effect was not significant for the individual coolant scenario, as the magnitude of temperature differences investigated were not as low as salinity differences found in the brine scenarios. Moreover, due to the relatively low volumetric flow rate of brine, the simulation scenarios involving only brine were likely less prone to such measurement inaccuracies.

Applicability to other study areas

In the context of thermal effluent, existing literature primarily investigates coastal discharge (Laguna-Zarate et al., 2021; Aljohani et al., 2018; Gaeta et al., 2020; Deabes, 2020). A notable distinction between coastal studies and this study lies in the sharpness of the temperature gradient directly away from the discharge point. For instance, Laguna-Zarate et al. (2021) found that during simulations comparable to the 5 GW scenario in this study, the water temperature remains, on average, 2 ºC higher than ambient 1 km seaward of the discharge point in both summer and winter. In contrast, our 5 GW scenarios reveal temperature elevations of approximately 0.5 ºC, limited to the east and west of the discharge point. Similarly, Aljohani et al. (2022) found that offshore discharge (1.5 km seaward) resulted in a sharper initial gradient in excess temperature compared to nearshore results, indicating quicker dissipation of thermal effluent. Interestingly, the total extent of the thermal plume was larger, with small temperature anomalies (<0.2 ºC) extending further along the coast compared to coastal discharge. This discrepancy is likely due to the large difference in

water depth. In shallow environments, thermal effluent quickly heats the entire water column below the discharge point (Gaeta, 2020). This may result in heightened heating of waters surrounding the discharge point compared to deeper areas, where thermal dissipation is also possible vertically, transferring heat to colder underlying waters. The results of this study combined with literature findings on thermal discharge in coastal environments strongly indicate that a decrease in water depth has a detrimental effect on the dissipation of heat, both in the vertical and at the surface. As a result, locations like the TNW area, which are positioned further offshore, are likely better suited for mitigating harmful effects arising from thermal discharge.

The results presented in this study also underscore the direct relation, and thus the importance, of the strength of the tidal constituent within the area of discharge and the extent of both thermal and brine plumes. Tide induced currents increase dilution of both brine and coolant but increase their range of dispersion. In areas with weaker tides, local concentration of salinity and heat might be significantly increased while the spatial extent of the plume may be reduced, as evidenced by the behaviour of the plumes during high- and low tides where current velocity is minimal. Furthermore, a complete surface to bottom traversal of brine was shown to be only possible during high- and low tides, a period that might be extended in areas of weak tides. However, the simultaneous discharge of coolant and brine proved to be effective in inhibiting sinking of brine. Lastly, in areas with weaker tides, the oscillatory surface motion of the plumes may be reduced or not occur altogether. This may inhibit the alleviation of longer lasting heating or increases in salinity.

Ecological implications of brine discharge

The results of this study indicate that the increase in salinity due to brine discharge from hydrogen electrolysis, even in the worst-case scenario with a 5 GW electrolyser operating at 100% capacity, never exceeds the natural salinity variations found in the North Sea as evidenced in Table 6. The maximum observed salinity increase directly at the discharge point was approximately 0.05 ppt, a value that quickly diminishes with distance from the source. This increase is significantly below the salinity changes cited in the literature as stressful for marine organisms, including phytoplankton, seagrasses, and various marine fauna (Table 2). For lower electrolyser capacities, the salinity differences are nearly undetectable, reinforcing the conclusion that direct salinity stress on marine life is highly unlikely under typical operating conditions. However, recent studies on brine discharge argue that while slight salinity increases may not cause direct harm, dynamic effects could still be significant (Biton et al., 2008).

Recent coastal studies on brine discharge have highlighted several dynamic effects that could arise from the formation of density currents. These studies suggest that gravity currents and the Coriolis force can cause dense brine plumes to spread along the seabed, even when density differences between the diluted brine and ambient seawater are relatively small (Biton et al., 2008). For instance, modelling studies on the Eastern Mediterranean coast have shown that far-field propagation of desalination brines can form a higher density layer above the seabed, impeding the vertical mass transfer of nutrients from the seabed to the overlying water (Kress et al., 2020; Wood et al., 2020). This process is critical as the recycling of organic matter and remineralization of nutrients in coastal-shelf sediments support up to 40% of primary production in coastal waters. In our study, we observed the occurrence of lateral dispersion of denser brines. These brines, with salinity increases around 0.05 to 0.02 ppt above ambient levels, align with the findings from density current studies (Wood et al., 2020). However, no lasting salinity anomalies at the seabed were found in the present study, as the anomalies were diluted within one tidal cycle. It is clear that direct effects of increased salinity as a result of brine discharge in the TNW area are likely

not ecologically significant, given they were found to be short-lasting and extremely slight in magnitude. However, further research into the transient effects of brine discharge on nutrient cycling and marine productivity is needed given the low salinity change required (Wood et al., 2020).

Another dynamic effect observed in this study is the influence of tidal currents on the sinking behaviour of the brine plume. During low- and high tide, the brine sinks relatively quickly, reaching the seabed within approximately 12 minutes for a 5 GW discharge. This rapid sinking could potentially affect the surface-to-bottom transport of nutrients, oxygen, and other properties, altering the ecological balance in the affected area. This effect, while transient, could still influence primary productivity, especially if such occurrences coincide with critical periods of phytoplankton growth or other biological processes. However, given the small spatial footprint of the brine plume at depth, these effects would likely be very local. Crucially, when brine is discharged together with coolant, sinking of the brine towards the bottom layer is completely inhibited. This will in all likelihood negate any dynamic effects potentially coupled with rapid sinking events. Furthermore, while the recorded salinity increases are much more widespread in the surface layers, the magnitude of such increases fall far below the natural variation of salinity in the area. In all likelihood, when brine is discharged alongside thermal effluent, direct and indirect harmful ecological effects of increased salinity in the TNW area will be extremely limited even for a worst-case scenario of a 5 GW electrolyser.

Ecological implications of thermal discharge

The temperature differences up to several degrees Celsius observed in this study, particularly for the worst-case scenarios of a 5 GW electrolyser, may be sufficient to cause ecological damage in the direct vicinity of the discharge point, especially to planktonic fauna such as phytoplankton and fish. As multiple studies on thermal effluent have highlighted, phytoplankton communities have been shown to shift in community and abundance during warming events of even a few degrees Celsius (Hu et al., 2023; Zhang et al., 2023; Li et al., 2011). Furthermore, physiological stress responses in both tropical and temperate fish have been identified for the same temperature increases (Johansen et al., 2021; Shiomoto & Olsen, 1978). Other responses could include reduced swimming speeds, loss of balance and orientation, and altered reproductive processes. Fish mobility might help some individuals avoid the most thermally stressful areas, but this avoidance behaviour could lead to habitat compression and increased competition for resources elsewhere (Birtwell et al., 2003). However, given the relatively limited spatial footprint of significant temperature increases (i.e., >1ºC), such an effect is likely not substantial in the TNW area. Effects on benthic fauna and reproductive processes (i.e., egg development and hatching) are likely to be limited as the thermal plume never significantly altered water temperatures at the seabed for any simulation. Furthermore, seeing that for all scenarios the thermal plume remains within this study's domain, no areas of environmental protection are influenced by the discharge of wastewater in the TNW area.

It is important to note that while temperature elevations of 1°C or higher, potentially indicative of inducing ecological harm, may extend multiple kilometres away from the discharge point for the 5 GW scenarios, such heating of the surface of the water column is subject to high variability. Fluctuating temperatures driven by the tidal cycle result in oscillating thermal gradients that can differ substantially from the constant thermal conditions often studied in laboratory settings. These rapid temperature shifts can lead to both alleviation and exacerbation of thermal stress, depending on the resilience of the affected organisms (Cabrerizo & Marañón, 2021). For instance, species naturally exposed to variable temperatures, tend to be more thermally resilient and capable of adapting to rapid changes,

often found in coastal zones such as estuaries (Cabrerizo et al., 2021). However, for species not accustomed to such variability, such as found in open seas, rapidly fluctuating temperatures can exacerbate thermal stress, potentially leading to reduced growth, altered reproductive success, and disrupted community interactions (Kremer et al., 2018). Furthermore, thermal variability has been shown to disrupt species coexistence among phytoplankton. Fluctuating temperatures can provide a temporary refuge for less competitive species, but extreme thermal fluctuations can accelerate species displacement and lead to unpredictable changes in community composition (Siegel et al., 2023).

Direct harmful effects of the presented temperature elevations appear to be either confined to the worst-case simulations in the far field or confined to the direct proximity of the discharge point for lower electrolyser capacities. However, it is important to consider the potentially exacerbating effects of multiple ecological stressors. Cooling systems used in industrial processes pose a significant threat to marine fauna through mechanical and chemical stressors. The substantial intake volumes required for cooling systems can entrain planktonic organisms and small fish, subjecting them to mechanical stress from turbulence, pressure changes, and collisions with intake structures (Lee et al., 2018). Once inside the cooling system, these entrained organisms are exposed to elevated temperatures, exacerbating the stress and potentially leading to thermal shock. The use of anti-biofouling agents in cooling systems introduces an additional layer of chemical stress. These agents, such as chlorine, are toxic to a wide range of marine organisms, causing oxidative stress, respiratory distress, and increased mortality rates (Amara et al., 2018). The combination of mechanical, thermal, and chemical stressors can produce synergistic effects, where the presence of one stressor amplifies the impact of the others. This can lead to unexpectedly severe outcomes, such as sudden population crashes or shifts in community structure, which are not anticipated based on the impacts of each stressor in isolation (Dafforn et al., 2011).

In situ studies aiming to assess the impact of thermal discharge from cooling systems face significant challenges in isolating the effects of thermal stress from those of chemical stressors. The simultaneous presence of anti-biofouling agents complicates the interpretation of observed ecological impacts. For example, reductions in phytoplankton abundance or changes in species composition could be attributed to thermal stress, chemical toxicity, or a combination of both. Similarly, fish mortality observed near discharge points might result from elevated temperatures, exposure to toxic chemicals, or the cumulative impact of both stressors (Crain et al., 2008).

Limitations of used methods

The methodology used in this research proved to be effective in capturing the three-dimensional behaviour of hypersaline- and thermal effluent within the research area. However, it is important to assess some limitations of the used methods which may have altered the results to a degree.

Firstly, while the use of a variable grid resolution is an efficient strategy to balance simulation accuracy with data, computational power, and computation duration requirements, this may induce an incorrect representation of diffusion of the plume. The grid resolution is coarsening outwards from the discharge point, which coincides with the outward spreading of the plume. In the far-field, numerical diffusion may be induced due to the transition of grid cells of higher resolution towards grid cells of lower resolution. Here, the transition to a coarser grid cell can lead to smeared gradients of the concentration and velocity variables, potentially overestimating the plumes' area while underestimating local concentrations.

Secondly, the input parameters handled in this study reflect a worst-case scenario that do not necessarily realistically reflect an offshore electrolyser system. For instance, the discharge parameters are calculated from a PEM electrolyser running at a constant 100% load. When translating the obtained results to a real-world scenario, it is important to note that this assumption is highly unrealistic. In all proposed offshore hydrogen concepts, the electrolyser is dedicated to power output from offshore windfarms (Leahy et al., 2021; Egeland-Eriksen et al., 2023; Hofrichter et al., 2023). Such a power supply is subject to the local wind velocity and direction, meaning that a power load sufficient to run the electrolyser at its full capacity is not always possible. This implies that the volumetric flowrate of brine and coolant will also be variable, as the power usage of the electrolyser corresponds to its hydrogen production and thus brine- and coolant discharge. The dispersion pattern of a temporally variable brine or coolant plume may be substantially different as evidenced by the results for lower electrolyser capacity. Additionally, selectively discharging brine during phases of rising flood or falling ebb may impede sinking processes, reducing the affected volume of salinity change. Alternatively, coolant could only be discharged during tidal maxima, reducing the spread of the thermal plume in the far-field.

It is important to note that the intake of seawater by the cooling stack, proportional to the volumetric flowrate of coolant outflow, was not considered within the confines of this study. This is an important topic to incorporate for future research, as this aspect may significantly influence the hydrodynamic processes observed. These differences may include local recirculation zone and possible mitigation of thermal effects by drawing cooler water from the far-field.

On the need for further research

Apart from incorporating variable discharges and the intake of the cooling stack, the following topics for further research can be formulated:

- What is the effect of seasonal phenomena such as stratification of the water column and the occurrence of storms on the distribution pattern of electrolyser wastewater discharge? The observed differences in affected volume for both coolant and brine between different seasons could not be explained fully within the confines of this study.
- What is the influence of offshore windfarms on the distribution patterns of electrolyser wastewater discharge? Offshore electrolyser systems will likely be coupled to one or more wind turbines placed offshore in the future (Hofrichter et al., 2023). It has been shown that the presence of wind farms in an offshore setting can impact sea surface winds, local flow patterns, length and strength of stratification and the distribution of temperature and salinity (Christiansen et al., 2022), all of which potentially alter the dispersion and behaviour of wastewater plumes.
- How does the dispersion pattern of wastewater discharged over multiple outfalls contrast with that from a single discharge point? While wastewater effluent discharged over multiple outfalls has been demonstrated to occasionally increase its thermal footprint (Morelissen et al., 2016), it may also aid in mitigating sharp gradients in temperature and salinity therefore reducing its ecological impact.
- What are the effects of discharge of anti-fouling agents as a result of offshore electrolysis? It is crucial to gain further understanding in the impact of antifouling agents in this research area, especially the potentially stacking harmful effects of thermal stress, salinity stress and chemical stress (Dafforn et al., 2011).

Lastly, it is important to highlight the need for validation of the results presented in this study through scale experiments or field studies. The outcomes of this research establish a

baseline for understanding the general dispersion patterns of wastewater resulting from offshore hydrogen electrolysis. However, certain inaccuracies in the model were identified, such as its inability to represent very small salinity changes when discharge flow rates are high and its potential to smooth gradients in the water's characteristics. Real-world monitoring of future offshore hydrogen production sites will be instrumental in verifying these results. This monitoring will provide crucial data to refine the model inputs and improve the accuracy of predictions.

The results presented in this study establish a valuable foundation for understanding the scope and behaviour of wastewater discharges stemming from offshore hydrogen electrolysis. It is clear that further research is needed to refine these findings and explore potential mitigation strategies. This is crucial, as hydrogen production plays a pivotal role in the transition towards renewable energy sources, especially considering the plans of the Dutch government to launch the first offshore electrolyser in the North Sea by 2031. Doing so aids in advancing our knowledge of sustainable energy production and its environmental implications.

5. Conclusion

This study presents the first hydrodynamical simulation examining the dispersal of wastewater from offshore hydrogen electrolysis. By employing a comprehensive set of numerical simulations, this research provides an effective baseline for future studies and policy development.

A key finding of this study is the identification of ebb-flood processes as a major factor influencing the dispersion of wastewater plumes. During periods of maximum flow rates, such as falling ebb or rising flood, wastewater widely propagates at the surface, while during slack waters, brine effluent sinks. This oscillating pattern underscores the importance of tidal forcings in modulating the environmental impact of wastewater discharge. Discharging brine and coolant simultaneously has no observable effect on the distribution of heat compared to coolant alone, while the salinity distribution is altered significantly: the brine plume is positively buoyant after mixing with coolant, inhibiting sinking processes but increasing surface dispersal.

The distinction between seasonal variations further enhances our understanding, revealing that winter conditions generally result in lower affected volumes compared to summer. This seasonal difference could be attributed to higher wind speeds and more variable wind directions in winter, which facilitate more effective mixing and dissipation of the thermal plumes. A more detailed analysis on these interactions would advance our understanding of the influence of seasonality on the dispersion patterns of wastewater discharge resulting from offshore hydrogen electrolysis.

The study demonstrates that direct effects of brine discharge on marine ecosystems are likely to be minimal due to the relatively small increases in salinity simulated. However, the sinking behaviour of the brine effluent, especially for worst-case scenarios, warrants further consideration. The study highlights the possibility for brine to form density currents and its implications for nutrient cycling and benthic communities. In contrast, the potential direct impact of thermal stress on marine organisms could be substantial, particularly under worst-case scenarios involving a 5 GW electrolyser operating at full capacity. Temperature increases near the discharge point could stress or harm local marine life, including planktonic species and fish, particularly those not adapted to rapid temperature fluctuations. While these effects are likely confined to the immediate vicinity of the discharge point, the study underscores the need for careful management and monitoring to mitigate potential ecological damage. This is especially important as offshore hydrogen electrolysis could impose multiple stressors on marine life, the stacking effects of which are still largely unknown.

Despite the robust modelling approach, the study acknowledges that the assumptions made in the simulations may not fully capture real-world conditions. For instance, the model assumes a constant discharge rate, which does not reflect the variability in power output from offshore wind farms that would drive the electrolyser. The intake of seawater by cooling systems was not accounted for. These factors could significantly alter the dispersion patterns and environmental impacts observed in the simulations. Therefore, further research incorporating more realistic operational scenarios is essential to improve our understanding of the effects of offshore hydrogen production and its implications for the marine environment.

As offshore hydrogen production faces significant growth and technological advancements, it is becoming a key player in the energy transition. The results presented in this study could provide a foundation for developing informed policy, ensuring that the expansion of offshore hydrogen production proceeds in a way that safeguards marine environments.

6. References

Ahmed, F. E., Hashaikeh, R., & Hilal, N. (2020). Hybrid technologies: The future of energy efficient desalination–A review. *Desalination, 495*, 114659.

Ali, N. S., Mo, K., & Kim, M. (2012). A case study on the relationship between conductivity and dissolved solids to evaluate the potential for reuse of reclaimed industrial wastewater. *KSCE Journal of Civil Engineering, 16*, 708-713.

Aljohani, N. S., Kavil, Y. N., Shanas, P. R., Al-Farawati, R. K., Shabbaj, I. I., Aljohani, N. H., & Abdel Salam, M. (2022). Environmental impacts of thermal and brine dispersion using hydrodynamic modelling for Yanbu desalination plant, on the Eastern Coast of the Red Sea. *Sustainability, 14*(8), 4389.

Alkhudhiri, A., Darwish, N., & Hilal, N. (2012). Membrane distillation: A comprehensive review. *Desalination, 287*, 2-18.

Amara, I., Miled, W., Slama, R. B., & Ladhari, N. (2018). Antifouling processes and toxicity effects of antifouling paints on marine environment. A review. *Environmental Toxicology and Pharmacology, 57*, 115-130.

Baars, M. A., Duineveld, G. C. A., Van Duyl, F. C., De Gee, A., Kraay, G. W., Leopold, M. F., & Westra, C. (1991). The ecology of the Frisian Front. *ICES CM, 50*, 25Q.

Bai, J., Zhao, J., Zhang, Z., & Tian, Z. (2022). Assessment and a review of research on surface water quality modeling. *Ecological Modelling, 466*, 109888.

Balmaseda, M. A., Mogensen, K., & Weaver, A. (2013). Evaluation of the ECMWF Ocean Reanalysis ORAS4. *Quarterly Journal of the Royal Meteorological Society, 139*, 1132-1161.

Begun, A. A., & Maslennikov, S. I. (2021). Influence of the Technical Ecosystem of the Electric Power Plant (Vladivostok) on the Phytoplankton of the Japanese Sea. *Water Resources*, *48*(3), 404-412.

Belkin, N., Rahav, E., Elifantz, H., Kress, N., & Berman-Frank, I. (2015). Enhanced salinities, as a proxy of seawater desalination discharges, impact coastal microbial communities of the eastern Mediterranean Sea. *Environmental Microbiology, 17*(10), 4105-4120.

Birol, F., The Future of Hydrogen: Seizing Today's Opportunities. IEA 2019.

Birtwell, I. K., Korstrom, J. S., & Brotherston, A. E. (2003). Laboratory studies on the effects of thermal change on the behaviour and distribution of juvenile chum salmon in sea water. *Journal of Fish Biology, 62*(1), 85-96.

Biton, E., Silverman, J., & Gildor, H. (2008). Observations and modeling of a pulsating density current. *Geophysical Research Letters, 35*(14).

Bosboom, J., & Stive, M. J. (2021). *Coastal dynamics*.

Burchard, H., & Bolding, K. (2002). *GETM – a general estuarine transport model, Scientific documentation, Tech. Rep. EUR 20253 EN*. European Commission, Ispra, Italy.

Cabrerizo, M. J., & Marañón, E. (2021). Temperature fluctuations in a warmer environment: impacts on microbial plankton. *Faculty Reviews, 10*.

Cabrerizo, M. J., Marañón, E., Fernández-González, C., Alonso-Núñez, A., Larsson, H., & Aranguren-Gassis, M. (2021). Temperature fluctuation attenuates the effects of warming in estuarine microbial plankton communities. *Frontiers in Marine Science, 8*, 656282.

Calado, G., & Castro, R. (2021). Hydrogen production from offshore wind parks: Current situation and future perspectives. *Applied Sciences, 11*(12), 5561.

Caparros Mancera, J. J., Segura Manzano, F., Andújar, J. M., Vivas, F. J., & Calderón, A. J. (2020). An optimized balance of plant for a medium-size PEM electrolyzer: design, control and physical implementation. *Electronics, 9*(5), 871.

Capuzzo, J. M. (1980). Impact of power-plant discharges on marine zooplankton: A review of thermal, mechanical and biocidal effects. *Helgoländer Meeresuntersuchungen, 33*, 422-432.

Cassol, G. S., Shang, C., An, A. K., Khanzada, N. K., Ciucci, F., Manzotti, A. & Ling, L. (2024). Ultra-fast green hydrogen production from municipal wastewater by an integrated forward osmosis-alkaline water electrolysis system. *Nature communications*, *15*(1), 2617.

Christiansen, N., Daewel, U., Djath, B., & Schrum, C. (2022). Emergence of large-scale hydrodynamic structures due to atmospheric offshore wind farm wakes. *Frontiers in Marine Science, 9*, 64.

Chuang, Y. L., Yang, H. H., & Lin, H. J. (2009). Effects of a thermal discharge from a nuclear power plant on phytoplankton and periphyton in subtropical coastal waters. *Journal of Sea Research, 61*(4), 197-205.

Cox, R. A., & Smith, N. D. (1959). The specific heat of sea water. *Proceedings of the Royal Society of London. Series A. Mathematical and Physical Sciences, 252*(1268), 51-62.

Crain, C. M., Kroeker, K., & Halpern, B. S. (2008). Interactive and cumulative effects of multiple human stressors in marine systems. *Ecology Letters, 11*(12), 1304-1315.

Creutzberg, F., Wapenaar, P., Duineveld, G., & Lopez, N. L. (1984). Distribution and density of the benthic fauna in the southern North Sea in relation to bottom characteristics and hydrographic conditions. *Rapp PV Reun Cons Int Explor Mer, 183*, 101-110.

Dafforn, K. A., Lewis, J. A., & Johnston, E. L. (2011). Antifouling strategies: history and regulation, ecological impacts and mitigation. *Marine Pollution Bulletin, 62*(3), 453-465.

d'Amore-Domenech, R., & Leo, T. J. (2019). Sustainable Hydrogen Production from Offshore Marine Renewable Farms: Techno-Energetic Insight on Seawater Electrolysis Technologies. *ACS Sustainable Chemistry & Engineering, 7*(9), 8006-8022.

Danish Energy Agency. (2023). *Cost and performance data for offshore hydrogen production report*. DNV. https://ens.dk/sites/ens.dk/files/Energioer/cost_performance_data_offshore_hydrogen_production.pdf

Darre, N. C., & Toor, G. S. (2018). Desalination of water: a review. *Current Pollution Reports, 4*, 104-111.

Davenport, D. M., Deshmukh, A., Werber, J. R., & Elimelech, M. (2018). High-pressure reverse osmosis for energy-efficient hypersaline brine desalination: current status, design considerations, and research needs. *Environmental Science & Technology Letters, 5*(8), 467-475.

Deabes, E. A. (2020). The impact of thermal power stations on coastline and benthic fauna: Case study of El-Burullus power plant in Egypt. *Results in Engineering, 7*, 100128.

Del Bene, J. V., Jirka, G., & Largier, J. (1994). Ocean brine disposal. *Desalination, 97*(1-3), 365-372.

Deltares. (2023). *Delft3D-Flow user manual (version 4.05)- Deltares Systems*. https://oss.deltares.nl/web/delft3d/manuals

Dewicke, A., Rottiers, V., Mees, J., & Vincx, M. (2002). Evidence for an enriched hyperbenthic fauna in the Frisian front (North Sea). *Journal of Sea Research, 47*(2), 121-139.

Dionigi, F., Reier, T., Pawolek, Z., Gliech, M., & Strasser, P. (2016). Design criteria, operating conditions, and nickel–iron hydroxide catalyst materials for selective seawater electrolysis. *ChemSusChem, 9*(9), 962-972.

Dong, Z. G., Chen, Y. H., Ge, H. X., Li, X. Y., Wu, H. L., Wang, C. H., & Che, H. (2018). Response of growth and development of the Pacific oyster (Crassostrea gigas) to thermal discharge from a nuclear power plant. *BMC Ecology, 18*, 1-11.

Drami, D., Yacobi, Y. Z., Stambler, N., & Kress, N. (2011). Seawater quality and microbial communities at a desalination plant marine outfall. A field study at the Israeli Mediterranean coast. *Water Research, 45*(17), 5449-5462.

Dresp, S., Dionigi, F., Klingenhof, M., & Strasser, P. (2019). Direct electrolytic splitting of seawater: opportunities and challenges. *ACS Energy Letters, 4*(4), 933-942.

Dupavillon, J. L., & Gillanders, B. M. (2009). Impacts of seawater desalination on the giant Australian cuttlefish Sepia apama in the upper Spencer Gulf, South Australia. *Marine Environmental Research, 67*(4-5), 207-218.

Egeland-Eriksen, T., Jensen, J. F., Ulleberg, Ø., & Sartori, S. (2023). Simulating offshore hydrogen production via PEM electrolysis using real power production data from a 2.3 MW floating offshore wind turbine. *International Journal of Hydrogen Energy*.

Eichner, S., Kulenkampff, F., & Salman, A. (2022). OffsH2ore island grid for hydrogen production-electrical simulation on how to reach grid stability.

Esbjerg Declaration. (2022). *The Esbjerg Declaration on The North Sea as a Green Power Plant of Europe*. Rijksoverheid. https://open.overheid.nl/documenten/ronl-1e299d084fbc5bfc2968d934ca2f4a97b3931d9f/pdf

Faulkner, A., Bulgin, C. E., & Merchant, C. J. (2021). Characterising industrial thermal plumes in coastal regions using 3-D numerical simulations. *Environmental Research Communications*, *3*(4), 045003.

Feria-Díaz, J. J., López-Méndez, M. C., Rodríguez-Miranda, J. P., Sandoval-Herazo, L. C., & Correa-Mahecha, F. (2021). Commercial thermal technologies for desalination of water from renewable energies: a state of the art review. *Processes, 9*(2), 262.

Fernández-Torquemada, Y., Gónzalez-Correa, J. M., Loya, A., Ferrero, L. M., Díaz-Valdés, M., & Sánchez-Lizaso, J. L. (2009). Dispersion of brine discharge from seawater reverse osmosis desalination plants. *Desalination and Water Treatment, 5*(1-3), 137-145.

Fraunhofer. (2021). *Offshore wind as a cornerstone of the European Green Deal – The potential in upscaling production and utilization*. https://www.fraunhofer.de/content/dam/zv/en/institutes/international/brussels/fraunhofer-green-deal-series/Fraunhofer-Impulse_GreenDeal_Offshore.pdf

Frank, H., Rahav, E., & Bar-Zeev, E. (2017). Short-term effects of SWRO desalination brine on benthic heterotrophic microbial communities. *Desalination, 417*, 52-59.

Gacia, E., Invers, O., Manzanera, M., Ballesteros, E., & Romero, J. (2007). Impact of the brine from a desalination plant on a shallow seagrass (Posidonia oceanica) meadow. *Estuarine, Coastal and Shelf Science, 72*(4), 579-590.

Gaeta, M. G., Samaras, A. G., & Archetti, R. (2020). Numerical investigation of thermal discharge to coastal areas: A case study in South Italy. *Environmental Modelling & Software, 124*, 104596.

Ghaffour, N., Soukane, S., Lee, J. G., Kim, Y., & Alpatova, A. (2019). Membrane distillation hybrids for water production and energy efficiency enhancement: A critical review. *Applied Energy, 254*, 113698.

Görgün, H. (2006). Dynamic modelling of a proton exchange membrane (PEM) electrolyzer. *International Journal of Hydrogen Energy, 31*(1), 29-38.

Gray, J. S. (1997). Marine biodiversity: patterns, threats and conservation needs. *Biodiversity & Conservation, 6*(1), 153-175.

Groenemans, H., Saur, G., Mittelsteadt, C., Lattimer, J., & Xu, H. (2022). Techno-economic analysis of offshore wind PEM water electrolysis for H2 production. *Current Opinion in Chemical Engineering, 37*, 100828.

Guimarães, L. S. F., de Carvalho-Junior, L., Façanha, G. L., da Silva Resende, N., Neves, L. M., & Cardoso, S. J. (2023). Meta-analysis of the thermal pollution caused by coastal nuclear power plants and its effects on marine biodiversity. *Marine Pollution Bulletin, 195*, 115452.

Hahn, S. J., Brandt, A., & Sonnewald, M. (2022). Annotated checklist and biodiversity analysis of benthic fauna at Sylt Outer Reef and Borkum Reef Ground (North Sea). *Check List, 18*(3), 593-628.

Herrero-Gonzalez, M., Admon, N., Dominguez-Ramos, A., Ibañez, R., Wolfson, A., & Irabien, A. (2020). Environmental sustainability assessment of seawater reverse osmosis brine valorization by means of electrodialysis with bipolar membranes. *Environmental Science and Pollution Research, 27*, 1256-1266.

Hilal, N., Kim, G. J., & Somerfield, C. (2011). Boron removal from saline water: A comprehensive review. *Desalination, 273*(1), 23-35.

Hodges, B. R. (2010, March). The importance of mixing and isolation time for desalination brine discharge. In *Proceedings of the International Engineering Conference on Hot Arid Regions (IECHAR 2010), Al-Ahsa, Saudi Arabia* (pp. 1-2).

Hofrichter, A., Rank, D., Heberl, M., & Sterner, M. (2023). Determination of the optimal power ratio between electrolysis and renewable energy to investigate the effects on the hydrogen production costs. *International Journal of Hydrogen Energy, 48*(5), 1651-1663.

Hu, S., Zhang, C., Liu, Q., Li, T., Huang, H., & Liu, S. (2023). Short-term responses of phytoplankton size-fractionated structure and photosynthetic physiology to thermal effluent in a subtropical coastal bay. *Frontiers in Marine Science, 10*, 1102686.

H-TEC. (n.d.). *H-TEC PEM Electrolyser ME450*. https://www.h-tec.com/en/products/detail/h-tec-pem-electrolyser-me450/me450/

International Energy Agency (IEA). (2021). *Net Zero by 2050*. https://www.iea.org/reports/net-zero-by-2050

International Maritime Organization (IMO). (2022). *London Convention and Protocol*. https://www.imo.org/en/OurWork/Environment/Pages/London-Convention-Protocol.aspx

Iso, S., Suizu, S., & Maejima, A. (1994). The lethal effect of hypertonic solutions and avoidance of marine organisms in relation to discharged brine from a destination plant. *Desalination, 97*(1-3), 389-399.

Jia, H. L., Zheng, S., Xie, J., Ying, X. M., & Zhang, C. P. (2016). Influence of geographic setting on thermal discharge from coastal power plants. *Marine Pollution Bulletin, 111*(1-2), 106-114.

Johansen, J. L., Nadler, L. E., Habary, A., Bowden, A. J., & Rummer, J. (2021). Thermal acclimation of tropical coral reef fishes to global heat waves. *eLife, 10*, e59162.

Kong, G., & Guan, W. (2024). Diffusion Characteristics and Mechanisms of Thermal Plumes from Coastal Power Plants: A Numerical Simulation Study. *Journal of Marine Science and Engineering*, *12*(3), 429.

Kremer, C. T., Fey, S. B., Arellano, A. A., & Vasseur, D. A. (2018). Gradual plasticity alters population dynamics in variable environments: thermal acclimation in the green alga Chlamydomonas reinhardtii. *Proceedings of the Royal Society B: Biological Sciences, 285*(20171942).

Kress, N., Gertner, Y., & Shoham-Frider, E. (2020). Seawater quality at the brine discharge site from two mega size seawater reverse osmosis desalination plants in Israel (Eastern Mediterranean). *Water Research, 171*, 115402.

Kültz, D. (2015). Physiological mechanisms used by fish to cope with salinity stress. *The Journal of Experimental Biology, 218*(12), 1907-1914.

Kumar, S., Baalisampang, T., Arzaghi, E., Garaniya, V., Abbassi, R., & Salehi, F. (2023). Synergy of green hydrogen sector with offshore industries: Opportunities and challenges for a safe and sustainable hydrogen economy. *Journal of Cleaner Production, 384*, 135545.

Kumar, S. S., & Himabindu, V. (2019). Hydrogen production by PEM water electrolysis–A review. *Materials Science for Energy Technologies, 2*(3), 442-454.

Kupsco, A., Sikder, R., & Schlenk, D. (2017). Comparative developmental toxicity of desalination brine and sulfate-dominated saltwater in a euryhaline fish. *Archives of Environmental Contamination and Toxicology, 72*, 294-302.

Laguna-Zarate, L., Barrios-Piña, H., Ramírez-León, H., García-Díaz, R., & Becerril-Piña, R. (2021). Analysis of Thermal Plume Dispersion into the Sea by Remote Sensing and Numerical Modeling. *Journal of Marine Science and Engineering, 9*(12), 1437.

Lardicci, C., Rossi, F., & Maltagliati, F. (1999). Detection of thermal pollution: variability of benthic communities at two different spatial scales in an area influenced by a coastal power station. *Marine Pollution Bulletin, 38*(4), 296-303.

Leahy, P., McKeogh, E., Murphy, J., & Cummins, V. (2021). Development of a viability assessment model for hydrogen production from dedicated offshore wind farms. *International Journal of Hydrogen Energy, 46*(48), 24620-24631.

Lee, P. W., Tseng, L. C., & Hwang, J. S. (2018). Comparison of mesozooplankton mortality impacted by the cooling systems of two nuclear power plants at the northern Taiwan coast, southern East China Sea. *Marine Pollution Bulletin, 136*, 114-124.

Lehner, F., & Hart, D. (2022). The importance of water electrolysis for our future energy system. In *Electrochemical Power Sources: Fundamentals, Systems, and Applications* (pp. 1-36). Elsevier.

Le Provost, C., Lyard, F., Genco, M. L., & Rabilloud, F. (1998). A hydrodynamic ocean tide model improved by assimilation of a satellite altimeter-derived data set. *Journal of Geophysical Research, 103*, 5513-5529.

Li, L., Chen, G., Shao, Z., & Huang, H. (2023). Progress on smart integrated systems of seawater purification and electrolysis. *Energy & Environmental Science, 16*(11), 4994-5002.

Li, G., Cheng, L., Zhu, J., Trenberth, K. E., Mann, M. E., & Abraham, J. P. (2020). Increasing ocean stratification over the past half-century. *Nature Climate Change, 10*(12), 1116-1123.

Li, T., Liu, S., Huang, L., Huang, H., Lian, J., Yan, Y., & Lin, S. (2011). Diatom to dinoflagellate shift in the summer phytoplankton community in a bay impacted by nuclear power plant thermal effluent. *Marine Ecology Progress Series, 424*, 75-85.

Li, X. Y., Li, B., & Sun, X. L. (2014). Effects of a coastal power plant thermal discharge on phytoplankton community structure in Zhanjiang Bay, China. *Marine Pollution Bulletin, 81*(1), 210-217.

Liu, W., Li, Q., Gao, F., & Kong, L. (2010). Effect of starvation on biochemical composition and gametogenesis in the Pacific oyster Crassostrea gigas. *Fisheries Science, 76*, 737-745.

Lykkebo Petersen, K., Heck, N., G. Reguero, B., Potts, D., Hovagimian, A., & Paytan, A. (2019). Biological and physical effects of brine discharge from the Carlsbad Desalination plant and implications for future desalination plant constructions. *Water*, *11*(2), 208.

Millero, F. J., Chen, C. T., Bradshaw, A., & Schleicher, K. (1980). A new high-pressure equation of state for seawater. *Deep Sea Research Part A. Oceanographic Research Papers, 27*(3-4), 255-264.

Missimer, T. M., & Maliva, R. G. (2018). Environmental issues in seawater reverse osmosis desalination: Intakes and outfalls. *Desalination, 434*, 198-215.

Mo, S., Du, L., Huang, Z., et al. (2023). Recent Advances on PEM Fuel Cells: From Key Materials to Membrane Electrode Assembly. *Electrochemical Energy Reviews, 6*, 28.

Mogensen, K., Balmaseda, M. A., & Weaver, A. (2012). The NEMOVAR ocean data assimilation system as implemented in the ECMWF ocean analysis for System4. *ECMWF Technical Memorandum 668*. Toulouse, France.

Morales, Y., Samanta, P., Tantish, F., Horn, H., & Saravia, F. (2023). Water management for Power-to-X offshore platforms: an underestimated item. *Scientific Reports, 13*(1), 12286.

Morelissen, R., van der Kaaij, T., & Bleninger, T. (2013). Dynamic coupling of near field and far field models for simulating effluent discharges. *Water science and technology*, *67*(10), 2210-2220.

Morelissen, R., Vlijm, R., Hwang, I., Doneker, R. L., & Ramachandran, A. S. (2016). Hydrodynamic modelling of large-scale cooling water outfalls with a dynamically coupled near-field–far-field modelling system. *Journal of Applied Water Engineering and Research, 4*(2), 138-151.

Niekerk, R., & Manita, R. (2022). Central cooling systems for large-scale green hydrogen production. *Hydrogen Tech World*.

Ni, M., Leung, M. K., & Leung, D. Y. (2008). Energy and exergy analysis of hydrogen production by a proton exchange membrane (PEM) electrolyzer plant. *Energy Conversion and Management, 49*(10), 2748-2756.

Niblett, D., Delpisheh, M., Ramakrishnan, S., & Mamlouk, M. (2024). Review of next generation hydrogen production from offshore wind using water electrolysis. *Journal of Power Sources, 592*, 233904.

Nie, P., Wu, H., Xu, J., Wei, L., Zhu, H., & Ni, L. (2021). Thermal pollution monitoring of Tianwan nuclear power plant for the past 20 years based on Landsat remote sensed data. *IEEE Journal of Selected Topics in Applied Earth Observations and Remote Sensing, 14*, 6146-6155.

Omerspahic, M., Al-Jabri, H., Siddiqui, S. A., & Saadaoui, I. (2022). Characteristics of desalination brine and its impacts on marine chemistry and health, with emphasis on the Persian/Arabian Gulf: a review. *Frontiers in Marine Science, 9*, 845113.

OSPAR Commission. (2021). *Text of the OSPAR Convention*. https://www.ospar.org/convention/text

Panagopoulos, A., Haralambous, K. J., & Loizidou, M. (2019). Desalination brine disposal methods and treatment technologies-A review. *Science of the Total Environment, 693*, 133545.

Pogoda, B., Merk, V., Colsoul, B., Hausen, T., Peter, C., Pesch, R., & Prinz, K. (2020). Site selection for biogenic reef restoration in offshore environments: The Natura 2000 area Borkum Reef Ground as a case study for native oyster restoration. *Aquatic Conservation: Marine and Freshwater Ecosystems, 30*(11), 2163-2179.

PosHYdon. (n.d.). *Proces*. https://poshydon.com/nl/home/proces-2/

Qin, J. J., Lay, W. C. L., & Kekre, K. A. (2012). Recent developments and future challenges of forward osmosis for desalination: A review. *Desalination and Water Treatment, 39*(1-3), 123-136.

Remaili, T. M., Simpson, S. L., Bennett, W. W., King, J. J., Mosley, L. M., Welsh, D. T., & Jolley, D. F. (2018). Assisted natural recovery of hypersaline sediments: salinity thresholds for the establishment of a community of bioturbating organisms. *Environmental Science: Processes & Impacts, 20*(9), 1244-1253.

Riera, R., Tuya, F., Sacramento, A., Ramos, E., Rodríguez, M., & Monterroso, Ó. (2011). The effects of brine disposal on a subtidal meiofauna community. *Estuarine, Coastal and Shelf Science, 93*(4), 359-365.

Rijksoverheid. (2023, March 20). *Windpark boven Groningen beoogd als 's werelds grootste waterstof-op-zee-productie in 2031*. Rijksoverheid.

https://www.rijksoverheid.nl/actueel/nieuws/2023/03/20/windpark-boven-groningen-beoogd-als-s-werelds-grootste-waterstof-op-zee-productie-in-2031#:~:text=In%20het%20windenergiegebied%20Ten%20noorden,moet%20rond%202031%20operationeel%20zijn

Rivera-Ingraham, G. A., & Lignot, J. H. (2017). Osmoregulation, bioenergetics and oxidative stress in coastal marine invertebrates: raising the questions for future research. *Journal of Experimental Biology, 220*(10), 1749-1760.

Rivero-Falcón, Á., Peñate Suárez, B., & Melián-Martel, N. (2023). SWRO Brine Characterisation and Critical Analysis of Its Industrial Valorisation: A Case Study in the Canary Islands (Spain). *Water, 15*(8), 1600.

RWE. (n.d.). *H_2opZee | Hydrogen pilot project from RWE*. https://www.rwe.com/en/research-and-development/hydrogen-projects/h2opzee/

Sajna, M. S., Elmakki, T., Schipper, K., Ihm, S., Yoo, Y., Park, B., & Han, D. S. (2023). Integrated seawater hub: A nexus of sustainable water, energy, and resource generation. *Desalination, 117065*.

Salehmin, M. N. I., Husaini, T., Goh, J., & Sulong, A. B. (2022). High-pressure PEM water electrolyser: A review on challenges and mitigation strategies towards green and low-cost hydrogen production. *Energy Conversion and Management, 268*, 115985.

Sánchez-Lizaso, J. L., Romero, J., Ruiz, J., Gacia, E., Buceta, J. L., Invers, O., & Manzanera, M. (2008). Salinity tolerance of the Mediterranean seagrass Posidonia oceanica: recommendations to minimize the impact of brine discharges from desalination plants. *Desalination, 221*(1-3), 602-607.

Sandström, O., Abrahamsson, I., Andersson, J., & Vetemaa, M. (1997). Temperature effects on spawning and egg development in Eurasian perch. *Journal of Fish Biology, 51*(5), 1015-1024.

Scheepers, F., Stähler, M., Stähler, A., Rauls, E., Müller, M., Carmo, M., & Lehnert, W. (2020). Improving the efficiency of PEM electrolyzers through membrane-specific pressure optimization. *Energies, 13*(3), 612.

Schrum, C., & Backhaus, J. O. (1999). Sensitivity of atmosphere–ocean heat exchange and heat content in the North Sea and the Baltic Sea. *Tellus A*, *51*(4), 526-549.

Shahzad, M. W., Burhan, M., & Ng, K. C. (2017). Pushing desalination recovery to the maximum limit: membrane and thermal processes integration. *Desalination, 416*, 54-64.

Shiomoto, G. T., & Olson, B. H. (1978). Thermal pollution impact upon aquatic life. *Journal of Environmental Health*, 132-139.

Shi, X., Liao, X., & Li, Y. (2020). Quantification of freshwater consumption and scarcity footprints of hydrogen from water electrolysis: A methodology framework. *Renewable Energy, 154*, 786-796.

Simoes, S. G., Catarino, J., Picado, A., Lopes, T. F., Di Berardino, S., Amorim, F., & de Leao, T. P. (2021). Water availability and water usage solutions for electrolysis in hydrogen production. *Journal of Cleaner Production, 315*, 128124.

Sirota, R., Winters, G., Levy, O., Marques, J., Paytan, A., Silverman, J., & Bar-Zeev, E. (2024). Impacts of Desalination Brine Discharge on Benthic Ecosystems. *Environmental Science & Technology, 58*(13), 5631-5645.

Srinath, A. N., Pena López, Á., Miran Fashandi, S. A., Lechat, S., di Legge, G., Nabavi, S. A., & Jafari, S. (2022). Thermal management system architecture for hydrogen-powered propulsion technologies: Practices, thematic clusters, system architectures, future challenges, and opportunities. *Energies, 15*(1), 304.

Stanev, E. V., Dobrynin, M., Pleskachevsky, A., Grayek, S., & Günther, H. (2009). Bed shear stress in the southern North Sea as an important driver for suspended sediment dynamics. *Ocean Dynamics, 59*, 183-194.

Stips, A., Bolding, K., Pohlman, T., & Burchard, H. (2004). Simulating the temporal and spatial dynamics of the North Sea using the new model GETM (general estuarine transport model). *Ocean Dynamics, 54*, 266-283.

Taibi, E., Miranda, R., Vanhoudt, W., Winkel, T., Lanoix, J. C., & Barth, F. (2018). *Hydrogen from renewable power: Technology outlook for the energy transition*.

Troost, K., van Asch, M., Craeymeersch, J. A. M., Duineveld, G., Escaravage, V., Goudswaard, P. C., & Wijnhoven, S. (2013). *Monitoringsplan T0 VHR gebieden Noordzee (No. C049/13)*. IMARES.

van der Molen, J., Ruardij, P., & Greenwood, N. (2016). Potential environmental impact of tidal energy extraction in the Pentland Firth at large spatial scales: results of a biogeochemical model. *Biogeosciences*, *13*(8), 2593-2609.

van der Roest, E., Bol, R., Fens, T., & van Wijk, A. (2023). Utilisation of waste heat from PEM electrolysers–Unlocking local optimisation. *International Journal of Hydrogen Energy*.

van Leeuwen, S., Tett, P., Mills, D., & van der Molen, J. (2015). Stratified and nonstratified areas in the North Sea: Long-term variability and biological and policy implications. *Journal of Geophysical Research: Oceans, 120*(7), 4670-4686.

Voorhees, J. P., Phillips, B. M., Anderson, B. S., Siegler, K., Katz, S., Jennings, L., & de la Paz Carpio-Obeso, M. (2013). Hypersalinity toxicity thresholds for nine California ocean plan toxicity test protocols. *Archives of Environmental Contamination and Toxicology, 65*, 665-670.

Wang, T., Cao, X., & Jiao, L. (2022). PEM water electrolysis for hydrogen production: fundamentals, advances, and prospects. *Carbon Neutrality, 1*(1), 21.

Wood, J. E., Silverman, J., Galanti, B., & Biton, E. (2020). Modelling the distributions of desalination brines from multiple sources along the Mediterranean coast of Israel. *Water Research, 173*, 115555.

Yue, M., Lambert, H., Pahon, E., Roche, R., Jemei, S., & Hissel, D. (2021). Hydrogen energy systems: A critical review of technologies, applications, trends and challenges. *Renewable and Sustainable Energy Reviews, 146*, 111180.

Zainal, B. S., Ker, P. J., Mohamed, H., Ong, H. C., Fattah, I. M. R., Rahman, S. A., & Mahlia, T. I. (2024). Recent advancement and assessment of green hydrogen production technologies. *Renewable and Sustainable Energy Reviews, 189*, 113941.

Zauner, A., Böhm, H., Rosenfeld, D. C., & Tichler, R. (2019). Innovative large-scale energy storage technologies and Power-to-Gas concepts after optimization. Analysis on future technology options and on techno-economic optimization.

Zhang, J., Wang, Y., Ottmann, D., Cao, P., Yang, J., Yu, J., & Lv, Z. (2023). Seasonal variability of phytoplankton community response to thermal discharge from nuclear power plant in temperate coastal area. *Environmental Pollution, 318*, 120898.

7. Appendix

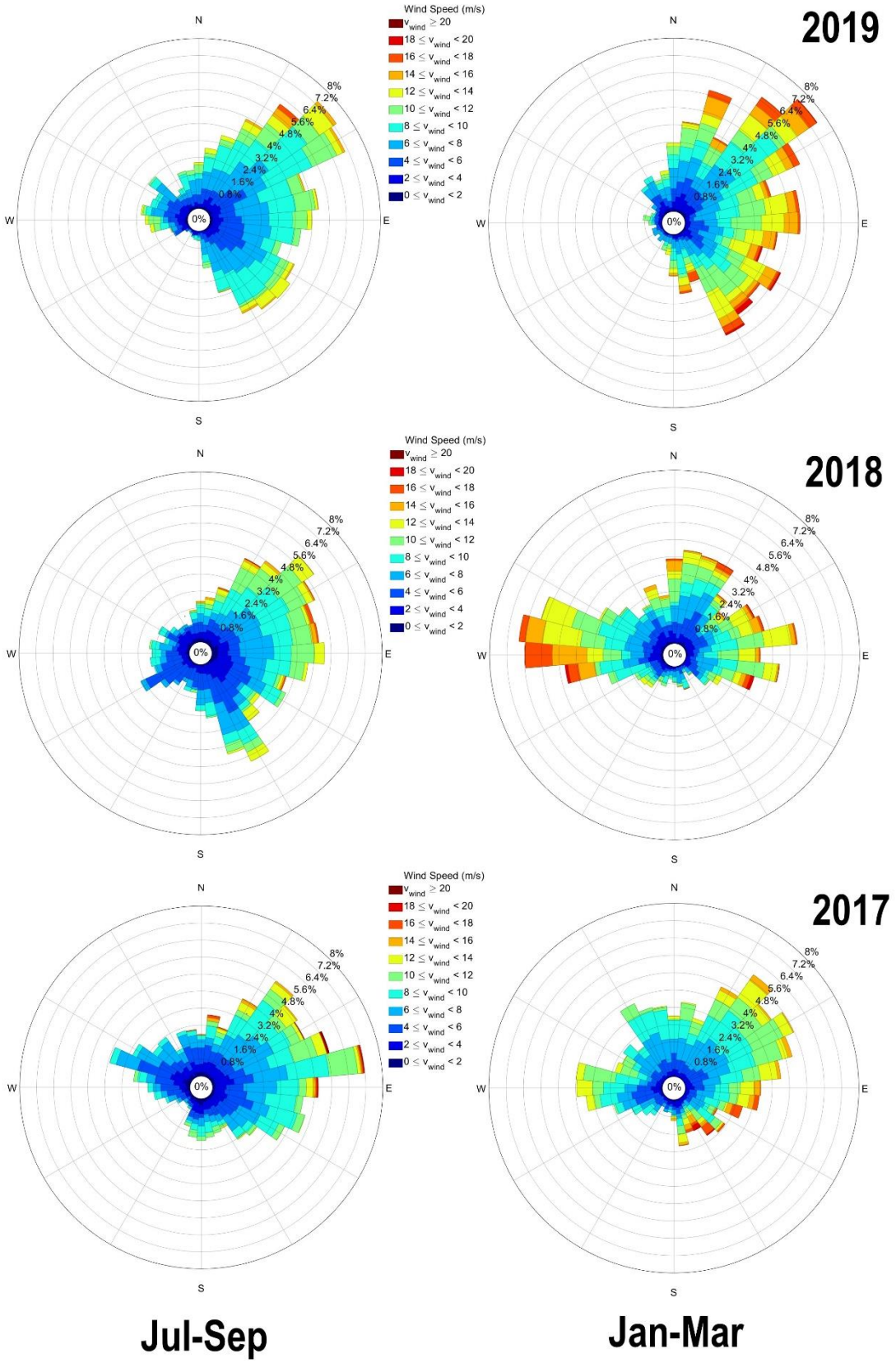

Appendix A. *Average wind speed at 10 meter elevation over the simulated domain for summer (July, August and September) and winter (January, February and March) for years 2019. 2018 and 2017.*

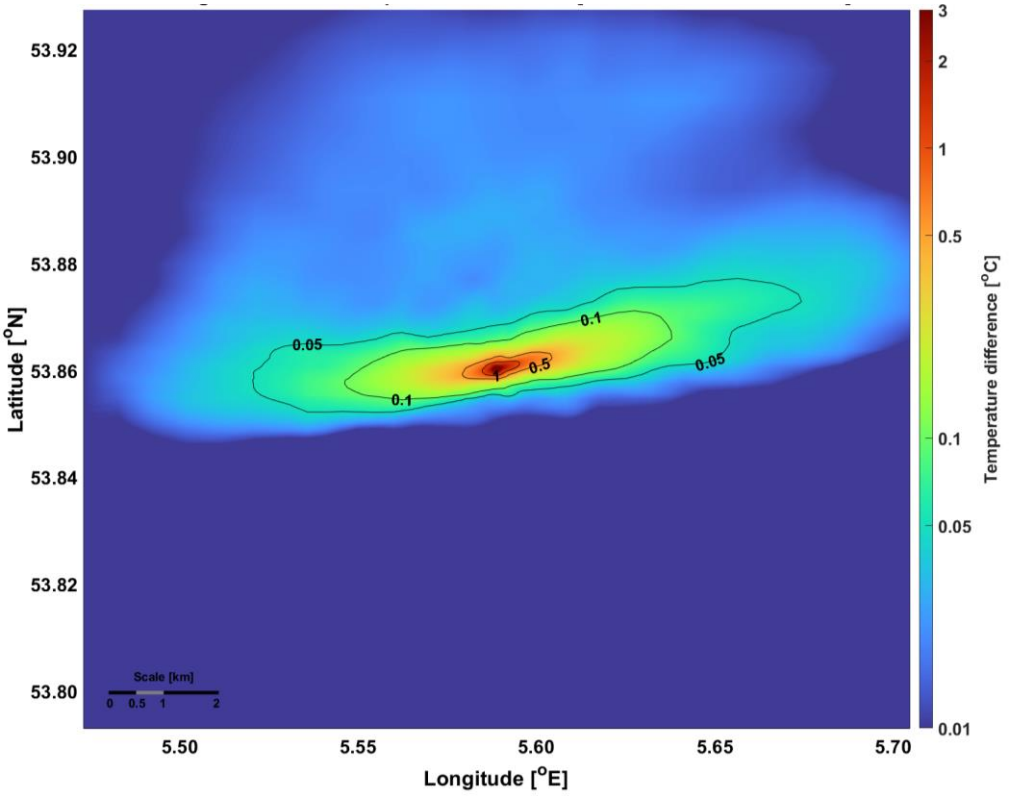

Appendix B. *Average sea surface temperature difference for a 5 GW electrolyser discharging both brine and coolant during summer.*

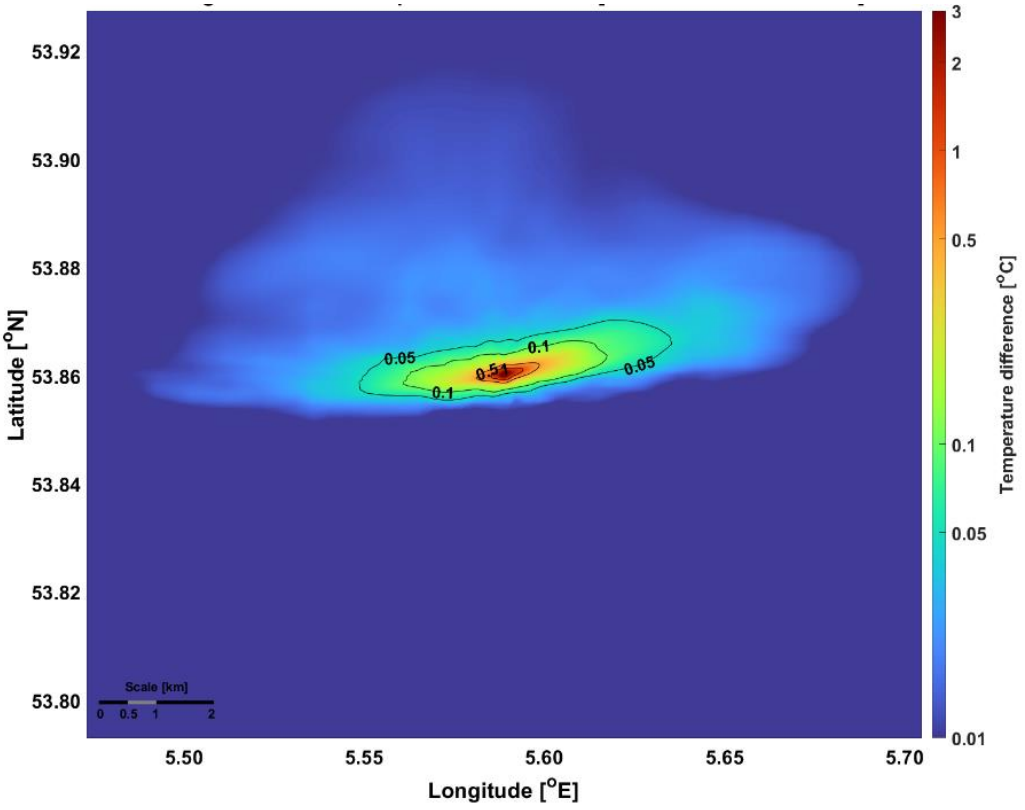

Appendix C. *Average sea surface temperature difference for a 5 GW electrolyser discharging both brine and coolant during winter.*

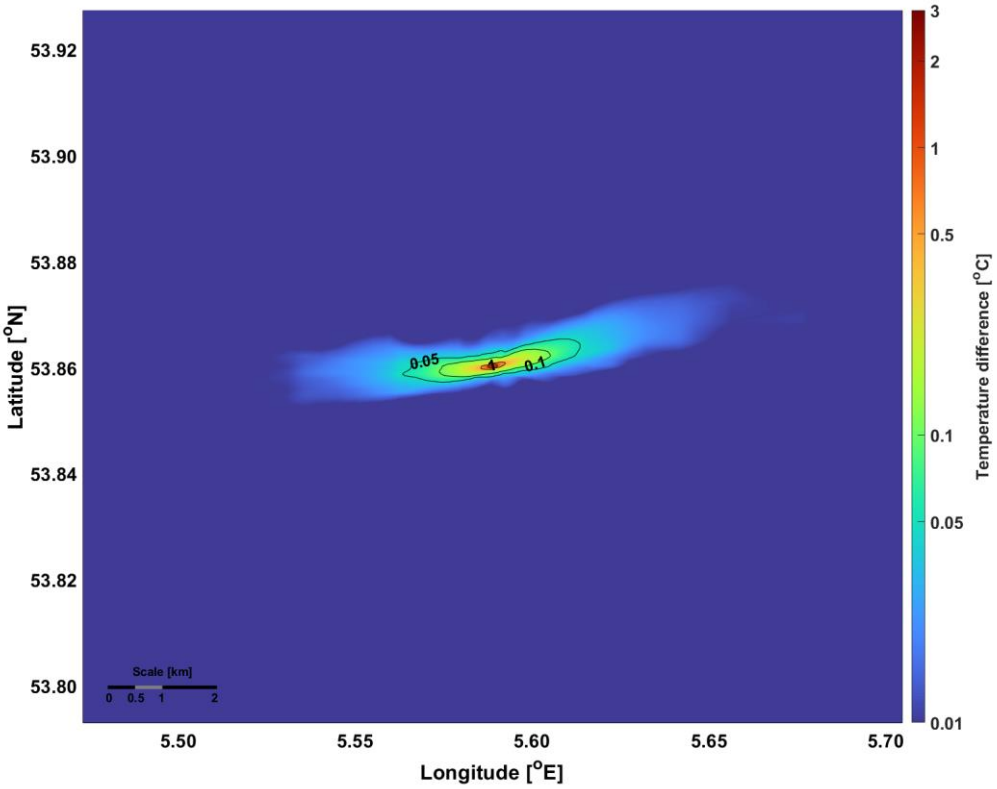

Appendix D. *Average sea surface temperature difference for a 1 GW electrolyser discharging coolant during summer.*

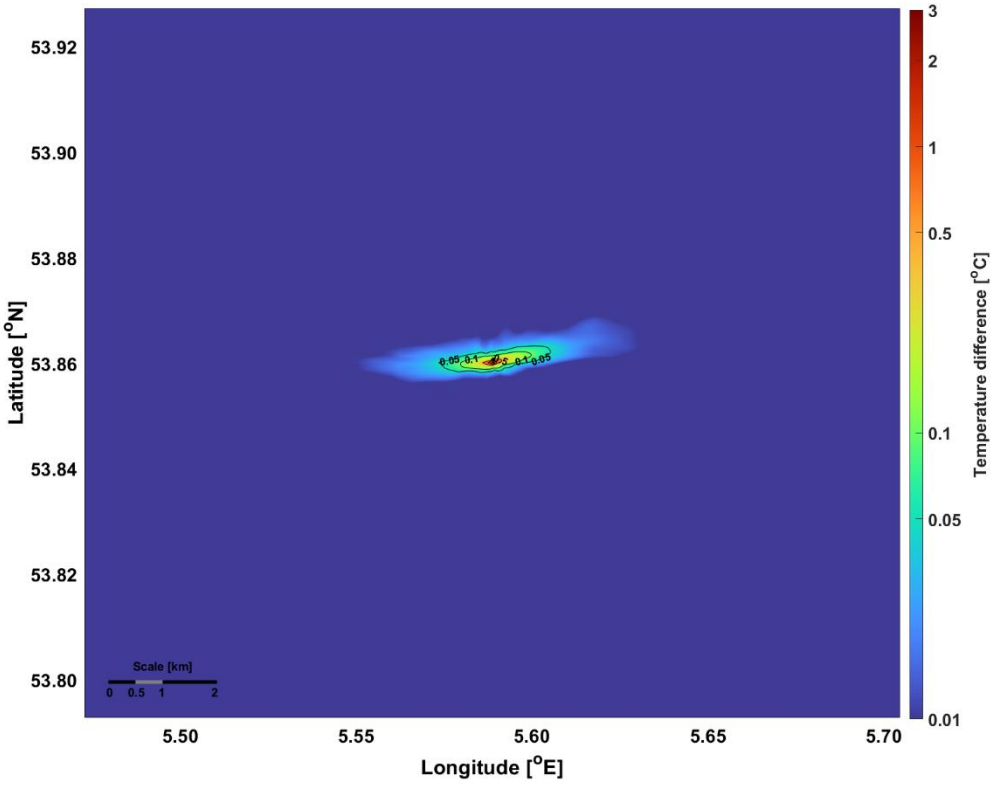

Appendix E. *Average sea surface temperature difference for a 1 GW electrolyser discharging coolant during winter.*

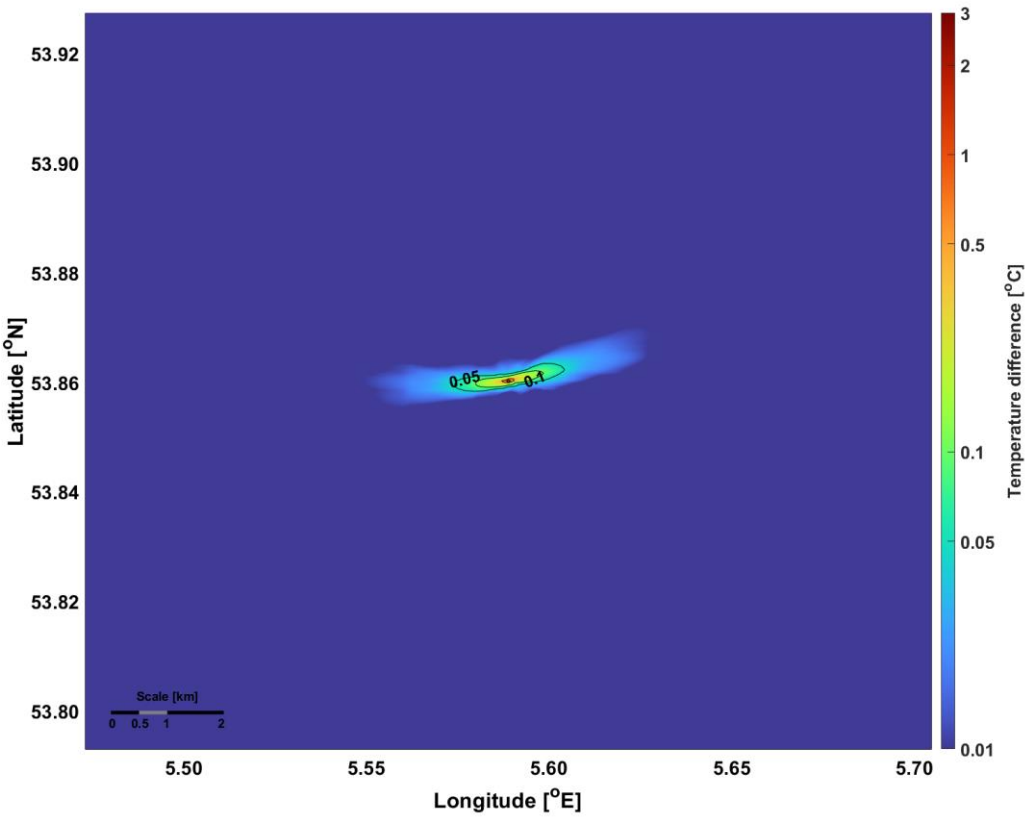

Appendix F. *Average sea surface temperature difference for a 0.5 GW electrolyser discharging coolant during summer.*

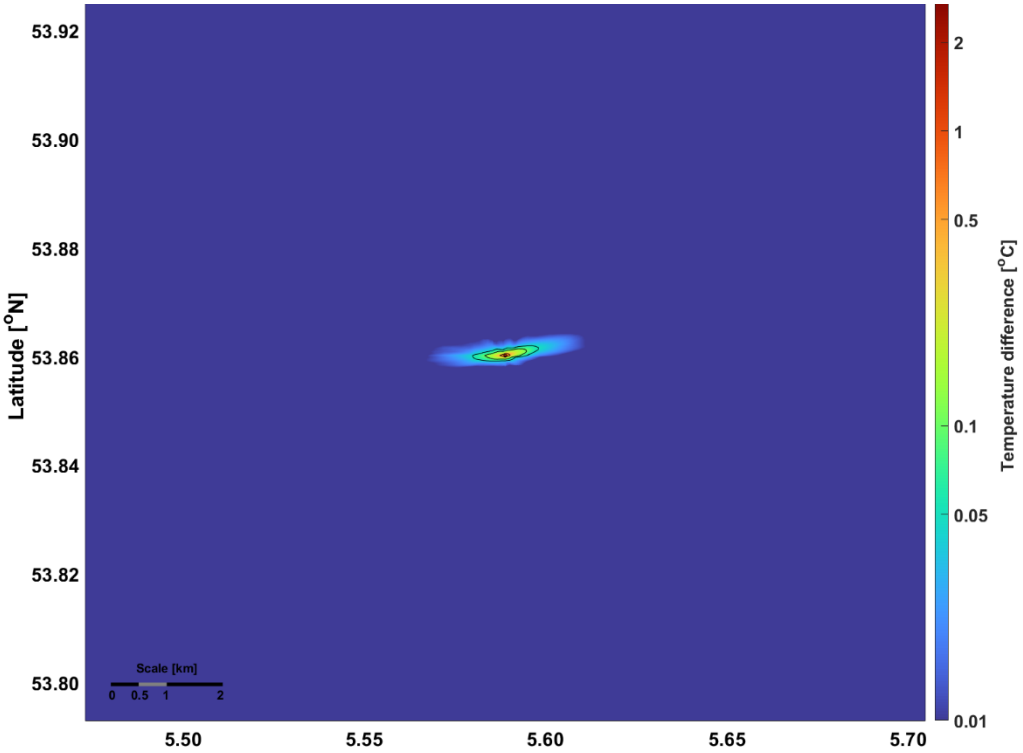

Appendix G. *Average sea surface temperature difference for a 0.5 GW electrolyser discharging coolant during winter.*

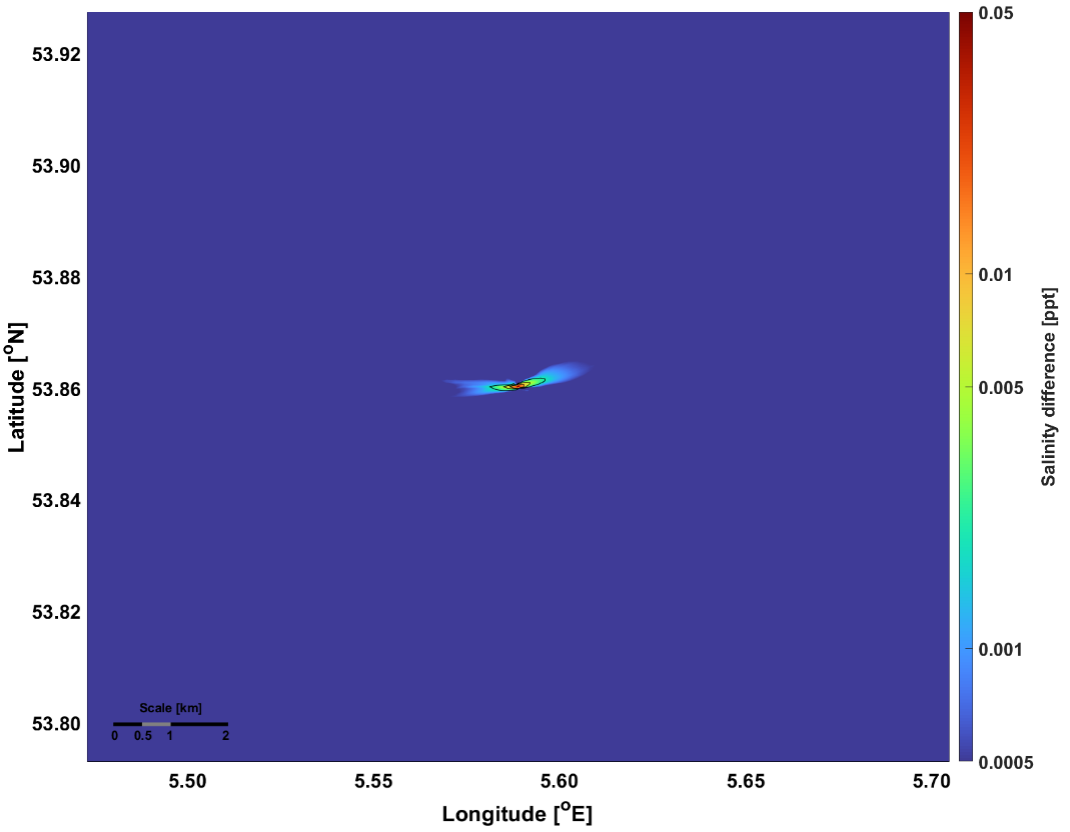

Appendix H. *Average sea surface salinity difference for a 1 GW electrolyser discharging brine during summer.*

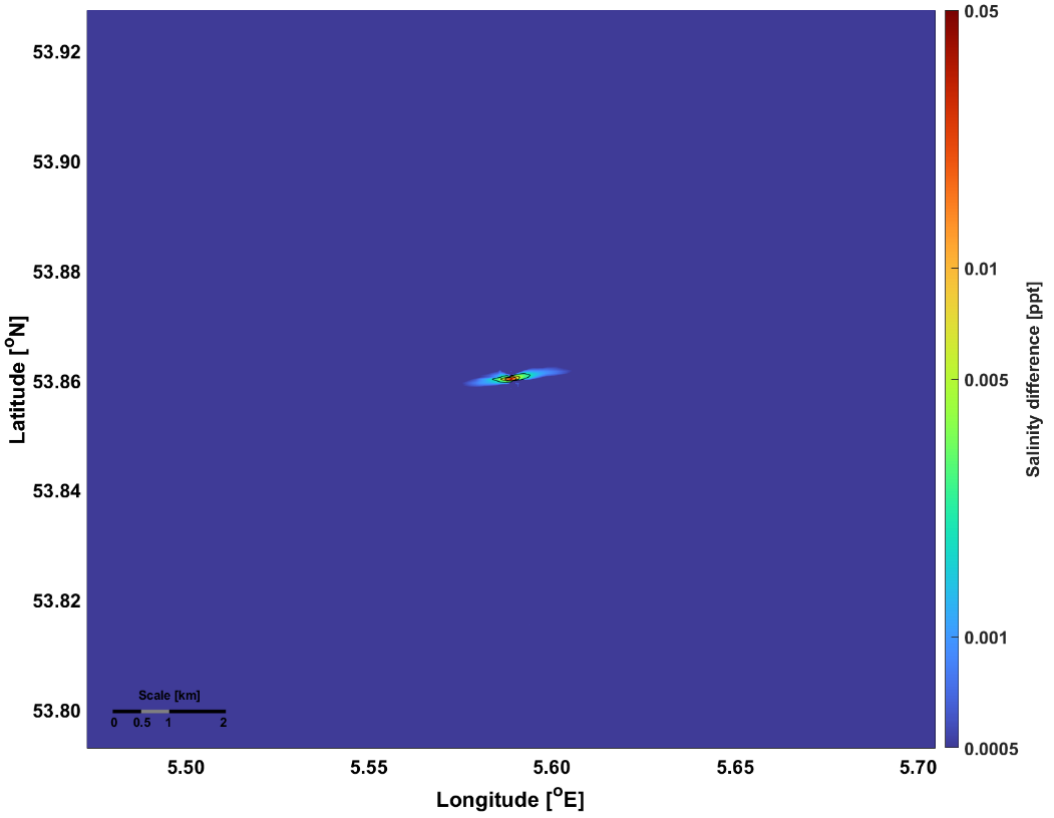

Appendix I. *Average sea surface salinity difference for a 1 GW electrolyser discharging brine during summer.*

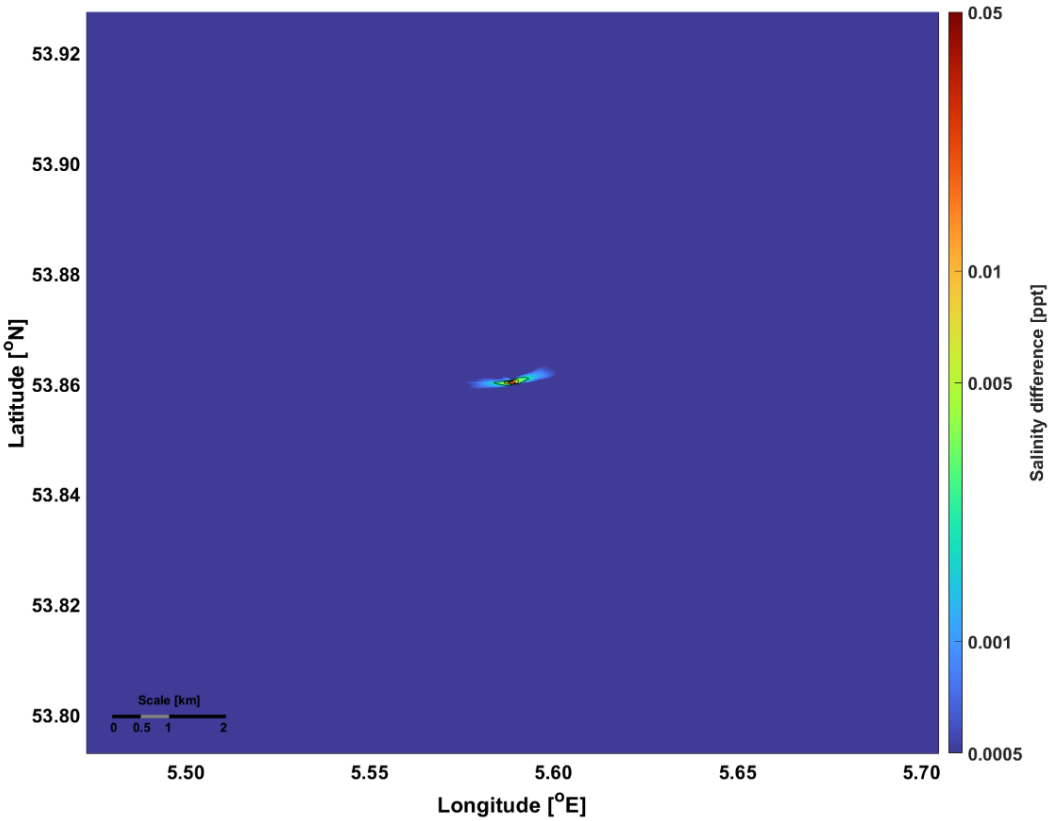

Appendix J. *Average sea surface salinity difference for a 0.5 GW electrolyser discharging brine during summer.*

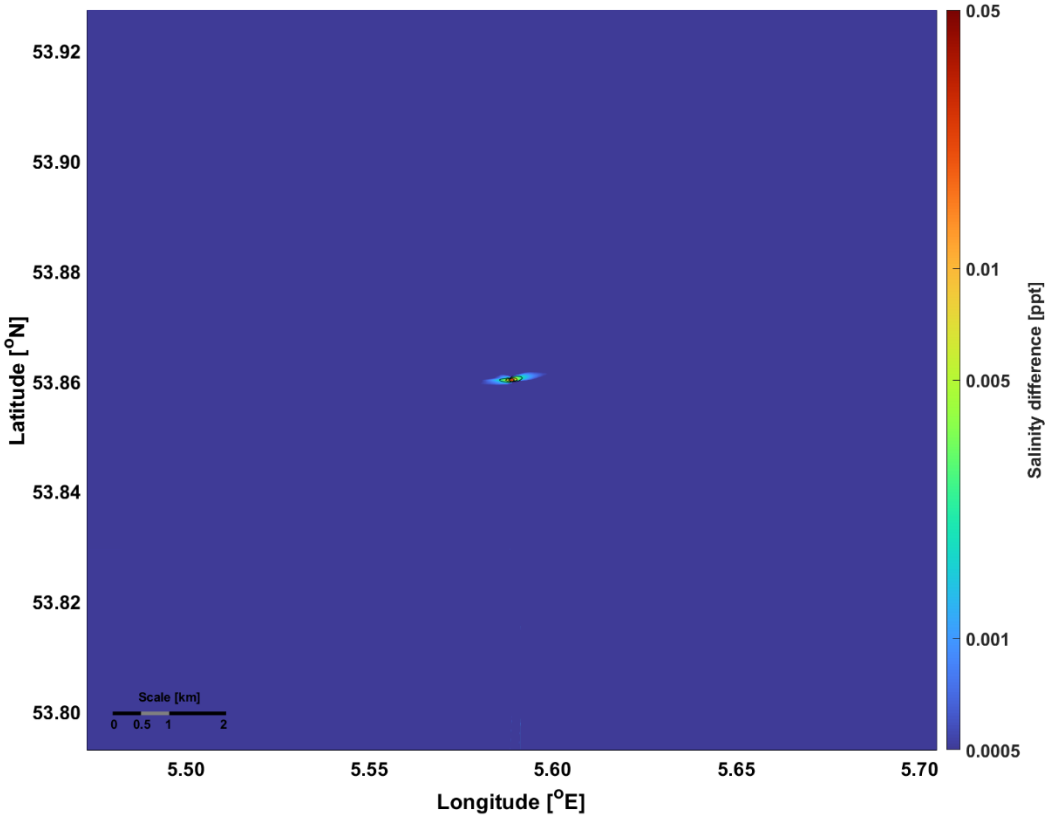

Appendix K. *Average sea surface salinity difference for a 0.5 GW electrolyser discharging brine during winter.*

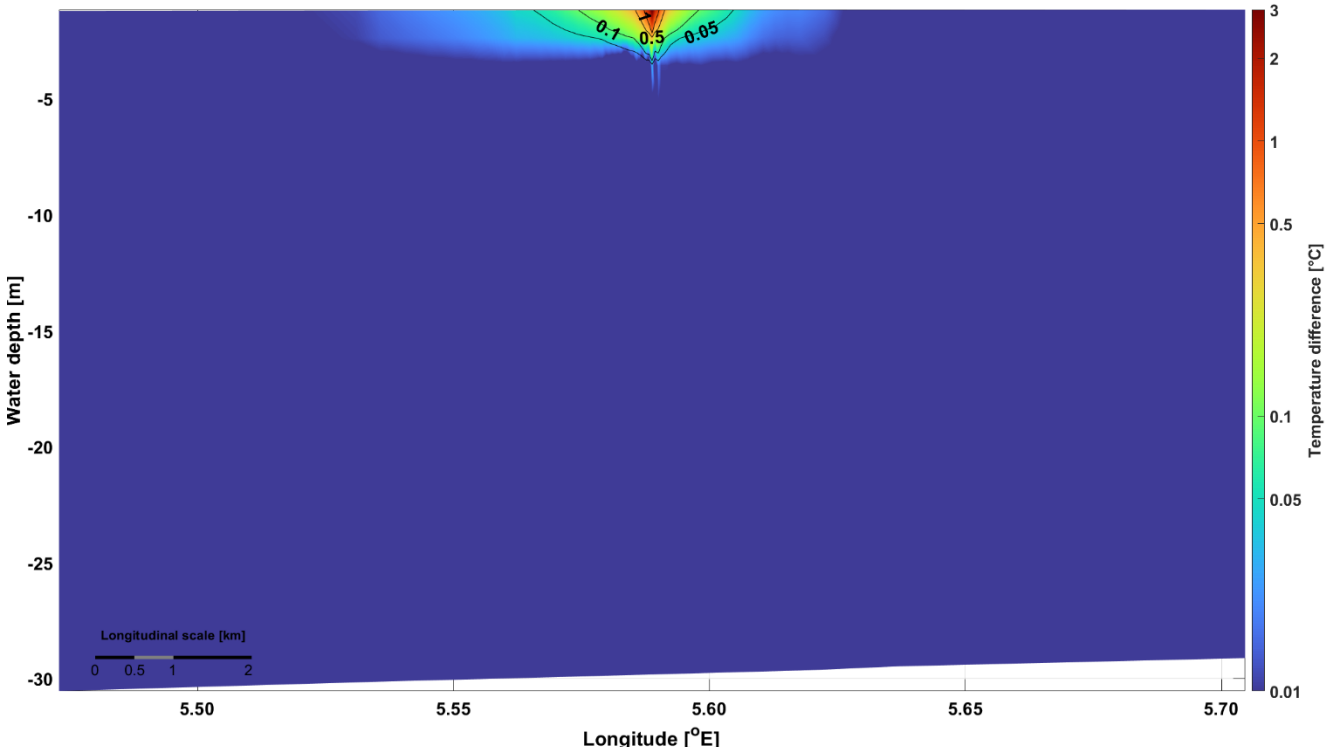

Appendix L. *Average cross-sectional temperature difference for a 1 GW electrolyser discharging coolant during summer.*

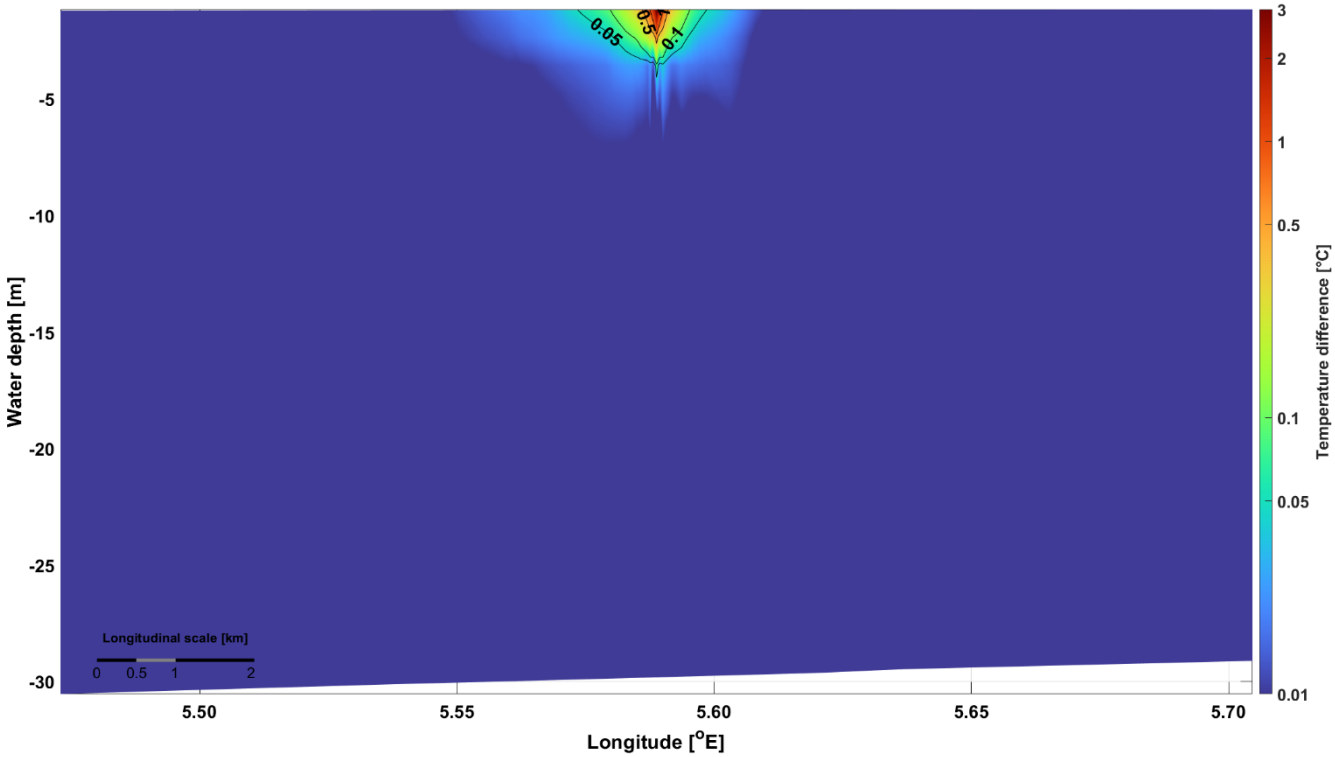

Appendix M. *Average cross-sectional temperature difference for a 1 GW electrolyser discharging coolant during winter.*

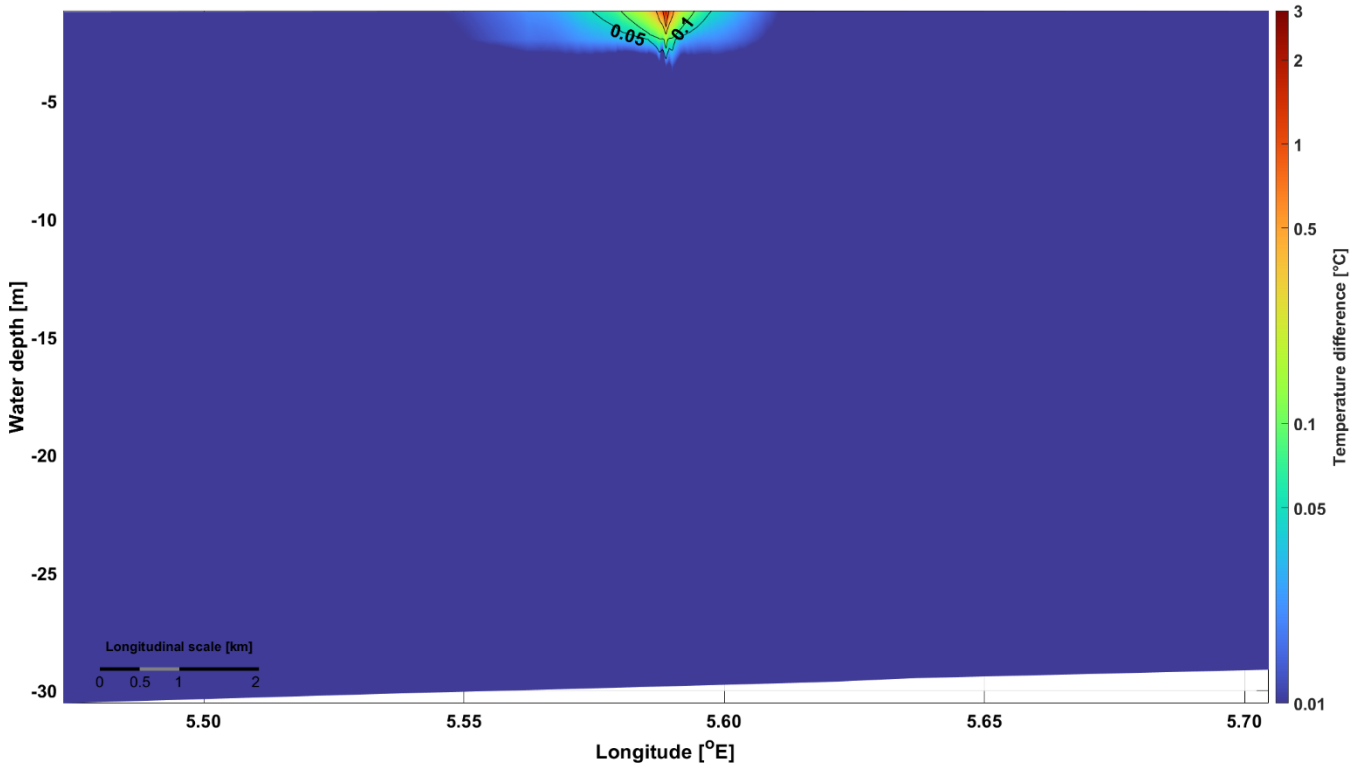

Appendix N. *Average cross-sectional temperature difference for a 0.5 GW electrolyser discharging coolant during summer.*

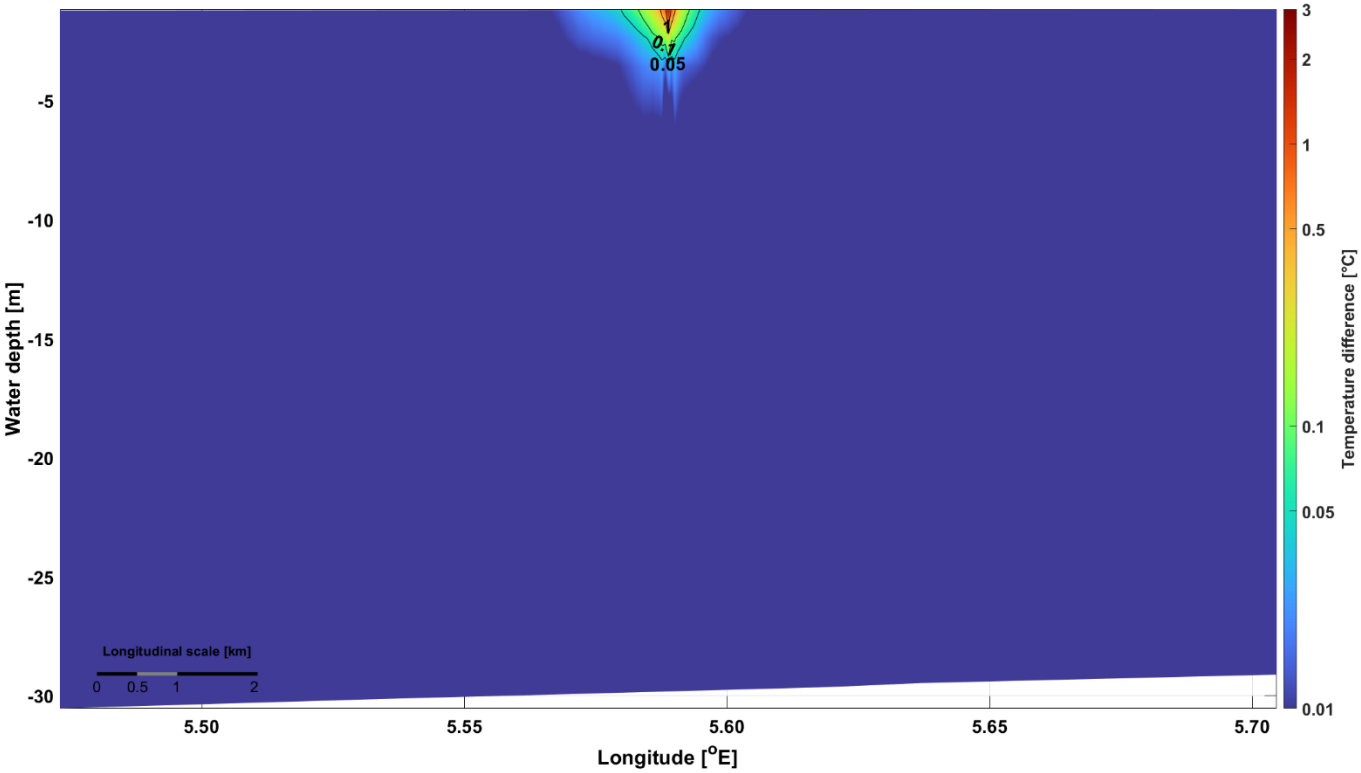

Appendix O. *Average cross-sectional temperature difference for a 0.5 GW electrolyser discharging coolant during winter.*

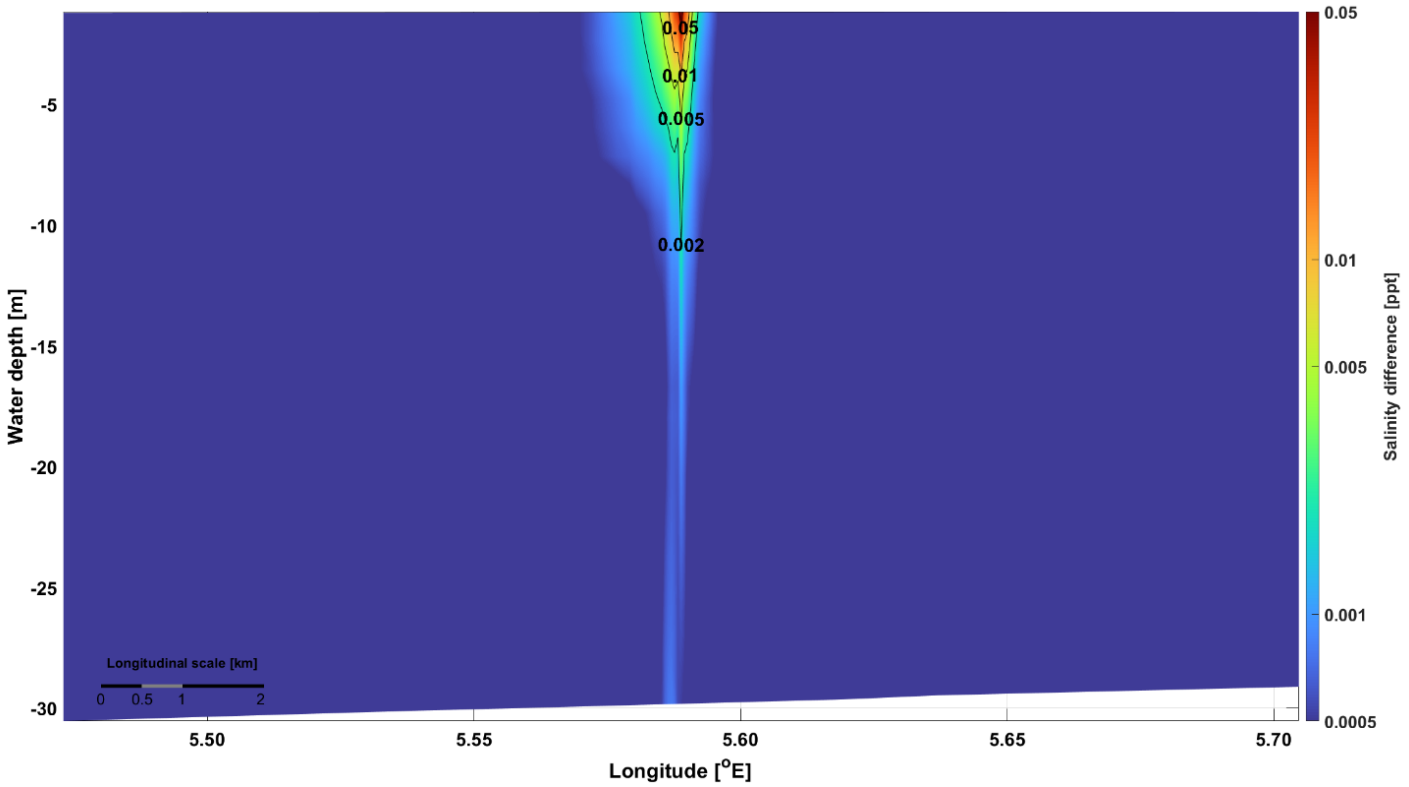

Appendix P. *Average cross-sectional salinity difference for a 1 GW electrolyser discharging brine during summer.*

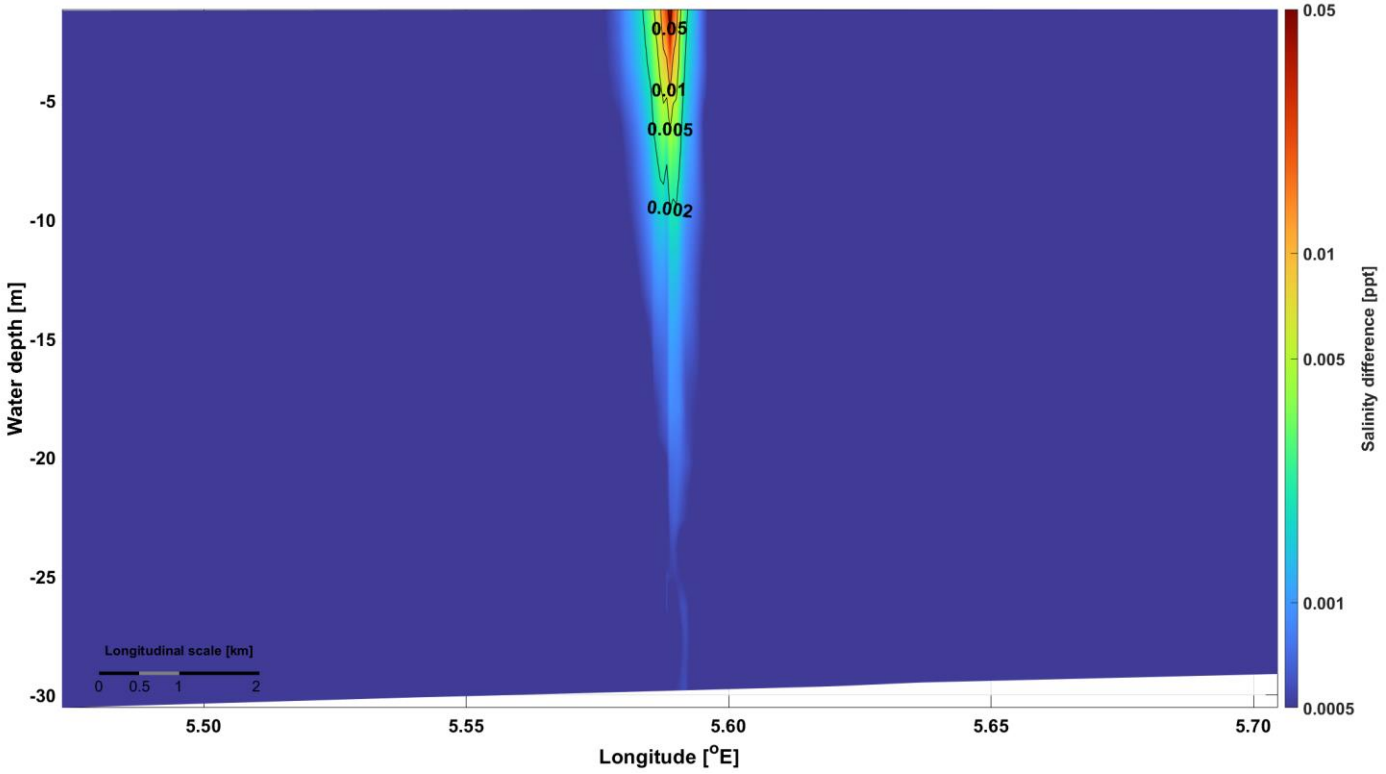

Appendix Q. *Average cross-sectional salinity difference for a 1 GW electrolyser discharging brine during winter.*

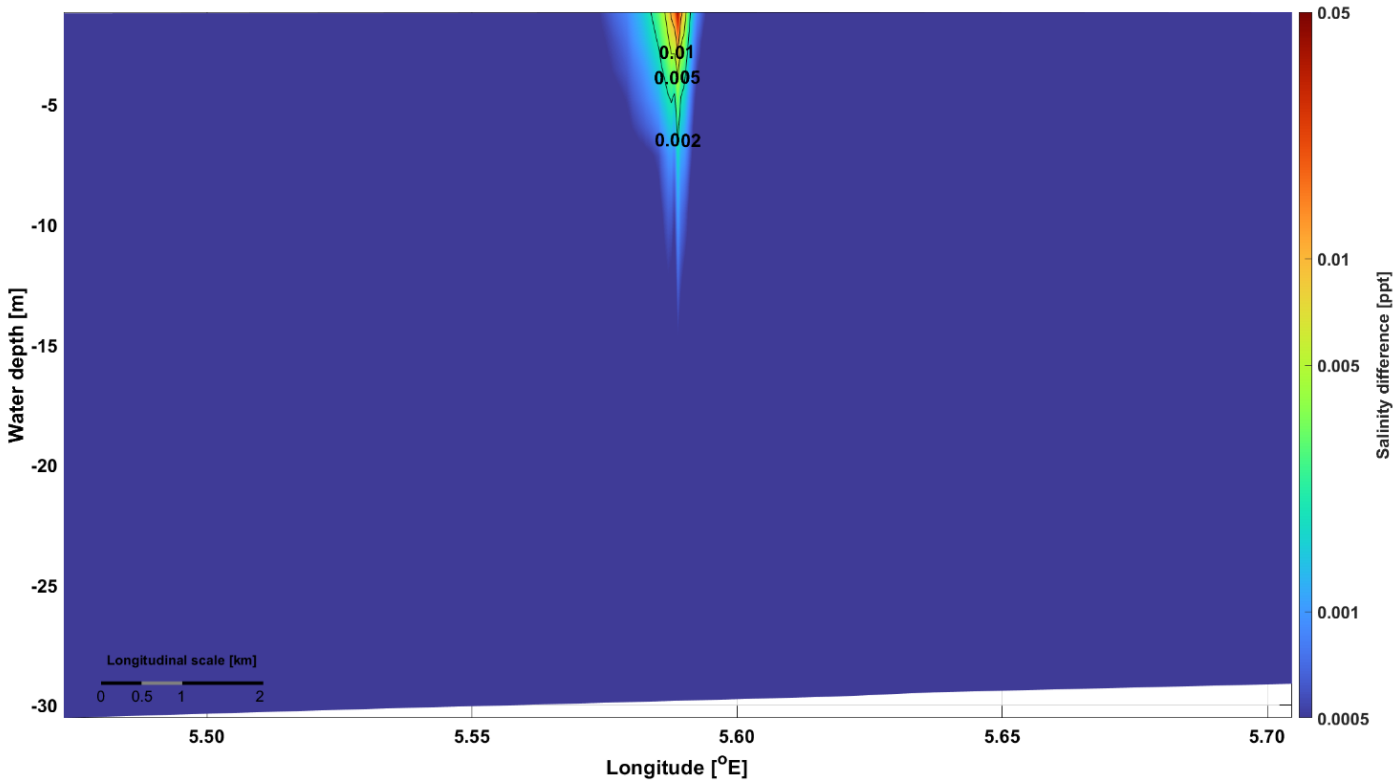

Appendix R. *Average cross-sectional salinity difference for a 0.5 GW electrolyser discharging brine during summer.*

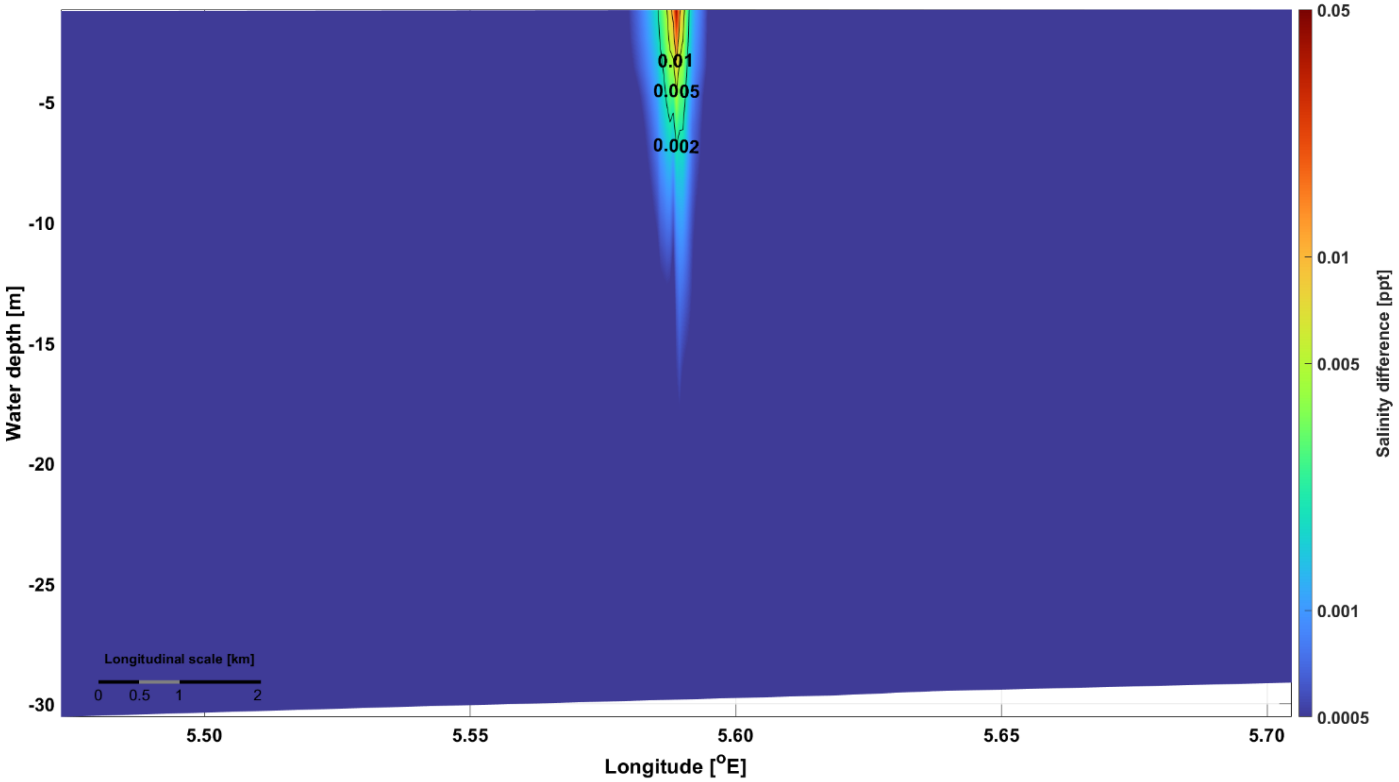

Appendix S. *Average cross-sectional salinity difference for a 0.5 GW electrolyser discharging brine during winter.*

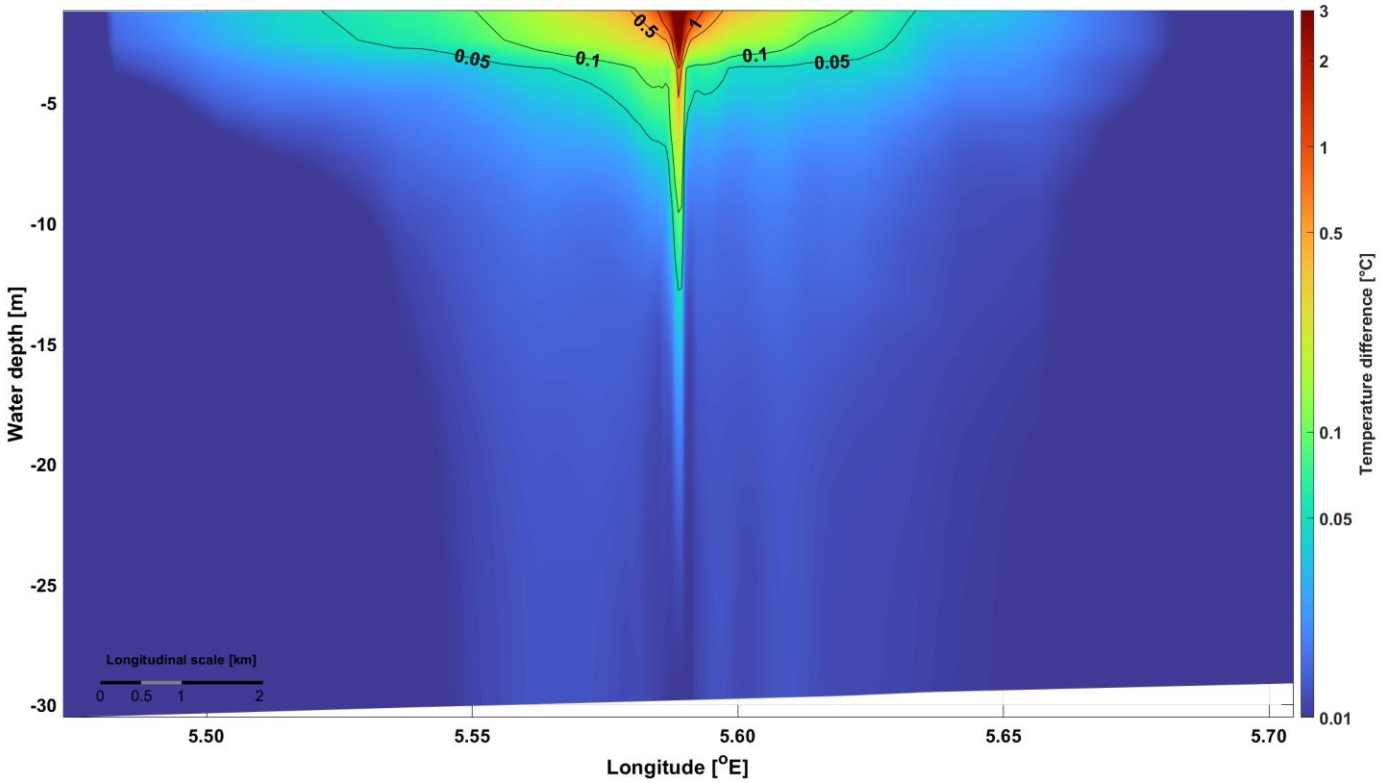

Appendix T. *Average cross-sectional temperature difference for a 5 GW electrolyser discharging coolant and brine simultaneously during summer.*

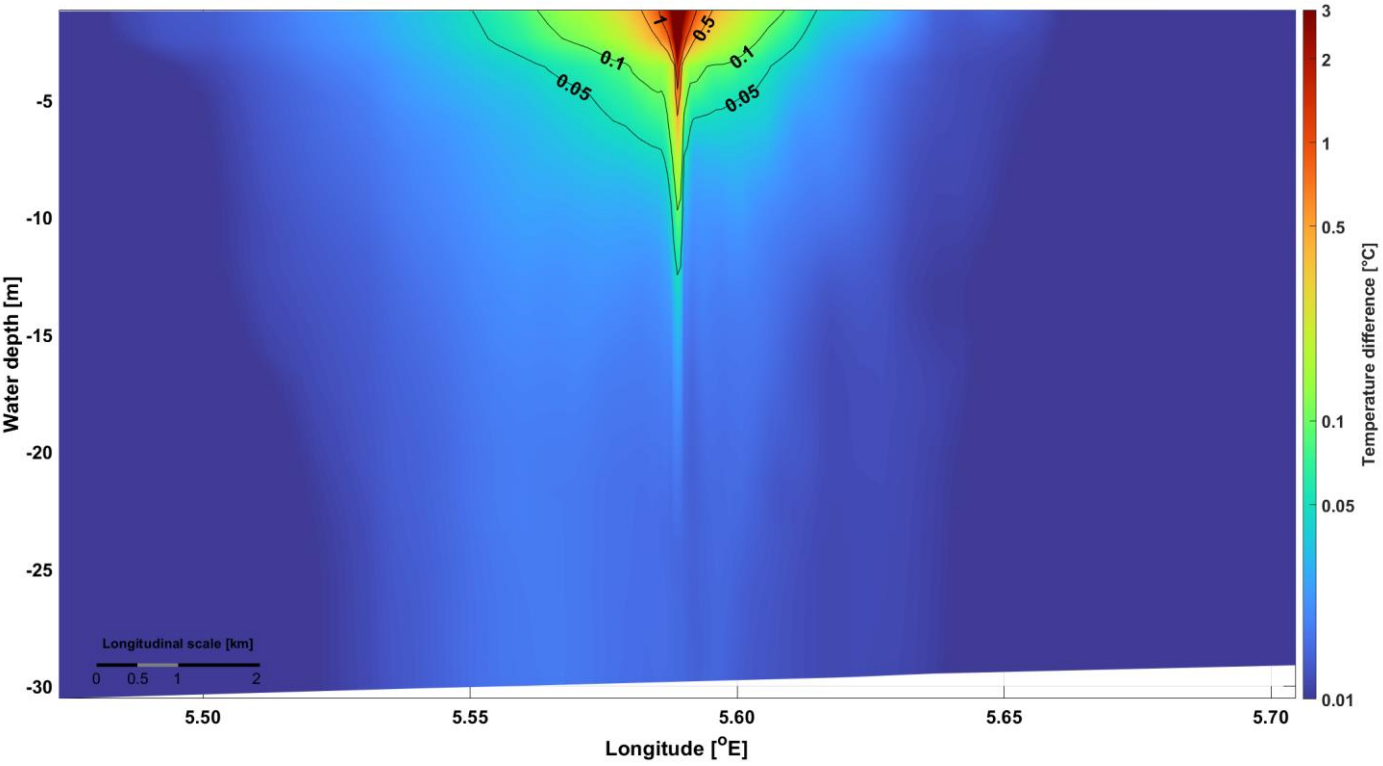

Appendix U. *Average cross-sectional temperature difference for a 5 GW electrolyser discharging coolant and brine simultaneously during winter.*